MONOLITHIC AND HYBRID SILICON-ON-INSULATOR INTEGRATED OPTICAL DEVICES

A DISSERTATION SUBMITTED TO
THE DEPARTMENT OF PHYSICS
AND THE INSTITUTE OF ENGINEERING AND SCIENCE
OF BILKENT UNIVERSITY
IN PARTIAL FULFILLMENT OF THE REQUIREMENTS
FOR THE DEGREE OF
DOCTOR OF PHILOSOPHY

By
İsa Kiyat
August, 2005

I certify that I have read this thesis and that in my opinion it is fully adequate, in scope and in quality, as a dissertation for the degree of doctor of philosophy.

Prof. Dr. Atilla Aydınlı(Supervisor)

I certify that I have read this thesis and that in my opinion it is fully adequate, in scope and in quality, as a dissertation for the degree of doctor of philosophy.

Prof. Dr. Cengiz Beşikçi

I certify that I have read this thesis and that in my opinion it is fully adequate, in scope and in quality, as a dissertation for the degree of doctor of philosophy.

Assoc. Prof. Dr. Recai Ellialtıoğlu

I certify that I have read this thesis and that in my opinion it is fully adequate, in scope and in quality, as a dissertation for the degree of doctor of philosophy.

Assoc. Prof. Dr. Oğuz Gülseren

I certify that I have read this thesis and that in my opinion it is fully adequate, in scope and in quality, as a dissertation for the degree of doctor of philosophy.

Asst. Prof. Dr. Vakur B. Ertürk

Approved for the Institute of Engineering and Science:

Prof. Dr. Mehmet B. Baray
Director of the Institute

ABSTRACT

MONOLITHIC AND HYBRID SILICON-ON-INSULATOR INTEGRATED OPTICAL DEVICES

İsa Kiyat
PhD in Physics
Supervisor: Prof. Dr. Atilla Aydınlı
August, 2005

Silicon, the basic material of electronics industry is rediscovered nowadays for its potential use in photonics and integrated optics. The research activity in silicon integrated optics have been speeding up during the last decade and even attracting interest of leading industrial companies. As a contribution to this world wide effort, we have designed, fabricated and characterized a class of monolithic and hybrid silicon integrated optical devices. These devices were realized on high-quality silicon-on-insulator (SOI) wafers. Beam propagation method (BPM) based simulations and analytical calculations were employed for the design.

We have demonstrated for the first time an SOI device that splits light into its TE and TM components. An SOI rib waveguide becomes birefringent as its size reduced. This idea is used to design and fabricate a directional coupler polarization splitter based on geometrical birefringence. The device uses 1 μm sized SOI waveguides. This compact device (only 110 μm in length) shows extinction ratios larger than 20 dB.

SOI waveguides with the same geometry was used to realize a batch of single and double bus racetrack resonators having radii in the range of 20 to 500 μm. Design of these racetrack resonators are presented in detail. The bending loss and coupling factor calculations were performed using BPM. During the design and analysis of waveguide resonators, we proposed a novel displacement sensor that can be used for scanning probe microscopies. The sensor operates by means of monitoring the changes in transmission spectrum of a high finesse micro-ring resonator due to stress induced by displacement. Operation principles and sensitivity calculations are discussed in detail.

SOI resonators with quality factors (Q) as high as 119000 have been achieved.

This is the highest Q value for resonators based on SOI rib waveguides to date. Finesse values as large as 43 and modulation depths of 15 dB were observed. Free spectral ranges increased from 0.2 nm to 3.0 nm when radius was decreased from 500 to 20 μm. The thermo-optical tunability of these resonators were also studied. A high-Q racetrack resonator is used to develop a wavelength selective optical switch. The resonator was thermo-optically scanned over its full free spectral range applying only 57 mW of electrical power. A low power of 17 mW was enough to tune from resonance to off-resonance state. The device functioned as a wavelength selective optical switch with a 3 dB cutoff frequency of 210 kHz. We have also demonstrated wavelength add/drop filters using the same racetrack resonators with double bus. Asymmetric lateral coupling was used in order to get better filter characteristics. Filters with crosstalks as low as -10.0 dB and Q-factors of as high as 51000 were achieved.

Finally, we introduce the use of a layer transfer method for SOI wafers. Such a layer transfer results in the possibility of using the back side of the silicon layer in SOI structure for further processing. With this method, previously fabricated SOI waveguides were transferred to form hybrid silicon-polymer waveguides. Benzocyclobutene (BCB) polymer was used as the bonding agent. The method is also applied to SOI M-Z interferometers to explore the possibilities of the technology. We additionally studied asymmetric vertical couplers (AVC) based on polymer and silicon waveguides and fabricated them using a hybrid technology.

Keywords: Integrated optics, Silicon-on-insulator technology, Optical waveguides, Polarization splitters, Ring resonators, Racetrack resonators, Displacement sensors, Wavelength add-drop filters, Thermo-optical effect, Wavelength selective optical switch, Hybrid integration, Wafer bonding, Mach-Zehnder modulator, Asymmetric vertical coupler.

ÖZET

YEKPARE VE MELEZ YALITKAN ÜSTÜ SİLİSYUM TÜMLEŞIK OPTİK AYGITLAR

İsa Kiyat
Fizik, Doktora
Tez Yöneticisi: Prof. Dr. Atilla Aydınlı
Ağustus, 2005

Elektronik endüstrisinin temel malzemesi olan silisyum son zamanlarda olası fotonik ve tümleşik optik uygulamaları için tekrar keşfedilmektedir. Silisyum tümleşik optik konusundaki araştırma faliyetleri son on yılda hızlanmakta ve hatta lider endüstri şirketlerinin de ilgisini çekmektedir. Dünya çapindakı bu çabaya katkı olarak, biz de bazı yekpare ve melez silisyum tümleşik optik aygıtları tasarlayıp, üretip ve karakterize ettik. Bu cihazlar yüksek kalitede yalıtkan üstü silisyum (YÜS) yongalar üstünde gerçekleştirildi. Tasarım için ışın ilerletme metoduna (IİM) dayalı nümerik benzeştirmeler ve analitik hesaplamalar kullanıldı.

İlk kez ışığı TE ve TM bileşenlerine ayıran bir YÜS cihazının çalıştığını gösterdik. Boyutları küçüldükçe bir YÜS sırt dalga kılavuzunun polarizasyon bağımlılıgı artmaktadır. Bu fikir kullanılarak bir doğrusal çiftleyici polarizasyon ayırıcı tasarlanıp üretildi. Cihazda 1 μm boyutlarında YÜS dalgakılavuzu kullanılmaktadir. Bu küçuk cihazla (sadece 110 μm boyunda) 20 dB den büyük ayırma oranları elde edilebilmektedir.

Aynı geometrik yapıya sahip YÜS dalgakılavuzları bir grup tek ve çift dalgakılavuzlu 20-500 μm yarıçapli koşuyolu çınlaçları yapmak icin kullanıldı. Bu koşuyolu çınlaçlarının tasarımları ayrıntılı olarak sunuldu. Bükülme kayıpları ve çiftleme oranları IİM kullanılarak hesaplandı. Dalgakılavuzu çınlaçlarının analiz ve tasarımı sırasında taramalı uç mikroskoplarında kullanılabilecek yeni bir mesafe sensörü önerildi. Sensör yüksek finesli bir mikro halka çınlaçının çıkıs tayfındaki bükülme nedenli degişiklikleri izleyerek çalışmaktadır. Çalısma prensipleri ve hasasiyet hesapları ayrıntlı olarak ele alındı.

119000 kadar büyük Q-faktörlerine sahip YÜS çınlaçları elde edildi. Bu YÜS sırt dalga kılavuzlarına dayalı çınlaçlardan bu güne kadar elde edilen en yüksek Q-faktörüdür. 43 kadar büyük fines değerleri ve 15 dB modülasyon derinlikleri elde edildi. Yarıçaplar 500 μm den 20 μm ye düşürülünce, serbest tayf aralıkları 0.2 nm den 3.0 nm ye çıktı. Bu çınlaçların termooptik akordlanmaları ayrıca incelendi. Yuksek Q-faktörlü bir çınlaç dalgaboyu seçici optik bir anahtar yapmak için kullanıldı. Çınlaç termooptik olarak tüm serbest tayf aralığı üzerinde yanlız 57 mW uygulayarak akord edilebilmektedir. Cihaz 210 kHz 3 dB kesim frekansıyla dalgaboyu seçici optik anahtar olarak çalışabilmektedir. Ayrıca iki dalgakılavuzlu koşuyolu çınlaçlarını kullanarak dalgaboyu ekleme/düşürme filtreleri geliştirildi. Daha iyi filtreleme özellikleri elde etmek icin asimetrik yatay çiftleme kullanıldı ve -10 dB kadar düsük çapraz sızma değerli ve 51000 Q-faktörlü filtreler elde edildi.

Son olarak bir tabaka aktarma yönteminin YÜS için kulanılmasını ele aldık. Böyle bir tabaka aktarması YÜS yapısındaki silisyum tabakanın arka yüzeyinin ileri işlemler için kulanılmasını sağlamaktadir. Bu metod ile önceden üretilmiş YÜS dalgakılavuzları aktarılarak melez silisyum-polimer dalgakılavuzları oluşturuldu. Benzocyclobutene (BCB) polimeri yapıştırmak için kullanıldı. Daha sonra, metod YÜS M-Z modülatörlerine teknolojinin olası başka kullanımlarını kesfetmek için uygulandı. Ayrıca polimer ve silisyum dalgakılavuzlarına dayali asimetrik dikey çiftleyicileri inceledik ve melez bir teknoloji kullanarak ürettik.

Anahtar sözcükler: Tümleşik optik, Yalıtkan üstü silisyum teknolojisi, Optik dalgakılavuzları, Polarizasyon ayıraçları, Halka çınlaçları, Koşu yolu çınlaçları, Mesafe sensörü, Dalgaboyu ekleme/çıkarma filitrelerı, Melez bütünleştirme, Yonga yapıştırma, Mach-Zehnder modülator, Asimetrik dikey çiftleyici .

Acknowledgement

I would like to express my deepest gratitude to Prof. Dr. Atilla Aydınlı for his supervision, guidance and encouragement throughout the research work presented in this PhD thesis. Without his friendly attitudes, it would be harder for me to survive my PhD thesis.

I would like thank Prof. Dr. Nadir Dağlı for his significant contribution and helpful discussions during his visits. I also would like thank him for providing us with some of the masks and BCB polymer used in fabrication. I would like also thank Asst. Prof Dr. Cem Öztürk for his help at the early stage of the development of layer transfer method.

My many thanks are to members of integrated optics group for forming a friendly and hardworking research environment. My special thanks are to Aşkin Kocabaş and Dr. Aykutlu Dâna for their help during some of the measurements and Coşkun Kocabaş for his useful discussion during the design of some of the devices. I would like also thank Murat Güre and Ergün Karaman for their effort to make Advanced Research Laboratory operate 7 days of the week and 24 hours of the day.

My many thanks are to my friends, Özgür Çakır, Feridun Ay, M. Ali Can, Kerim Savran, and Sefa Dağ for being supportive and funny.

Finally, I would like to thank my family living in Van. They have given continuous support throughout my life even they continuously complain due to my rare and short visits.

I would like to dedicate this thesis to my wife, Evla for her never fading love and support over the passing more than 8 years.

This work was supported by a Bilkent University Research Grant, (Code: Phys03-02) and The scientific and technological council of Turkey, (TÜBİTAK).

Contents

List of Figures

List of Tables

Chapter 1

Introduction

1.1 Integrated Optics

Photonics is the name for the science and the technology of manipulation of photons, quanta of light. It is also known as optoelectronics. Fiber optics and integrated optics can be categorized as sub fields of photonics and deal with its different aspects. As the name suggests, devices made out of optical fibers are in the scope of fiber optics. On the other hand, integrated optics describes planar integration of all miniature optical devices on a chip or wafer.

The relation between fiber optics and integrated optics can be understood as follows. Optical fibers have become more commercial and widely used as their optical attenuation was reduced to negligible levels. This implementation resulted in world wide telecommunication networks, in which, signals transmitted with higher bit rates at the speed of light. Integrated optical circuits (IOC) that comprise various components used for different functions are key elements at the beginning or end points of these optical fibers. IOC's are required to manipulate the transmitted optical signals. Detection, generation, modulation, switching, multiplexing and demultiplexing are the mostly performed manipulations. Speed and low cost are the main requirements that an effective IOC should comply. Apart from telecommunications, integrated optical devices have started to find applications as temperature, pressure, displacement, humidity, chemical and even biological sensors due to their potentially high sensitivities.

There are two types of IOC's namely hybrid and monolithic IOC. Two or more materials are integrated together in a hybrid IOC while, a single material is used for all components of a monolithic IOC. The materials implemented as IOC's are generally categorized as optically active or passive. Optically active refers to materials that are capable of light generation. To fabricate a laser one would need such a material. The most common materials to make lasers are gallium aluminum arsenide, $Ga_{1-x}Al_xAs$ and gallium indium arsenide phosphide $Ga_xIn_{1-x}As_{1-y}P_y$ [1]. There are also others. On the other hand, materials like lithium niobate, $LiNbO_3$, silica glass, silicon and most polymers are optically passive materials. In an IOC based on one of these materials will need a hybrid integration with an optically active material. Although, these optically active semiconductors can be engineered for generation of light with a specific wavelength and are the materials of the multilayered heterojunction lasers, very expensive and sophisticated techniques are needed to grow them, such as molecular beam epitaxy (MBE) or metal oxide chemical vapor deposition (MOCVD). On the other hand, silicon, silica glass and polymers do not require such expensive growth techniques.

Optical planar waveguides are the building blocks of IOC's. Apart from their use as optical interconnects between individual devices, they are also needed to realize many types of devices such as directional and multimode interference couplers, Mach-Zehnder interferometers and access components of detectors and lasers in IOC‘s, etc [2, 3]. Planar waveguides are designed in different types and geometries depending on their function and material used. The loss characterization is the key step when analyzing a waveguide. Losses as large as 2-5 dB/cm for GaAlAs systems, 0.5 dB/cm for $LiNbO_3$, and 0.1 dB/cm for silicon based optical waveguides are possible [4].

Integrated optical devices can also be classified in terms of their type of operation. Characteristics of passive devices can not be manipulated after their fabrication while, some physical effects can be implemented to realize active devices. Ability to tune, modulate or alter characteristics of a device may be very crucial. Apart from elimination of malfunctions due to some errors in design and fabrication, such an ability can be used to realize some of the key devices for a IOC, such as modulators and switches. Electro-optical, thermo-optical, acousto-optical, opto-mechanical and all-optical are the names of mostly used physical effects in fabrication of active devices. Electro-optic effect generally known as Pockel's effect changes refractive index of the material linearly and modulation speeds of a few GHz can be achieved through implementation of this effect [5, 6]. All III-V semiconductors, $LiNbO_3$, and some specially synthesized polymers have this effect inherently and this effect can be given to some of materials (silica glass and some polymers) by poling them [7]. Although, silicon lacks electro-optical effect, modulation speeds up to 1 GHz have been recently demonstrated by Silicon Photonics Group at Intel through the free-carrier injection, an slower type of electro-optical effect [8]. Injection of free carriers both changes refractive index and increases optical attenuation. Another type of electro-optical effect is the electro-absorption in which bandgap of a material may change under applied electric field and lead absorption of light. Finally, only modulation speeds a few hundred kHz have been achieved, thermo-optical effect is straightforward and easy to implement nearly to all type of materials [9, 10]. Silicon is one of the materials having large thermo-optical coefficient [11].

1.2 Silicon Integrated Optics

Silicon, the basic material of electronics industry is rediscovered nowadays for its potential use in photonics and integrated optics. The research activity in silicon integrated optics have been speeding up during last decade and even getting interest of leading industrial companies. Use of silicon as in microelectronics has been a well established technology for many decades. It is commercially available in high-quality and at low-prices. Increasing research efforts for silicon based integrated optics should be considered as a natural consequence.

The developments in silicon materials technology [12] also initiated these research activities. Since late 80's several methods of growing or fabricating thin films of high optical quality on silicon substrates have been developed. These methods are epitaxial growth of silicon based alloys with tailored optical properties (SiGe-heterostructures [13]), doping silicon growth of silicon based dielectrics (silica, [14] siliconoxynitride(SiON) [15] and germano silica [16]) and finally fabrication of high quality silicon-on-insulator wafers. In the following, we will briefly explain first three techniques and their application to integrated optical devices. Material and optical properties of SOI are then discussed and a summary of integrated optical devices realized so far is given.

Si-Ge heterostructures are generally fabricated through molecular beam epitaxy (MBE) [17] or chemical vapor deposition (CVD) growth [13, 18] techniques. Germanium ($n \simeq 4.3$) slightly increases the refractive index of silicon ($n \simeq 3.5$). Refractive index of $Si_{1-x}Ge_x$-alloy is given by $n_{SiGe} \approx n_{Si} + 0.3x + 0.32x^2$. Epitaxial growth of thin strained SiGe-layers can be done due to very similar lattice constants of Si and Ge atoms. Waveguides on MBE-grown strained $Si_{0.99}Ge_{0.01}$ layer have been fabricated with losses 3-5 dB/cm at $\lambda = 1.3\mu m$ [17] and with reduced loss of 0.6 dB/cm on CVD-grown $Si_{1-x}Ge_x$ layers [19]. The high cost and difficulty in growing of SiGe by MBE and CVD are current problems of this material. SiGe is a good platform for photodetector fabrication and these devices have been integrated with SOI waveguides [20]. SiGe is an important material due to its compatibility with SOI technology.

Light guides in a doped silicon waveguide when the doping level of the epilayer is lower than the doping level of the substrate. These waveguides generally suffer from high optical losses, waveguide loses due to defects formed during doping process in the range of 15-20 dB/cm have been measured for rib waveguides with epilayers of thicknesses between $7\mu m \leq H \leq 43\mu m$ and doping levels of a few $10^{14} cm^{-3}$ for epilayer and $10^{18} - 10^{19}\ cm^{-3}$ for substrate [21]. These high losses may be further decreased by using larger dimensions and a very highly doped substrate, which will decrease absorption to the substrate. The optical losses as low as 1.2-1.5 dB/cm have been achieved with such waveguides [22].

Plasma enhanced chemical vapor deposition (PECVD) or flame hydrolisis(FHD) techniques are used to deposit silica or SION layers on silicon or quartz substrates. The substrates are annealed to about 1000 °C to eliminate source of optical losses. The silica layers are designed such that refractive index differences of 0.5-1.5 percent are possible and waveguide losses ranging from 0.01 dB/cm to 0.07 dB/cm are possible [14]. Meanwhile, SiON layers have refractive indices between 1.45 (silicon-oxide refractive index) and 2 (silicon-nitride refractive index) and the typical losses for SiON based waveguide technology are 0.1 dB/cm for slab waveguides and 0.2 dB/cm for channel waveguides. Waveguide bend radius as small as 1.5 mm are possible due to the high refractive index difference between SiON layer and its cladding [15]. This is the main advantage of SION over silica layers.

Among all the silicon based optical materials, SOI has very unique optical properties. This mainly due to its very unique structure. Crystalline silicon is the guiding layer. The large refractive index difference between silicon($n \simeq 3.5$ and $SiO_2(n \simeq 1.45)$ makes fabrication of highly confined waveguides possible. Bulk silicon is perfectly transparent at the optical telecommunication bandwidths (around 1.3 μm and 1.55 μm). SOI based IOC's are fully compatible with silicon electronic integrated circuit. This compatibility is one of the most important advantages of SOI IOC's over those based on other technologies.

SOI integrated optics technology has developed very rapidly, because it rises on the well-established silicon integrated electronics micromachining technology. New device fabrication technologies are not needed. SOI wafers are now commercial on the market with their high quality and relatively low prices. Among many fabrication techniques of SOI substrates, only two of them has good enough material properties to become commercial. These techniques are Separation by IMplemented OXygen (SIMOX) technology and Bond-and-Etchback (BE-SOI) technology [23]. SOI material structure is defined as a relatively thin silicon($n \sim 3.5$) top layer separated from a very thick silicon substrate by a thin SiO_2 ($n \sim 1.45$) layer. The challenge in SOI wafer fabrication is to make the top silicon layer having the same quality as bulk silicon. The criteria that need to be optimized are defect density, layer interface and silicon surface roughness and thickness uniformity.

The flow of SIMOX process is as follows; an oxygen ions (O^+) beam of doses as high as 1-2x10^{18} ions cm^{-2} is accelerated to penetrate into a silicon wafer surface by about 0.1-0.2 μm under an electrical potential of $150 - 200$ keV to produce a SiO_x insulating layer with $0.1 - 0.5$ μm thickness [24]. This is then followed by a high temperature anneal at $1250 - 1300$ ^{0}C. This annealing step facilitates the crystallization of the damaged thin top silicon layer and formation of a relatively sharp Si and SiO_2 interface. In SIMOX technology different Si thicknesses become available by implantation at different O^+ doses and under different potentials. In any case, the layer thickness obtained by SIMOX is limited and does not exceed 0.2 μm. The Si thickness uniformity is well controlled an is around ± 5 nm.

BESOI technique differs in many ways from SIMOX. The general processes flow can be described as follows. One or both silicon wafers are thermally oxidized. Then, wafers are hydrophilicly bonded to each other. The oxide layer then becomes the buried insulator layer. After that point, different BESOI techniques uses different ways to thin one of the silicon wafers to get the desired silicon film thickness. Generally thinning is achieved by polishing the wafer until the desired thickness is obtained [12]. This thickness can be as small as 1 μm or as large as a few hundred micrometers. Etching mechanisms enhanced by particular etch stop layers are also being utilized [12, 25]. After all that, the nonuniformity of the silicon film thickness may still become a problem due to lack of sensitivity of polishing and etching mechanisms utilized in BESOI techniques. The average thickness uniformity is ± 0.5 μm.

The smart-cut (or Unibond) technology of Soitec Inc. have brought a brilliant solution to the nonuniformity problem [26]. This problem especially becomes very drastic in the case of silicon top layers of a few micrometers. In this technology [25], a wafer is implanted by hydrogen ions of doses $2x10^{16}$ - $1x10^{17}$ cm^{-2} before oxidation. The wafer is bonded to a second one as described above, and followed by a two step heat treatment at temperatures of $400 - 600$ ^{0}C. This leads the hydrogen ion implanted wafer to split into one thin silicon layer bonded to the other wafer with SiO_2 between them and a thick reusable silicon layer (Fig. 1.1). A fine polishing of the top silicon layer ends the process. The thickness uniformities as good as those achieved in SIMOX technology is obtained with Unibond

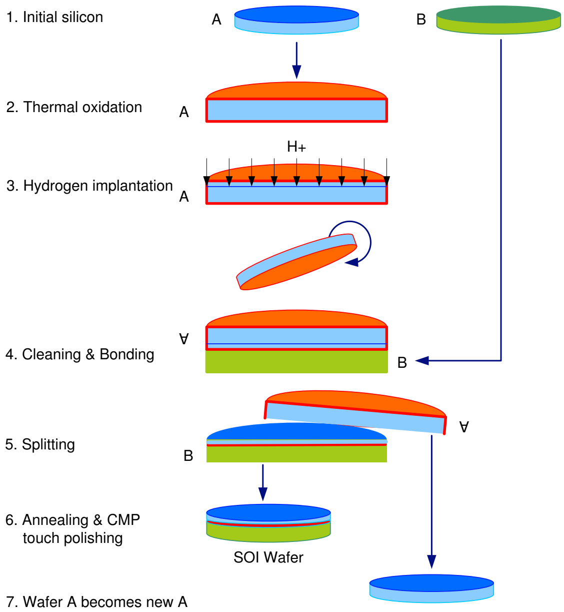

Figure 1.1: The Soitec's Unibond process to fabricate SOI wafers. (from archive of Soitec.)

process.

As a conclusion to SOI wafer fabrication techniques, we can say that SIMOX process results in good SOI structures for both digital and analog integrated electronic circuit applications but is not preferred for integrated optics systems in general. On the other hand, BESOI wafers are better for integrated optic devises and systems with providing defect densities as low as bulk silicon and various silicon layer thickness options. Finally, Unibond BESOI wafers resulting in both very uniform thicknesses and low defect densities are very appropriate and preferred in both integrated electronic and optical applications including microprocessors, smart power devices, optoelectronic circuits, liquid crystal and high-resolution displays, MEMS and wireless communication circuits [26].

Starting from the beginning of 90's, optical properties of SOI waveguides have been investigated and a large number of SOI based passive and active integrated optical devices developed. Waveguides on SOI was first realized with relatively high propagation losses, later by means of advanced fabrication techniques this value decreased to 1 dB/cm, and then to 0.5 dB/cm, and finally to 0.1 dB/cm

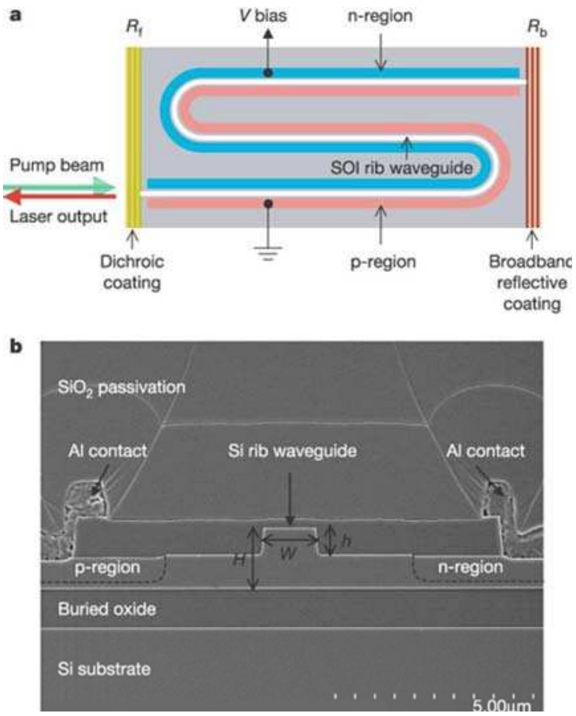

Figure 1.2: Si raman laser based on an SOI rib waveguide. (from reference [39].)

using large cross-section SOI rib waveguides [27, 28, 29, 30]. Obtaining losses around 0.5 dB/cm is typical for single mode waveguides with silicon top layers larger than 4 μm. The dependence of propagation loss on the thickness of insulator (SiO_2) was also studied [31].

Apart from optical waveguides, a number of SOI guided wave optical devices have also been demonstrated. Some examples are integrated 3 dB directional couplers with excess insertion loss of 1.9 dB [32], 5x9 star couplers with loss of 1.3 dB [33], asymmetric Mach-Zehnder type wavelength filters with -18 dB crosstalk [34], optical switches based on thermo-optic effect [9, 35] with 5 μs rise time and 150 mW switching power [35] and low-loss multimode couplers [12]. Furthermore, submicrometer thick SOI wafers were studied and many ultra compact devices were realized with Si nanowire waveguides [36, 37]. These wafers were even used to fabricate photonic band gap materials or crystals for telecom wavelengths [38]. Recently, implementing free-carrier injection technique, SOI modulators were demonstrated to exceed 1 GHz psychological limit [8]. Furthermore, researchers from Intel fabricated first all silicon continuous laser operating with Raman scattering in silicon [39] (Fig. 1.2). All these developments in silicon photonics lead the expectations for a silicon monolithic IOC and increases the research activity in the field.

1.3 Contribution of our Research Work

As a part of the research activity by academic and industrial institutions in the field of silicon photonics on SOI wafers, we have designed, fabricated and characterized a class of monolithic and hybrid silicon integrated optical devices. In this thesis work, fundamental physical principles used in the design of the devices are summarized, design methods applied are discussed in detail, fabrication and characterization techniques employed are explained and finally results of all the realized devices are presented through discussions. In *chapter 2*, we briefly discussed the basic principles, design methods, device fabrication processes and techniques to test these devices.

We have realized during our studies on modal properties of SOI single mode rib waveguides that their birefringence can be geometrically controlled as their size decreasing to 1.5 μm or smaller. We have utilized this property of SOI rib waveguides to develop a set of compact polarization splitters given in *chapter 3*. Polarization splitters find applications in optical systems where polarization states of light are important. Some of these systems are used in communications, sensing, data storage, imaging and signal processing [40, 41]. For many birefringent optical devices, separation of orthogonal polarization states is a straightforward solution where polarization splitters can be used. So far, directional couplers, asymmetrical Y-junction structures, multimode interference couplers have been adopted as polarization splitting components. These devices have been realized on silica, $LiNbO_3$, GaAs/GaAlAs, InGaAsP/InP and polymer materials [40, 42, 43]. Material birefringence, stress induced birefringence in ion exchanged waveguides and selective attenuation of orthogonal polarization states using metal over a waveguide have been employed in these polarization splitters. A polarization splitter based on two-dimensional grating coupler etched in an 220 nm thick SOI waveguide has also been realized [44]. Even micro opto- electromechanical systems (MOEMS) have been used for fabrication of polarization separators [43].

Our passive, TE/TM splitting devices are based on a directional coupler design. Our splitters are important because they are the first devices realized on SOI that splits TE and TM modes guiding in silicon which is known to have no bulk material birefringence.

With the goal of developing SOI optical resonators that are high-Q, compact and functional, we discuss and summarize waveguide ring resonators in *chapter 4*. Micro-ring resonators are of great interest due to their compactness and stability with respect to back reflections and high wavelength selectivity, which are key features for various applications. Due to these superior characteristics optical ring resonators are used in massive integration of many optical devices, including channel dropping filters [36], WDM multiplexers [45], on-off switches [46], chemical and pressure sensors, ring lasers [47]. Ring resonators have been realized in various waveguide materials systems both with low index contrast [48] as well as high index contrast [49]. Among the high index contrast material platforms, silicon-on-insulator (SOI) provides a low cost alternative with the possibility of integration with mature silicon microelectronics processing technology. Most of the effort on SOI systems has been devoted to realization of ring resonators using strictly single mode optical wire waveguides with ultra small dimensions in the nanophotonic regime [50]. However, as the dimensions get smaller, fabrication tolerances become harder to meet. With submicron cross sections, coupling in and out of ring resonator devices as well as minimization of propagation losses become a major hurdle [51]. Used as a channel dropping filter, a ring resonator should have low propagation and bend losses which lead to high Q values for better channel selectivity. Therefore, design and realization of SOI ring resonators using single mode SOI waveguides with large cross sectional areas is crucial. This approach of making use of the large-index contrast with larger cross sections allows the design of small radius rings with lower propagation losses and higher Q values as well as achieving better fabrication tolerances.

In *chapter 4*, the key issues in designing a waveguide resonator are highlighted.

The calculations and BPM simulations for SOI resonators are presented. Additionally, the same design tools were integrated with analytic and finite element method simulations to design an integrated optical displacement sensor using micro-ring resonator. All the issues related to the sensor are also given in *chapter 4*.

In *chapter 5*, we give all the measurement results on fabricated SOI racetrack resonators. We demonstrated resonators of Q values as high as 119000 and finesse values as high as 42. Compact resonators with radius of 20 μm resulting free spectral range of 3 nm were also obtained. These devices operates as wavelength drop filters. Thermooptical modulation and tuning of these resonator were also studied. A resonator wavelength selective optical switch with low operation power of 17 mW and high modulation speed of 210 kHz was realized. This is the fastest SOI thermooptical device with no differential control. Finally, wavelength add/drop filters based on a resonator of two bus waveguides were tested to have crosstalk as high as 10 dB.

The thesis continues with *chapter 6* which discuss the use of a layer transfer method for SOI wafers and a set of devices realized with this method. So far, all SOI integrated optical devices such as directional and multimode interference couplers for beam splitting, thermo-optic modulators have been fabricated through processing the top Si layer. However, it is clearly desirable to have the capability to process both sides of the device for further electronic and/or optical integration. Processing both sides of the silicon layer may result in novel devices while improving performances of some of the existing ones. Transfer of the silicon layer in SOI has recently been studied, but has not yet been used for integrated optical device fabrication [52]. In this chapter we introduce the use of a layer transfer method, which was successfully employed in GaAs-AlGaAs platform [53] for SOI wafers. Such a layer transfer results in the possibility of using the back side of the silicon layer in SOI structure for further processing. We developed silicon-polymer waveguides, M-Z modulators, asymmetric vertical couplers with this layer transfer method. Finally, the conclusion chapter summarizes all the achievements and gives further suggestions.

Chapter 2

Tools of Integrated Optics

This chapter is devoted to the summary of basic physical principles and device fabrication and characterization techniques. These principles and techniques were implemented in the design and realization of integrated optical components discussed in this thesis work.

2.1 Basic Principles and Design

The basic components of integrated optics are planar optical waveguides. Slab waveguides show light confinement in one of the transverse dimensions. One will need rectangular waveguides when confinement in both of the dimensions is intended. Light propagates in optical waveguides as modes. They are spatial distributions of light during propagation. A waveguide can have single or multi modes. Each mode of a waveguide has a different propagation constant or effective refractive index.

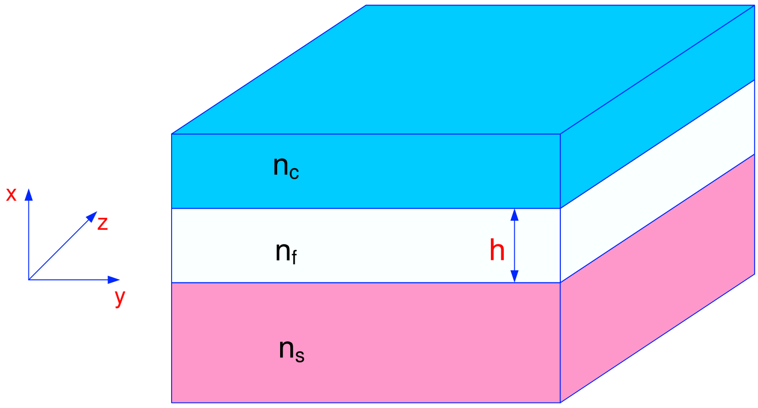

Figure 2.1: General slab waveguide structure with coordinate axis.

2.1.1 Slab Waveguides

Slab waveguides are known as the simplest of waveguides. Slab waveguides have a minimum of three different layers (Fig. 2.1). For guidance of light, n_f, refractive index of guiding film must be larger than n_c, refractive index of cladding layer and n_s, refractive index of substrate layer,

$$n_f > n_s \geq n_c. \tag{2.1}$$

The slab waveguide is said to be *symmetric* when n_s=n_c and *antisymmetric* otherwise, $n_s \neq n_c$.

The slab waveguide supports a definite number of optical modes, and at least one, if it is symmetric. These modes are calculated from Maxwell's equations through the application of boundary conditions. However, the same modes for slab waveguides can be found by using ray optics concepts. Detailed discussion of ray optics approach can be found in [54]. For a through analysis, one needs to solve well known Maxwell equations for a source free (ρ=0, $\vec{J}$=0), linear (ϵ and μ are independent of $\vec{E}$ and $\vec{H}$) and isotropic medium. Maxwell equations are strongly coupled. They can be decoupled through a standard procedure of creating a single second order differential equation. This procedure when applied to the Maxwell equations leads to the wave equation, which is

$$\nabla^2\psi - \mu\epsilon\frac{\partial^2\psi}{\partial t^2} = 0 \tag{2.2}$$

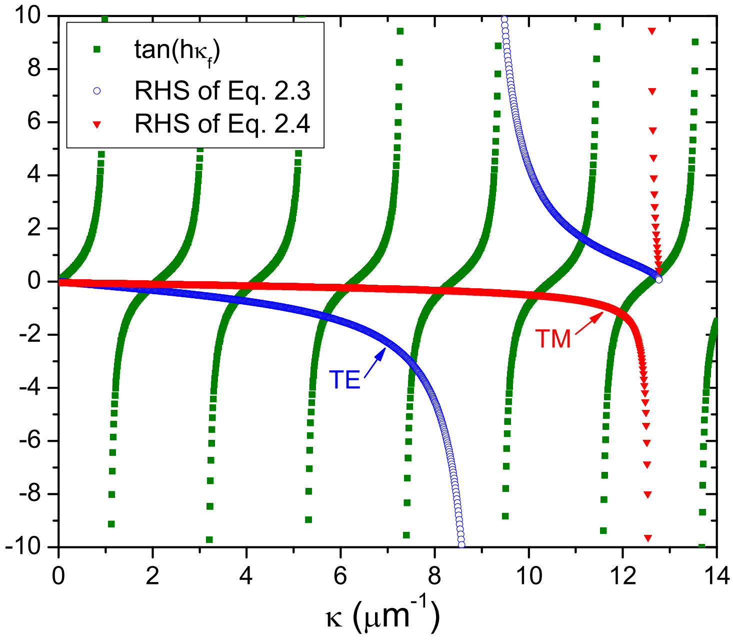

Figure 2.2: Graphical TE and TM solutions for a symmetric SOI slab waveguide of 1.5 μm thickness.

where ψ stands for either of $\vec{E}$ or $\vec{H}$. After that, the wave equation should be solved for the slab waveguide in Fig. 2.1. The parameters are chosen such that $n_f > n_s > n_c$ and the guiding layer has thickness h. Rectangular cartesian coordinate system are utilized to make the problem simpler. z is always chosen to show propagation direction. There are two cases emerging from geometry, either $\vec{E}$ or $\vec{H}$ is parallel to the layer interfaces, which define TE or TM polarizations, respectively.

The detailed slab waveguide analysis can be found in many textbooks [6] and also in [54]. In summary, oscillatory fields are defined in terms of propagation constants of the waveguide and frequency of light. Substitution of these fields into wave equation and application of boundary conditions leads to so called eigenvalue equation for propagation constant, β. The equation for TE polarization is

$$\tan(h\kappa_f) = \frac{\gamma_c + \gamma_s}{\kappa_f[1 - \frac{\gamma_c \gamma_s}{\kappa_f^2}]} \tag{2.3}$$

The similar equation for TM polarization is

$$\tan(h\kappa_f) = \frac{\kappa_f[\frac{n_f^2}{n_s^2}\gamma_s + \frac{n_f^2}{n_c^2}\gamma_c]}{\kappa_f^2 - \frac{n_f^4}{n_c^2 n_s^2}\gamma_c\gamma_s} \tag{2.4}$$

where γ and κ are defined as

$$\begin{array}{llll} \text{Attaneuation} & \text{Coefficient,} & \gamma = \sqrt{\beta^2 - k_0^2 n^2} & if \quad \beta > k_0 n \\ \text{Transverse} & \text{Wavevector,} & \kappa = \sqrt{k_0^2 n^2 - \beta^2} & if \quad \beta < k_0 n \end{array} \tag{2.5}$$

These equations are also called the characteristic equation of TE and TM modes of a slab waveguide. They are transcendental equations and should be solved numerically or graphically. These complex equations are simplified for the special case of a symmetric waveguide. The eigenvalues of these equations, β_{TE} and β_{TM} can be found for a slab waveguide with a definite thickness h and index values for its layers using either a numerical or graphical software in a personal computer as we did for a symmetric SOI slab waveguide of 1.5 μm thickness in Fig. 2.2 [55].

2.1.2 Single Mode Rib Waveguides

The slab waveguide is easy to analyze and useful to understand the basic concepts of optical waveguides. However, it has no lateral confinement and this reduces the number of applications where it can be used. The alternatives are circular fibers and dielectric rectangular waveguides. The fibers are not compatible with planar processing technology, such as planar chips, which are backbones of integrated electronics. Light in a slab waveguide can be laterally confined and resulting structure is the so called dielectric rectangular waveguide. The rectangular waveguides have several geometric shapes leading to lateral confinement. These shapes are rib, ridge, channel and diffused [54]. The optical waveguides that we employed in this thesis are rib waveguides. The mode analysis of the rectangular waveguides is a bit cumbersome and exact analytical solutions can not be so easily found, instead, some simplified analytical results based on the solution of the wave equation are further corrected by some perturbation techniques. What is actually needed are some simple methods which will be useful

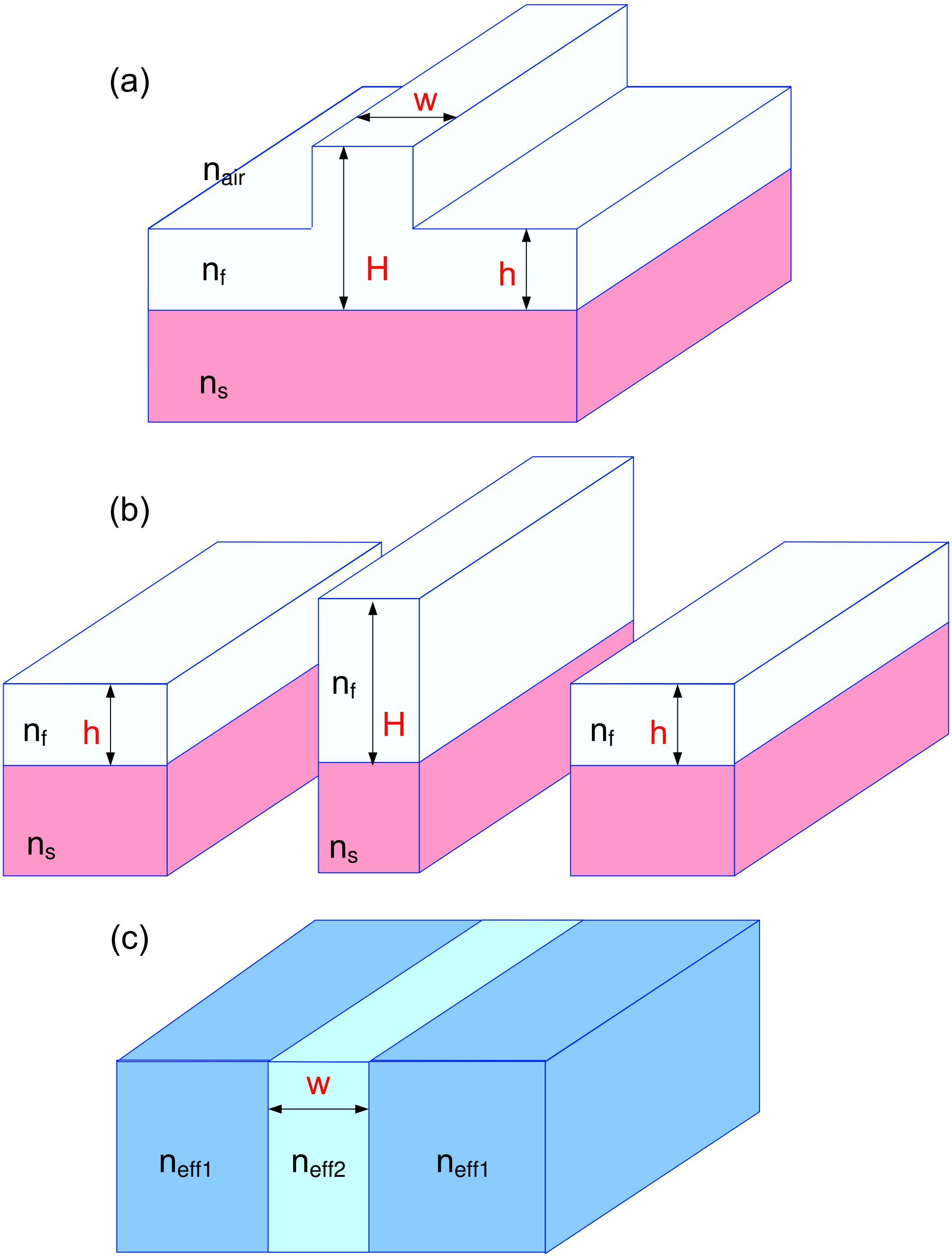

Figure 2.3: Effective index analysis for a rib waveguide of air cladding. (a) The rib waveguide with its critical dimensions. (b) Three slab waveguides constructed from the rib waveguide. (c) Artificially constructed slab waveguide using effective index of three slabs.

for design purposes. There are two basic waveguide design tools, namely effective index method (EIM), which is a relatively easy method to apply and useful for most of the design purposes and the beam propagation method (BPM), which is a numerical simulation method. We generally designed our SOI rib waveguides by EIM. BPM was used for fine tuning of the waveguide characteristics.

A rib waveguide can be analyzed using EIM as follows. A rib waveguide can be divided so that three slab waveguide are formed as seen in Fig. 2.3. The propagation constants of each slab are calculated from the characteristic equations (Eqs. 2.3 and 2.4) of the slab waveguide for desired polarization. The effective indices (n_{eff1} and n_{eff2}) are calculated for each slab through

$$n_{eff} = \frac{\beta}{k_0} \tag{2.6}$$

These effective indices are used to construct an artificial slab waveguide structure as in Fig. 2.3. After that, calculation of the β is repeated for the new structure using the equation for the orthogonal polarization and effective index is calculated by Eqn. 2.6. The resulting effective index is the effective index of the original rib waveguide.

Strictly single mode SOI waveguides requires sub-micrometer dimensions. These waveguides are also called nanowire waveguides. They generally have the same thicknesses of single mode SOI slab waveguides with values smaller than 0.3 μm. Although nanowire waveguides allow us to construct very compact devices, their very small dimensions lead to very high coupling losses between the waveguide and a single mode fiber which has a diameter of 9 μm. On the other hand, quasi-single mode waveguide propagation has been shown in SOI rib waveguides with large cross section that is dimensions of a few μms [56]. These waveguides have been used to realize many integrated optical devices that are compatible with SM fibers. For these quasi-single mode waveguides, *the single mode condition* which relates vertical and horizontal dimension of the waveguide by facilitating EIM can be stated as

$$t < c + \frac{r}{\sqrt{1-r^2}} \quad and \quad r > 0.5 \tag{2.7}$$

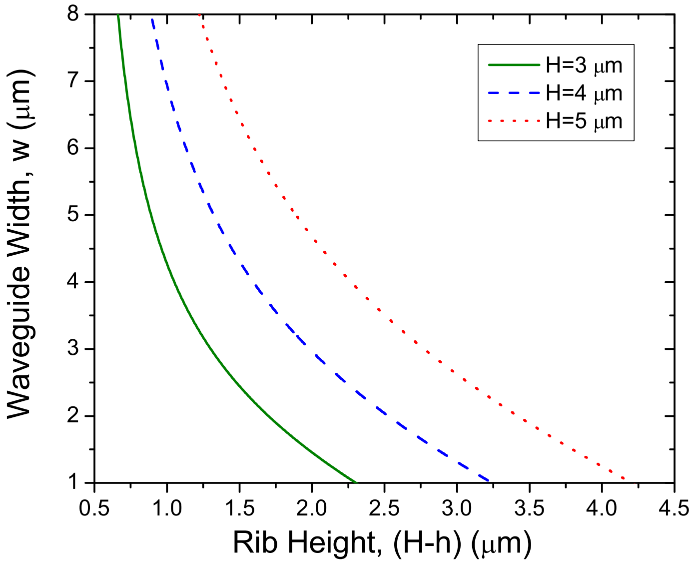

Figure 2.4: Waveguide width (w) versus rib height (H-h) calculated from SMC applied to SOI rib waveguides with oxide cladding. Results are shown for three different waveguide heights (H).

where

$$t = \frac{w_{eff}}{H_{eff}} \quad , \quad r = \frac{h_{eff}}{H_{eff}}$$

Details on how to find the effective width (w_{eff}) and heights (H_{eff}, h_{eff}) can be found in [54]. The relation in Eq. 2.7 leads to single mode propagation in horizontal (lateral) direction while $r > 0.5$ ensures propagation of only one mode in vertical (transverse) direction by avoiding deep etching of the waveguide. The constant c was defined as 0.3 in [56]. It was calculated from an approximation to a BPM simulation. However, it was later proposed that c values of 0 or -0.05 give better single mode condition for rib waveguide design purposes, [57].

The so called single mode condition given above can be used to design single mode waveguides with large cross-section (H $\geq$ 3 μm). One can plot the equation for specific waveguide heights. We did this for some representative height values in Fig. 2.4. Such a plot may be more practical during fabrication of waveguides. Although, the effective index method and the single mode condition may be found very practical, BPM simulations can give more accurate waveguide characteristics. Therefore, verification of the number of modes and effective indexes should be made by these simulations. We should note that these two methods are clearly not sufficient for design of SOI rib waveguide with cross-section in the order of 1 μm. These waveguides have very interesting characteristics that would be implemented in design of novel devices. We have used such waveguides in design of several devices and mostly preferred to use BPM simulations for waveguide analysis.

2.1.3 Beam Propagation Method

Unfortunately, analytical solutions are only available for a few simple waveguide structures. There are also some approaches based on some approximation, like effective index method that we discussed earlier. Most of the waveguide components and devices are too much complicated to have neither analytical solutions or be treated with approximation methods. Bend or tapered waveguides, y-junctions or couplers are such kind of components. Beam propagation method (BPM) provides numerical simulation of these components. It does not give approximate solutions. BPM can let us analysis even more complicated waveguides, for example the refractive index or a geometrical property of the waveguide may change along the propagation direction.

BPM simulates a structure by decomposing a spatial mode into superpositions of plane waves using discrete Fourier transforms [6]. The mode is reconstructed after the plane waves are travelled for a certain distance. Although BPM codes in a numerical package can be used for simple one-dimensional structures, commercially available BPM simulators should be used for fast analysis of more complex 2-dimensional structures. Polarization characteristics can also be studied with such simulators. We have used one of such simulators, BeamProp, for device designs [58]. This software allows the user to define many structures complicated in both geometry and index distribution in a cad layout (Fig. 2.5). An assorted set of field profiles are available to be launched to the defined structure. The software can also dynamically monitor many characteristics of the waveguide

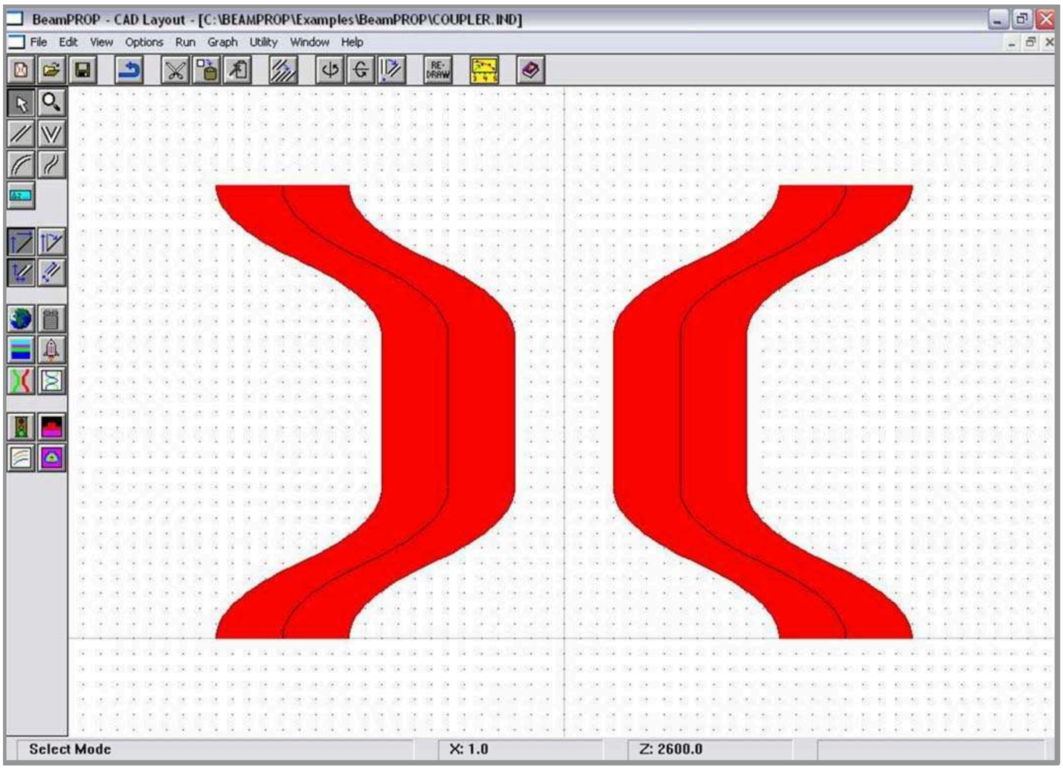

Figure 2.5: Cad layout of BeamProp software. We repeatedly used this software for the design and analysis of the devices discussed here.

structure including propagating mode powers, effective indices and waist of the propagating fields. The structure can be analyzed in one or two dimensional using scalar, vector or semi-vector BPM methods. Many waveguide structures can be integrated and their behaviors can be analyzed. For example coupling from a fiber to waveguide or between waveguides having materials of different dielectric constants.

2.1.4 Directional Waveguide Couplers

Optical tunnelling is responsible for the coupling of optical power from one waveguide to another one. The device composed of a pair of waveguides is called a waveguide coupler in general and *directional coupler* if the power exchange happens in a coherent fashion so that the direction of propagation does not change.

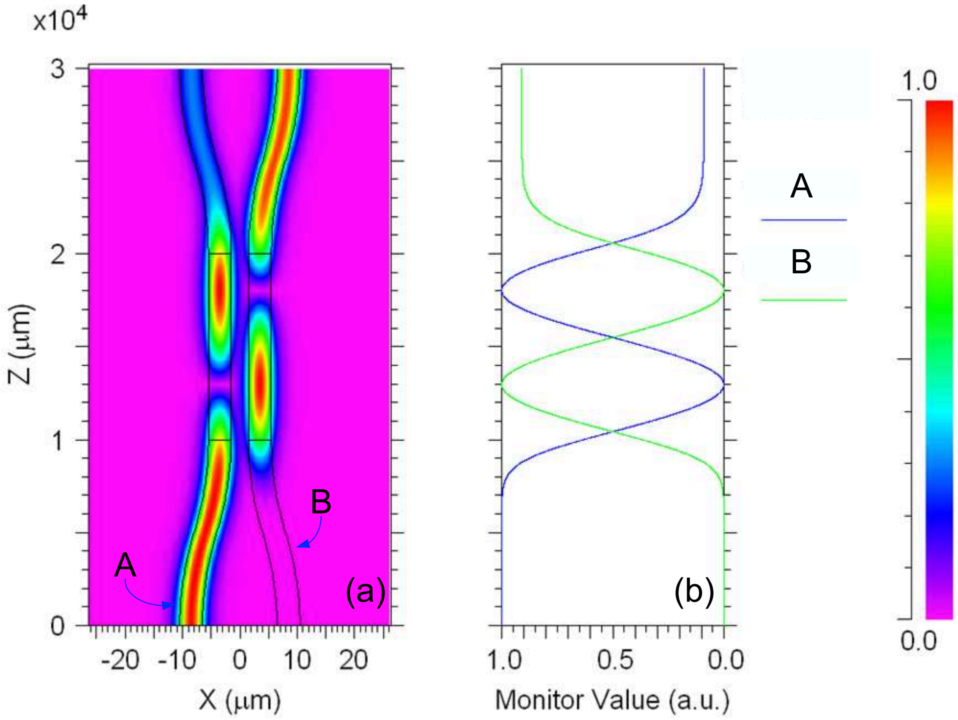

Figure 2.6: BPM analysis of a waveguide directional coupler. (a) X-Z contour map of coupler. (b) Monitored optical power in each waveguide as light propagates in the coupler.

Directional couplers are one of the fundamental waveguide devices used in integrated optic circuits. They have been used in circuits designed for power splitting, modulation or switching of light signals, wavelength filtering and polarization selecting. A directional coupler consists of two identical waveguides very closely placed, as in Fig. 2.6. The light incident at input of one of the waveguides couples to the other as it propagates and full coupling of the optical power is possible for long enough coupling length. Integrated optics uses coupled mode formalism to handle directional couplers. Coupled mode theory can describe the power exchange between all optical modes. When coupling occurs, the electromagnetic field propagating in a waveguide of a directional coupler is perturbed by the evanescent tail of that of the other waveguide. The coupled mode theory describes this perturbed field by superposition of unperturbed that is ideal modes of the waveguide. The basic coupled mode theory has been constructed on the scalar wave equation. What is computed with this method is coupling coefficient, κ, for a directional coupler design. When κ is calculated, the length required for full coupling can be determined.

We have demonstrated the coupled mode theory approach for a directional coupler with rib waveguide structure in [54]. Here we will give important results, detailed calculation can be found there or in [6]. The optical powers in waveguide A and B compromising a directional coupler exchange between each other. They can be defined in terms of coupling coefficient, κ as

$$P_A(z) = \cos^2(\kappa z) \tag{2.8}$$

$$P_B(z) = \sin^2(\kappa z) \tag{2.9}$$

The total power goes back and forth between two waveguides and the driven field (waveguide B) always lags 90^0 (See Fig. 2.6 for comparison). Using the above equations we can write for lengths satisfying $L\kappa = \pi/2 + q\pi$ complete energy transfer occurs where q is an integer. This length can be extracted to be

$$L = \frac{\pi}{2\kappa} + \frac{q\pi}{\kappa} \tag{2.10}$$

The length for $q = 0$ is called as *coupling length*, L_c. Non-integer q values leads couplings between 0 and 100 percent. κ (therefore L_c) is a strong function of g, the gap between waveguides, w, the waveguide width H, the waveguide height, h, the waveguide slab height and the refractive index difference between guiding layer and substrate. That is, a coupling factor is very specific to a specific coupler design. Therefore, coupled mode formalism may not be found practical enough in designing a coupler. Waveguides generally bend to couple and decouple. An effective coupling still takes place in these regions which brings further complexity to the analysis. These bends may cause bending losses and change the effective coupling constant and L_c. For these reasons, BPM has been used in all directional coupler analysis made for polarization splitters, racetrack resonators, etc in this thesis work. An example of coupler analysis using BPM is shown in Fig. 2.6.

2.2 Basic Fabrication Techniques

This section intends to give basic device fabrication procedures used in this thesis work. These procedures are generally common for all devices. We give details of recipes and refer them later on in the thesis. Some devices need some uncommon fabrication process and these processes are explained as these devices are discussed in coming chapters.

Preparation of SOI samples for further fabrication processes, photolithography, thin film deposition (dielectrics and metals) and etching etc. starts with dicing of pieces from a whole SOI wafer. All the fabrication processes were done in the class 100 facility of Department of Physics at Bilkent University. The pieces cleaved out from SOI wafers have sizes depending the device designs. We worked with chips with sizes ranging from 15x15 mm to 30x40 mm. Diced chips are cleaned through tri-solvent cleaning which includes use of successive application of trichloroethane (TCE), aceton (ACE) and iso-propanol (ISO) solvents. Details of this cleaning technique can be found in [54]. Chips are rinsed under running water for a while and blown with nitrogen then they are placed on a hot plate at 110 ^{0}C for 1 minute in order to evaporate the remaining monolayer of water on the chip surface.

2.2.1 Photolithography

We have used standard photolithography to transfer the device patterns from a mask to a chip. Masks have clear and opaque parts defining the patterns. In photolithography process, samples are first applied with some photoresist (PR), then the aligner is used to align sample and the mask, then an UV light source is used to expose the sample over the mask. After exposure, the samples are treated with developer solvent. This solvent dissolves the PR parts which are exposed, that is parts remained under the clear part of the mask during exposure, if the PR is *positive* [59]. While PR on the other parts are dissolved in the case of a *negative* PR.

The details of photolithography process done in our fabrication facility is as follows. The samples are put on the spinning chuck of the spinner tool (Karl Suss Model SM 120 Spinner) and a drop of 100 % HexaMethylDisilazene (HMDS) solution is put on the sample surface to enhance the adhesion of the PR to the sample and the sample is spun at speeds ranging from 2000 to 6000 rpm for 40 s so that HMDS is uniformly spread over the sample surface. We have used three kinds of PR throughout the thesis work. They are AZ MIR701, AZ 5214E and AZ TI35ES [60]. First one is a positive PR. The others can be processed as either positive or negative. After covering all of the sample surface with drops of a PR of our choice, the sample is once more spun at the same rate and duration. The uniformly PR covered samples are prebaked on a hot plate at a temperature around 100 °C for a duration of about 50 seconds to strengthen the sticking of PR to the sample and to solidify the PR. Actual bake temperature and duration depends on the type of PR and given in the tabulated recipes for each PR (Table 2.1). The resulting PR film may have a thickness in the range of 0.75 to 3.5 μm. We can measure thicknesses after photolithography and developing steps using Sloan Dektak 3030ST Surface Texture Analysis System. For both mask alignment and exposure we used Karl-Suss MJB-3 HP/200W Mask Aligner. This system uses a 500 W mercury xenon high pressure lamb as its light source and in principle can define dimensions as small as 0.8 μm with 0.1 μm accuracy. The mask is loaded on the mask holder of the aligner and the samples and patterns on the mask are aligned such that the straight alignment marks on the mask are parallel or perpendicular to the edges of the rectangularly cleaved samples. The SOI samples used have surfaces on $< 100 >$ plane and the strips are defined on that plane also. Such an alignment may be critical especially if an anisotropic etching (i.e. we used KOH for some device fabrications) is used later on. After exposure, the exposed positive PR parts are dissolved in 25 percent aqueous AZ 400K developer solution and this results in realization of the mask patterns in the PR film. When a negative PR is used, a second bake at 120 °C for 2 mins and a float (no mask) exposure of 1 or 2 minutes are required before application of developer solution. The samples with PR patterns on their surface must pass through another bake (called postbake) at 120 °C for several mins if the patterns are going to be used as a mask in an etching process. On the other hand, no postbake is required if a thin metal film deposition and a liftoff process is used.

PR Label ⇒	AZ MIR701	AZ 5214E	AZ 5214E	AZ TI35ES	AZ TI35ES
Type of Use	Positive	Positive	Negative	Positive	Negative
Spin Speed (rpm)	6000	4000	4000	5000	5000
Spin Dur. (s)	40	40	40	40	40
Prebake Temp.(°C)	90	110	110	100	100
Prebake Dur.(s)	60	50	50	120	120
Expos. Dur.(s)	54	40	25	120	40
2^{nd} Bake Tem.(°C)	110	-	120	-	120
2^{nd} Bake Dur.(s)	60	-	120	-	120
F. Expos. Dur.(s)	-	-	70	-	110
Develop Dur.(s)	25	40	40	60	60
PR Thickness.(μm)	0.75	1.40	1.40	3.50	3.50
Reference No.	PL1	PL2	PL3	PL4	PL5

Table 2.1: Recipes of three kind of PRs that are used in fabrication processes.

2.2.2 PECVD Grown Dielectric Films

Si_3N_4 and SiO_2 dielectric films that we used for several purposes were grown in the plasma enhanced chemical vapor deposition (PECVD) system available at our facility. In our device fabrication, SiO_2 layers were employed as upper cladding of SOI rib waveguides, passivation layers between waveguides and metal films and separation regions between Si slabs and polymer waveguides. On the other hand, we used Si_3N_4 layers only as a masking material during KOH etching. PECVD grown silicon nitride (Si_3N_4) films are known for their very high resistance to KOH solution, while PECVD SiO_2 is not a good masking material for KOH etching. Apart from its resistance to the KOH solution, simple processing of silicon nitride in dilute hydro fluoric acid (HF) solutions makes it the primary choice for masking material to be used in KOH based etching processes.

The use of SiO_2 layers lets us to fabricate devices based on symmetric SOI rib waveguides. SiO_2 cladding also preserves waveguide facets from any damage during cleavage of devices. Thickness of grown layers using PECVD can be controlled with a good accuracy. Realization of some devices (couplers, etc.) needs precisely defined gaps between two waveguides or subcomponents. These gaps may be on a submicrometer scale for some device designs. In lateral placement of device elements, such gaps are defined through photolithography and a subsequent etch of the material. Therefore, accuracy of these gaps totaly depend on lithography resolution. On the other hand, the gaps can be defined with higher precision even in submicrometer scale by growing a SiO_2 layer using PECVD. However, the device should be designed with its elements in a vertical scheme in that case.

During a PECVD process, the reactants are brought to the vicinity of a hot sample by gas flow and appropriate chemical reactions take place to grow the material of interest on the sample surface. The normal CVD (chemical vapor deposition) reactions require the samples to be at temperatures as high as 700 to 1000 ^{0}C [61]. PECVD makes use of plasma reactions to assist the CVD reactions taking place which result in the samples being deposited at relatively low temperatures, 100-350 ^{0}C. PECVD processes are conducted in plasma reactors which may be in barrel (or tube) or planar or downstream configurations. We have used a fully automated planar plasma reactor (*Plasmalab 8510C*) for deposition of dielectric layers.

The detailed growing process is as follows: Samples are placed on the lower electrode plate of the previously heated reactor. A 13.56 MHz radio frequency (RF) applied across the electrode plates to excite the plasma. Each of the process gases are brought into the reactor chamber from its specific gas line. The characteristics (refractive index, film thickness etc.) of PECVD grown films depend on the reactor used, gas type and flow rate, RF power, sample temperature and material. In Table 2.2, recipes that we used to grow PECVD Si_3N_4 and SiO_2 films are summarized.

2.2.3 Deposition of Thin Metal Films

We made use of thin metal layers that are either evaporated or sputtered from a target. Nickel (Ni) films was used as both masking material in dry etching and as thin metal heaters. Ni is resistive to most etching gases and a layer of 100 nm can be enough for etching down Si or PECVD dielectrics to more than 5

Process Parameters ⇓	SiO_2	Si_3N_4
2% SiH_4 + 98% N_2 Flow Rate (sccm)	180.0	180.0
NH_3 flow Rate (sccm)	-	45.0
N_2O_3 flow Rate (sccm)	225	-
Pressure (mTorr)	1000.0	1000.0
RF power (W)	10.0	10.0
Temperature (^{0}C)	250.0	250.0
Grow Rate ($\mathring{A}$/mins)	400	100

Table 2.2: Recipes for growing Si_3N_4 and SiO_2 films using PECVD

μm. Before deposition of metals, patterns are defined through photolithography on the samples. Parts on which metal will be deposited should be clear, while the other parts should be PR coated. Metal is deposited over all surface of the sample, PR coated or not. After the deposition, the samples are put into a ACE bath for a while. This is to facilitate the process called liftoff. ACE dissolves PR film and lift the metal parts on PR off.

2.2.4 Etching Processes

Photolithography defines PR patterns onto surface of samples. PR layer should be used as mask layer to transfer patterns into waveguide material or another material that would be used as mask layer. Also patterns can be transferred to metal layers through liftoff process as discussed above. PR layers or metal layers are used as masking material in dry etching. On the other hand, Si_3N_4 is the mask for KOH etch. We transferred PR patterns into Si_3N_4 through a dilute HF etch. Before etching in HF solution, the PR patterns are further hardened via another baking process at 120 for 2 mins at a hotplate. The HF solution that we used was with the ratio 1 : 100 for $HF(50\%) : H_2O$. The etch rate 50 $\mathring{A}$/s. After the etch remaining PR is removed in ACE. The sample with Si_3N_4 patterns are ready for KOH etch.

Patterns must be defined into waveguide materials, to Si layer of SOI wafer in our case. Dry and wet etching techniques can be employed for this purpose. In both techniques, the unmasked parts on SOI samples are etched down for desired

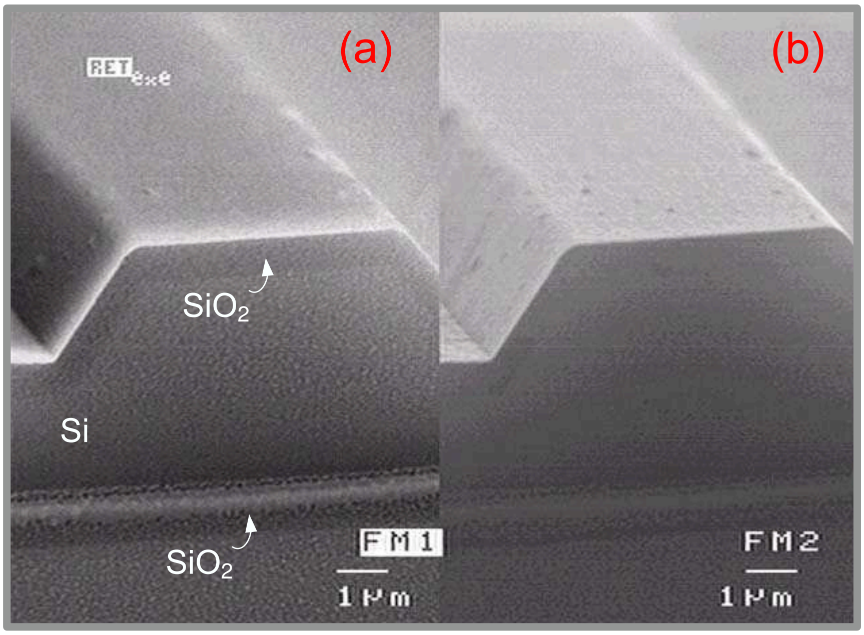

Figure 2.7: SEM micrographs of a SOI rib waveguide defined through KOH etching. (a) In topographic view of the waveguide facet, different materials can be identified. (b) Normal SEM view of the same facet.

thickness. Dry etching uses physically assisted chemical radicals and ions, which are produced in a plasma reactor, to etch the semiconductor material surface, both chemically and mechanically. Dry etching which can be called as reactive ion etching (RIE), results in an anisotropic etching profile. That is, some special planes of semiconductor crystals are preferably etched at a higher rate than other planes. On the other hand, wet etching being the most widely used etching technique makes use of chemical reactions taking place between semiconductor material and aqueous acidic and basic solutions. Unlike dry etching, wet etching is generally isotropic for the most semiconductor material and etching solution pair, but also some examples of anisotropic wet etchants exist. Both dry etching (or RIE) [12, 32, 33, 34] and wet etching [23, 62] have been applied in silicon-on-insulator based waveguide device fabrication.

Straight waveguides and devices that do not have circular or S-shaped parts can be easily etched in anisotropic KOH etch. All the other shapes are better to be defined through RIE. KOH anisotropic etching of silicon have been studied a lot since the early 60's [63, 64]. The etch rates are different for different KOH

Material ⇒	Si (slow)	Si (fast)	Si (faster)	SiO_2	BCB
CHF_3 Flow Rate	50	-	-	150	150
0_2 Flow Rate	3	6	-	10	10
SF_6 Flow Rate	-	28	20	-	-
CCl_2F_2 Flow Rate	-	-	30	-	-
Pressure(mTorr)	66	50	50	50	50
RF Power(W)	100	100	100	100	100
Etch Rate($\mathring{A}$/min)	140	870	1500	170	1090
Reference No.	RIE1	RIE2	RIE3	RIE4	RIE5

Table 2.3: RIE etch recipes used to etch various materials during fabrication processes.

concentrations and etch temperatures. It is also not the same in each crystallographic planes of silicon. This difference makes KOH an anisotropic etchant. We used 1:3:1, KOH:H_2O:ISO solution at 40 ^{0}C as our optimum parameters. These parameters were optimized during my M.S. Thesis work [54]. This recipe have been used for anisotropic etch of SOI waveguides that we used in layer transfer method discussed in Chapter 6. The etch rate for this recipe is not constant with time and this is a general property of anisotropic KOH etching. However, the etch rate remained in the range of 550 to 650 $\mathring{A}$/min. The other parameters that may affect especially the repeatability are the total volume of the solution and the stability of solution temperature. Larger solution volumes and more stable solution temperature result in better etch results. A typical result of KOH etch is given in Fig. 2.7.

We also used KOH etching to thin backside of the SOI samples after the all fabrication steps are over. Such a thinning from 625 μm down to 150 μm is required for a good optical cleavage of waveguide facets. An KOH etch recipe (KOH:H_2O ratio of 1:3 at 60 ^{0}C) having larger etch rate (18 μm/hr) was preferred for thinning. The process details of which can be found in [54] lasts for more than 24 hrs.

RIE was used to define polarization splitters (Chapter 3) and ring resonators (Chapter 5) on SOI wafers in this thesis work. We also facilitated dry etching technique to define ribs on some polymer (BCB) and deep channels on thick

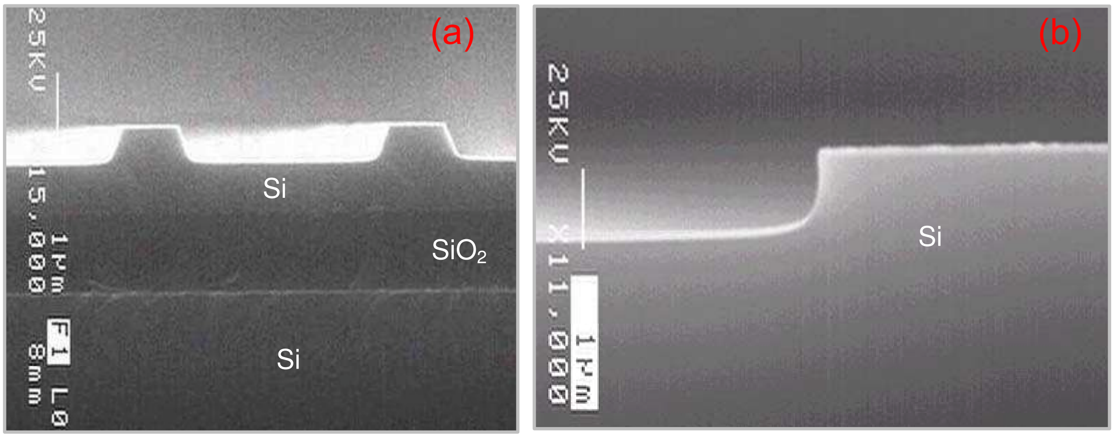

Figure 2.8: SEM micrographs of some structures defined through RIE etching. (a) SOI rib waveguide etched using RIE1 recipe. (b) A silicon step etched using RIE2 recipe.

thermally grown SiO$_2$ layers. In principle, any type of material can be etched down with a good choice of process gas. The critical point is to have a resistive enough masking material. PR itself may be more than enough for shallow etches as we did in fabrication of SOI polarization splitters and resonators. Etch depths defined into top silicon layers were in the order of 0.5 μm. The use of thick PR may help to reach etch depths up to 2 μm in silicon. On the other hand, it is possible to define groves with depths larger than 4 μm using a 100 nm Ni layer as mask. In the etching process of SiO$_2$ layer, we define channels with depths of up to 4 μm with Ni as the masking material. We also used Ni mask to define grooves with 6 μm depth on silicon chips which were then used as molds for analysis of some biomaterials by Prof. Dr. Vasıf Hasırcı's Group at METU. A specific recipe is used when etching is performed in RIE systems. That is, gas flow rates, chamber pressure and applied RF power are the parameters that determine etch rate and anisotropy of a process. We tabulated the different recipes that were used in RIE etching of various materials in Table 2.3 and referred to them later in the coming chapters. Some SEM micrographes show results of some etch recipes in Fig. 2.8.

2.3 Basic Characterization Techniques

Fabricated devices are characterized on an integrated optics experiment setup. In their characterization, devices are tested and results obtained are compared with theoretical or design expectations. Waveguide as the basic component of integrated optics, are characterized for their optical modal and losses properties. The mostly applied tests to integrated optical devices are power splitting, wavelength dependent transmission and power modulation due to an external effect.

An schematic view of our measurement setup can be seen in Fig. 2.9. We have used both an external cavity tunable laser and a DFB (Distributed Feed Back) laser as light sources. The tunable laser has wavelength resolution of ± 1 pm and can be tuned between 1515 nm and 1615 nm, while, the DFB laser lases around 1550 nm. Optical measurements were generally performed with the laser being at 25 ^{0}C and under 27 mA current. The laser has a peak value of 1547.58 nm under these condition. DFB laser was the light source during characterization of polarization splitter and most of the other experiments that did not require wavelength tunability. On the other hand, all the resonator (Chapter 5) and asymmetrical vertical coupler (Chapter 6) tests need wavelength tuning and were tested using the tunable laser.

Fiber-laser integration enables light to be transferred to a single mode (SM) fiber with core size of 9 μm. This SM fiber is attached to another SM fiber which is bent to form a number of circles with diameter of a few cm and placed in three circular mounts called polarization controller and used to chose only one polarizations state. The polarization controller is attached to another SM fiber whose tapered and lensed (or optically cleaved) end is positioned in a fiber-chuck on a piezoelectric XYZ translation stage. Submicron translation of input fiber could be done by driving the stage with an external voltage supply. In butt coupling, light is directly coupled into waveguides through the cleaved fiber end or focused on waveguide facet when lensed fiber is used. Sample holder is also integrated on a XYZ translation stage which improves the fiber-chip coupling. Light coming out of the waveguides end facets is collected and then focused to either a photodetector or an IR camera using a microscope objective. The

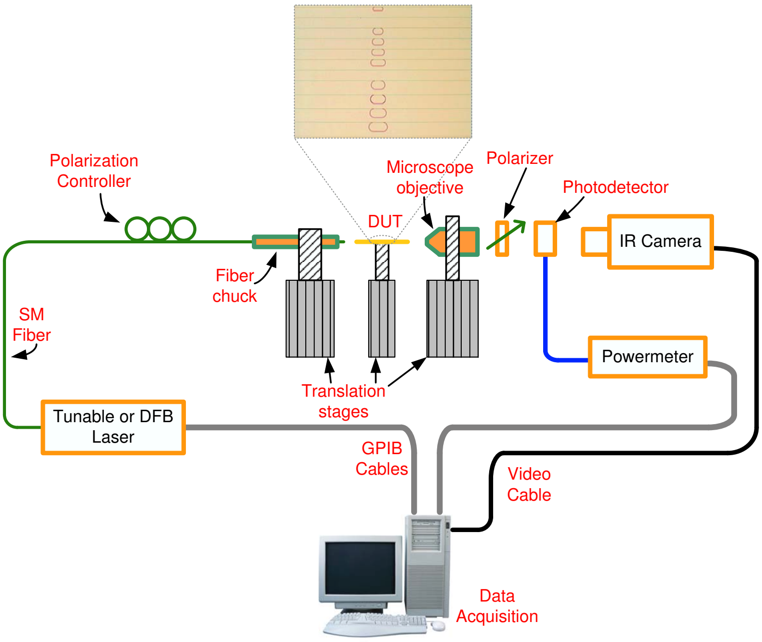

Figure 2.9: Schematic representation of experimental setup used for integrated optical device characterization.

detector can measure output optical signal through the use of an oscilloscope or optical powermeter. Optical power measurements are then used for calculating optical losses. Fine positioning of optical modes were done using the camera prior to any measurement.

A number of neutral density filters were used to control optical power to avoid saturation of the camera when the images captured to image files using an video capture card attached to a PC. Coupling properties of directional couplers were calculated by analyzing captured IR images with an image contrast analysis software. The software we used was labelled Scion Image and had the ability to read relative intensities at each pixel of a straight line cursor placed on an image. Tunable laser and powermeter were remote controlled through use of Labview programming on a PC connected to the instruments by GPIB cables. We were able to scan the laser wavelength in a range and with a resolution of our choice.

2.3.1 Optical Waveguide Losses

Two types of optical losses that can be extracted from characterization of a waveguide are insertion and propagation losses. First one include both losses occurring during light propagation in the waveguide and those due to reflection at input and output waveguide facets. The main contribution to propagation loss comes from scattering of propagating light. Absorption of waveguide material and radiation due to unguided modes are significant and are explained later in this section. Scattering losses can result from imperfections in waveguide material or on the surface of the waveguide. The material imperfections are voids, crystalline defects and contaminant atoms and can be ignored for SOI optical waveguides due to extremely pure nature of silicon crystal. On the other hand scattering from waveguide walls can be an important source of loss and depends on waveguide fabrication techniques. Since, light reflects many times from surfaces of a waveguide, it has been showed quantitatively that the surface scattering loss depends on ratio of the roughness of the waveguide surfaces to the wavelength directly, and the waveguide thickness and the amount of the tail of the evanescent field. In the case of the SOI rib waveguides the roughness of the buried SiO_2 layer, the thickness variation of the top silicon layer and the roughness of the walls of the etched rib are the points to be considered. The first two are related with the fabrication of the SOI substrate and they are results of the optimized commercial technologies. The last is related with the etching of silicon during fabrication process.

Absorption is a mechanism which is mostly important for semiconductor waveguides. Band edge absorption and free carrier absorption are the two types of absorption loss mechanisms that are dominant in semiconductor. We can safely ignore losses due to band edge absorbtion since telecommunication wavelengths (1.3 and 1.55 μm) are well apart from the band gap of the silicon (1.1 eV or 0.9 μm). We also eliminate free carrier absorption, fabricating devices on wafers with low doping levels or high resistivity. Meanwhile, the radiation loss is the name for the loss taking place when a waveguide design is near or beyond cutoff. Well confined single mode waveguides do not suffer significantly from radiation. However, it should be considered for multimode and bending waveguides. In case of SOI rib waveguides, radiation losses are not so significant as long as the waveguide is designed as a single mode waveguide away from the cutoff.

The simplest way of loss measurement for SM waveguides is to input some light with known optical power the waveguide and measure the optical power at the output. While, prism-coupling loss measurement technique is generally preferred for multimode waveguides [65]. What is measured for SM waveguides is the insertion loss. Successive measurement of insertion loss for waveguides of different lengths can be used to extract propagation loss of the waveguide. Observation of Fabry-Parot resonances can also be used to determine propagation loss [53]

The details of insertion loss measurement and extraction of propagation loss are as follows. The light with a known wavelength and optical power is focused or butt-coupled into cleaved or polished input facet of a waveguide using a from cleaved or lensed SM fiber and the transmitted power is measured at the output port. The insertion loss is calculated in dB's using $10\log(I_{in}/I_{out})$, where I_{in} and I_{out} are the optical powers injected at the input and measured at the output, respectively. This measurement is repeated for a large number of waveguides having different lengths, but otherwise identical. This task is accomplished by starting measurements with a relatively long (e.g. several millimeters) waveguide sample then repetitively shortening the sample by cleaving. Measurements are repeated for the waveguides of different lengths. The most important problem of this technique is with alignment which should be optimized for each waveguide/microscope objective pair by maximizing output optical power. Then the logarithm of relative transmission is plotted with respect to waveguide length. The plot is a straight line and its slope gives loss coefficient. This technique is effective for the single mode waveguides which can be easily cleaved to optical quality. I used this technique for loss measurement of 3 μm size during my Ms. Thesis work [54] and found propagation losses of 0.70 and 0.76 dB/cm for TE and TM polarizations, respectively.

A waveguide with optically cleaved facets can be considered as a Fabry-Perot

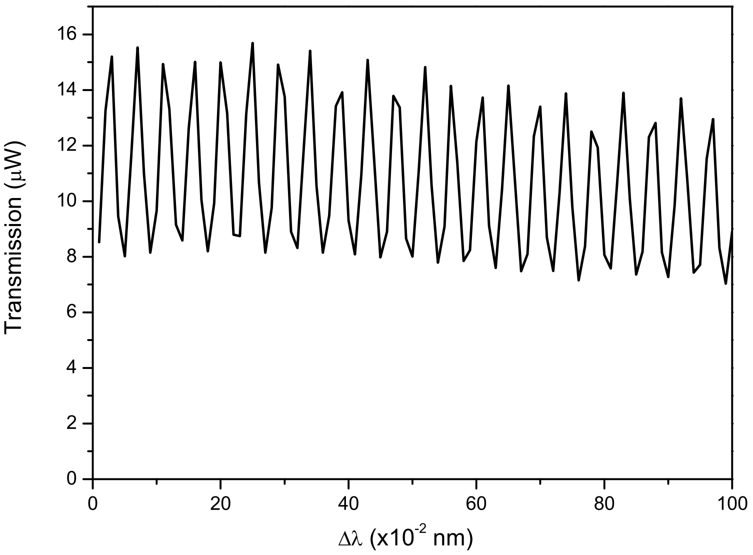

Figure 2.10: Measured transmission spectrum of SM SOI waveguide. Fabry-Perot oscillations are used to calculate propagation loss of the waveguide.

interferometer. The facets behave as the partially transmitted mirrors of the interferometer. An interference pattern forms with a change in the phase of the propagating light. The phase change can easily be accomplished by tuning the input wavelength. The measured optical power has maxima and minima with scanned wavelength. The ratio of the maximum transmitted optical intensity to minimum intensity can be defined as

$$\frac{I_{max}}{I_{min}} = \frac{(1 + Re^{-\alpha L})^2}{(1 - Re^{-\alpha L})^2} \tag{2.11}$$

in terms of reflectance of facets, R, optical power loss coefficient, α and cavity length, L which is the length of the waveguide. Defining this ratio as κ, the loss coefficient can be stated as

$$\alpha = \frac{1}{L} ln[R\frac{\sqrt{\kappa}+1}{\sqrt{\kappa}-1}] \tag{2.12}$$

The optical loss for a waveguide can be determined from Eq. 2.12 with the knowledge of facet reflectance. In practice the same optical quality can not be repeated in each cleavage of a waveguide sample so the reflectance of the facets can not be known exactly. In that case, the cut-back technique can be applied. That is, measuring maximum and minimum intensity for waveguide samples with the same features except different lengths. Then, $10log[(1+\sqrt{\kappa})/(1-\sqrt{\kappa})]$ which has dimension of dB, versus waveguide length is plotted. A straight line should be fitted to that plot. The slope of the line gives optical loss coefficient and extrapolated value to L=0 is the exact reflectivity of facets. We observed Fabry-Perot oscillations for straight SOI rib waveguides of 1 μm size and found an upper limit of 5.5 dB/cm for propagation loss. We used perfect reflectivity for Si facets (Fig.2.10).

Chapter 3

Compact SOI Polarization Splitters

In this chapter, design, fabrication and characterization of SOI directional couplers utilized as a passive polarization mode splitter are explained in details. SOI integrated optical directional couplers have already been fabricated [66]. However, they have not been exploited for polarization splitting applications. We make use of birefringence accumulation in SOI rib waveguides as their sizes are reduced. To the best of our knowledge, this device is the first integrated optical polarization splitter based on SOI technology to separate light into TE and TM modes.

In the next section, we explain the design and operation principles of the device. Fabrication procedures and measurement techniques follow. Finally, the experimental results and some analysis are given.

3.1 Splitter Design

The polarization dependent behavior of integrated optical waveguides has two main sources. One source is the intrinsic material birefringence which can be due

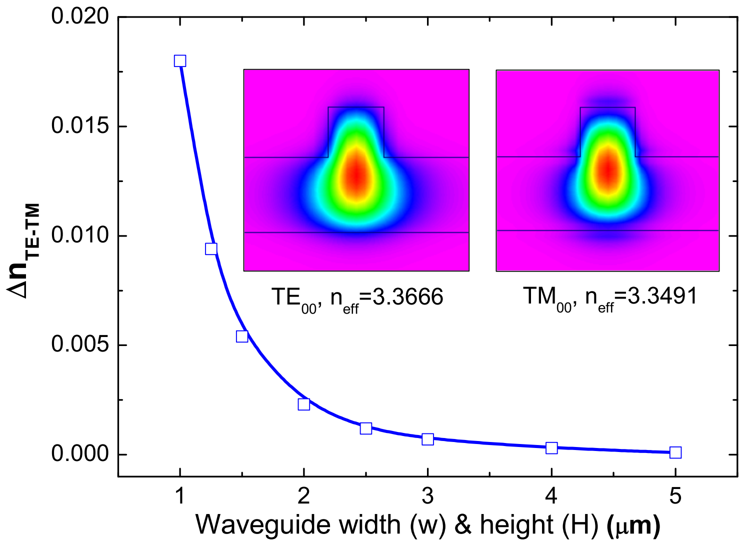

Figure 3.1: Effective index difference between TE and TM modes of single mode (SM) SOI waveguides with $h/H = 0.6$. The insets show simulated fundamental TE and TM mode profiles and effective refractive indices for the designed waveguide.

to stress in the waveguides. The other source is due to waveguide geometry or cross sectional profile. SOI single mode (SM) waveguides with large cross-section are generally known for their polarization insensitivity due to inherent index isotropy of the silicon crystal and negligible stress formed by wafer bonding. The birefringence observed in these waveguides is negligible and has been attributed to cross sectional geometry of the waveguides [12]. It has been shown by numerical simulation that even the small birefringence in the rib waveguides can be tailored to zero by adjusting the geometrical cross section [67]. However, as cross sectional dimensions reduce, birefringence can increase and such waveguides can be designed for a specific birefringence value. Analysis of SOI waveguides by 3D vector beam propagation (BPM) simulations confirm the evolution of geometrical birefringence in SM SOI waveguides as their size is reduced as seen in Fig. 3.1. The waveguides with sizes $w, H \leq 1$ μm display significantly different effective indices for their TE (transverse electric) and TM (transverse magnetic) modes. In our design, width (w) and height (H) of the SM waveguide is chosen to be 1 μm, while slab height (h) is 0.6 μm. These dimensions satisfy the single mode

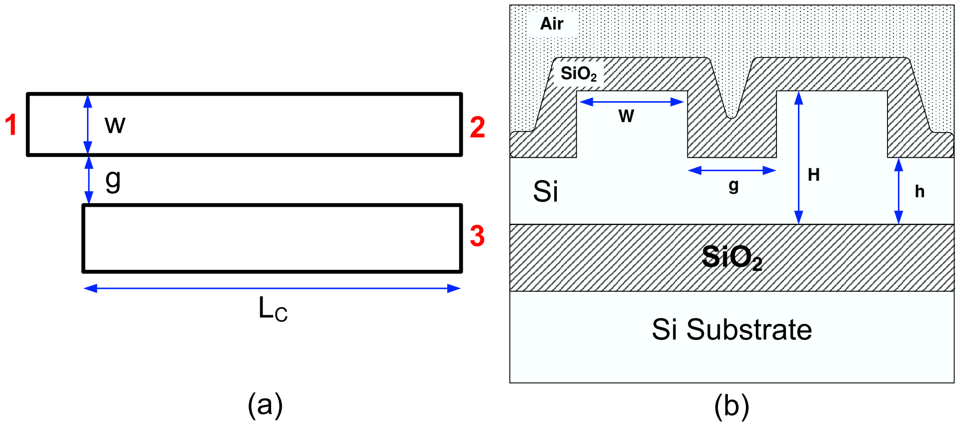

Figure 3.2: A schematic cross sectional view of coupling region of the designed directional coupler with critical dimensions.

condition for an SOI waveguide [56] and can be fabricated with good accuracy. The inset in Fig. 3.1 shows TE and TM mode profiles for the chosen waveguide structure.

In the light of this discussion, we design a directional coupler to be used as a polarization splitter using SOI SM waveguides with top silicon layer thickness of 1.0 μm. For the preliminary design of the polarization splitter we first consider the device layout shown in the Fig. 3.2(a) with its cross-sectional view given in Fig. 3.2(b) . This is a straight directional coupler which can be analyzed with minimal computational effort. Light is launched into port 1 and the output power is detected either from port 2 or port 3. Optical propagation in a directional coupler can be expressed in terms of even and odd modes of the coupled waveguide system with effective indices n_e and n_o. A directional coupler comprising two single mode waveguide is said to have an odd and an even mode. The optical field in the directional coupler at any instance can be expressed as a superpositions of those modes [2]. The evolution of the effective index of these modes for TE and TM polarizations are simulated and shown in Fig. 3.3 as a function of the waveguide spacing. From the figure, it is clear that for small waveguide spacings, the difference between propagation constants of the odd and even modes is large, while they converge to the TE and TM effective indices of individual waveguides as the spacing increases.

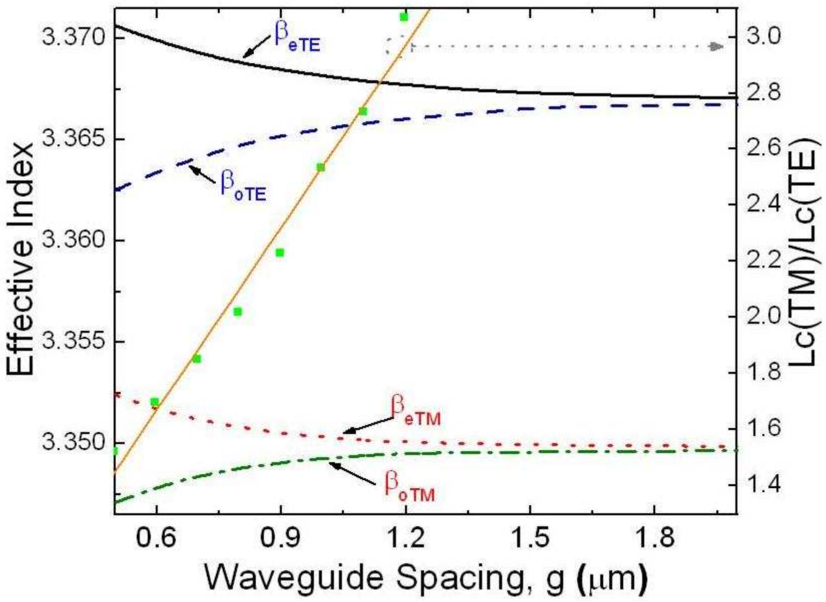

Figure 3.3: TE and TM effective indices of even and odd modes of a coupler as a function of waveguide spacing, g. Note that as g increases odd and even propagation constants converge to respective refractive indices of the isolated waveguides. The ratio of TM to TE coupling lengths are also shown.

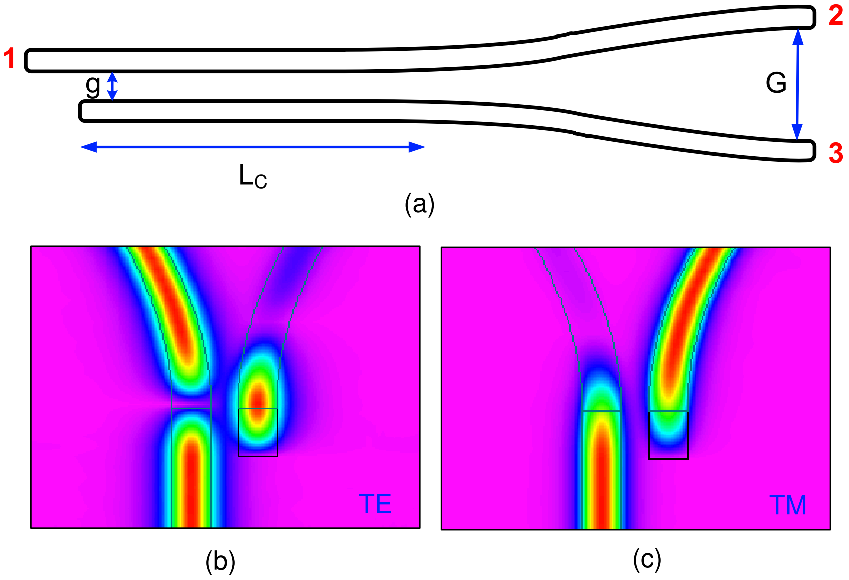

Figure 3.4: The schematic layout of the polarization splitter,(a) with 3D vector BPM simulation results of a coupler with g=0.7 μm and L_c=110 μm for TE (b) and TM (c) modes. The simulations show the excellent polarization splitting. G is 50 μm and the length of the S-bend is 3 mm.

The coupling length, L_c is the length necessary for complete energy transfer and is different for TE and TM polarizations. The coupling length of either TE or TM polarization is given by

$$L_c = (\pi)/(n_e - n_o)k_0 \tag{3.1}$$

in terms of free space wavevector, k_0. We seek a design where,

$$L_c(TM)/L_c(TE) = 2m \tag{3.2}$$

relation is met. Here, m is an integer. The coupling length for TM polarization becomes twice of that of TE polarization at a gap value of 0.8 μm allowing for TE mode injected at the input port to couple back and forth and detected at the output port 2, while the TM mode couples only once and is detected at the output port 3. Using these values as a starting point we considered the design of the polarization splitter shown in Fig. 4(a). In this case output waveguides are separated at the output using S-bends. In order to take into account the coupling contribution at the S-bend waveguides, full 3D vector BPM is used to obtain the final design by scanning various waveguide spacings, g, from 0 to 1.5 μm. Results of 3D vector BPM analysis show that gaps of 0.7 μm and 1.4 μm allows polarization splitting with m values of 1 and 2, and $L_c(TM)$ lengths of 110 μm and 2450 μm respectively (Fig. 3.4(b)). The small difference between waveguide spacing obtained from Eq. 3.2 (0.8 μm) and that obtained from BPM analysis (0.7 μm) is due to the coupling contribution at the S bends. The corresponding devices are the shortest possible polarization splitters with the chosen geometry.

3.2 Fabrication and Results

The SOI polarization splitters are fabricated so that the waveguide widths and heights are 1 μm. Such small dimensions require very uniform silicon layer thickness. Standard bond and etch back SOI (BESOI) wafers show thickness variations of 500 nm which is not suitable for our purpose. However, Unibond wafers have thickness uniformities ranging from ±20 nm down to ±5 nm [26]. These wafers

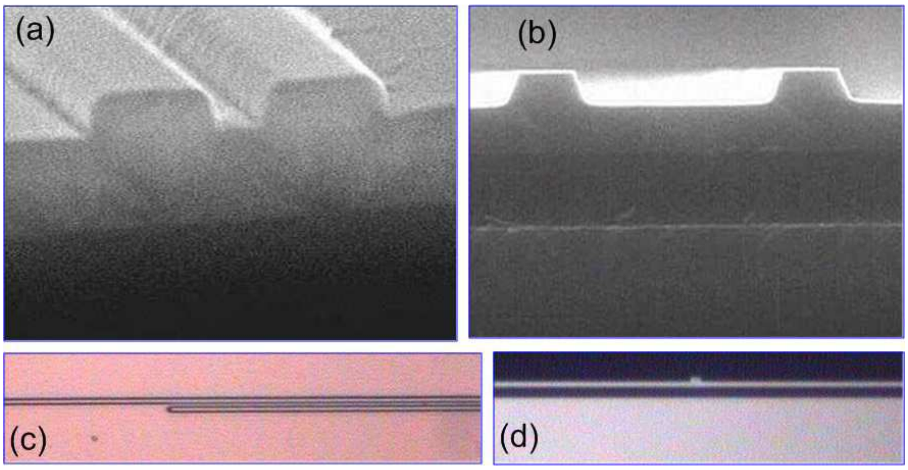

Figure 3.5: Cross-sectional SEM micrographs of (a)coupling region and (b)output ports. Optical images show (c)top view of coupling region and (d)cross-sectional view of input port.

are fabricated by H^+ ion implantation followed by heat treatment, while BESOI wafers are bonded and polished down to the desired thickness.

We start the fabrication with a Unibond wafer with silicon layer thickness of 1000 ± 20 nm and cleave a piece that has dimensions of 1.5 cm x 1.5 cm. A photoresist layer is spun and the device is optically exposed by lithography (PL1). The pattern is transferred to the SOI chip by reactive ion etching (RIE) using a slow etch recipe (RIE1). The RIE etch is followed by the deposition of a thin upper cladding layer of SiO_2 using plasma enhanced chemical vapor deposition (PECVD). In order to obtain optical quality facets for optical measurements, we cleave the chip at the input and output ports. We find that best cleaves are obtained when we thin the 625 μm thick substrate down to approximately 100 μm as explained in previous chapter. The optical and SEM micrographs of the fabricated directional couplers are shown in Fig. 3.5.

The fabricated and optically cleaved devices are tested on the integrated optics setup with a distributed feedback laser (DFB) laser operating at 1550 nm. The input light polarization state is controlled by a fibre polarization controller. In order to improve light coupling to the waveguides, a tapered and lensed fibre

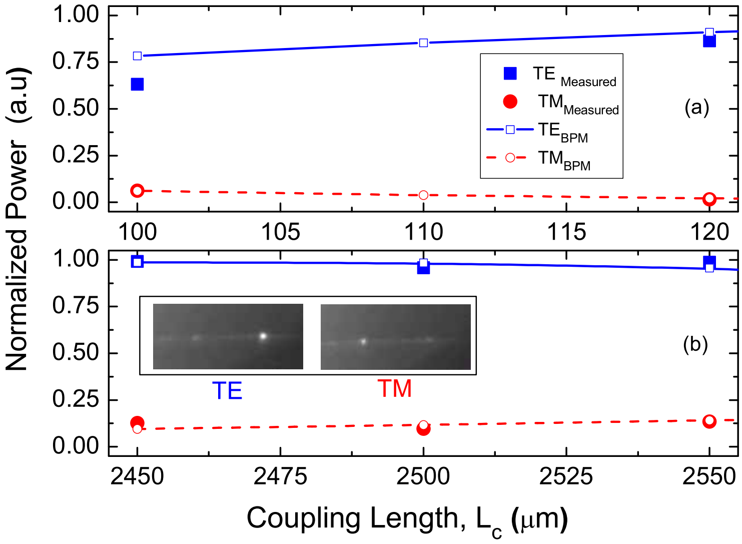

Figure 3.6: Normalized polarized optical power measured at the output port 2 for both TE and TM input signals for (a) gap=0.7 μm and (b) gap=1.4 μm. Lines are drawn to guide the eye.

with beam spot diameter of 2 μm was used. TE and TM measurements are made separately. Before each measurement, the laser light optimized in either polarization state is focused on the input facet of the directional coupler. A polarizer with high extinction ratio is used after the device to confirm the polarization state of the measured signal. The input waveguide connected to port 1 was at least 3.5 mm from the point where the coupler starts to eliminate the possibility of exciting both waveguides of the coupler while exciting port 1. Light at the output ports are viewed by an IR camera and captured by a TV-video card. The results for gaps of 0.7 and 1.4 μm are given in Fig. 5. We observe very good polarization splitting at the designed coupling length of 2450 μm for 1.4 μm gap (extinction ratios of 20.8 dB for TE and 9.7 dB for TM polarizations) and at the designed coupling length of 120 μm for 0.7 μm gap (extinction ratios of 18.1 dB for TM and 8.0 dB for TE polarizations). Extinction ratios (ER) quoted are defined in units of dB as

$$ER_{TE} = 10log(\frac{P2}{P3}) \tag{3.3}$$

for TE polarization and

$$ER_{TM} = 10log(\frac{P3}{P2}) \tag{3.4}$$

for TM polarization in terms of $P2$ and $P3$, optical powers measured at ports 2 and 3, respectively.

The results obtained from 3D vector BPM simulations and the results obtained from the experiments are in very good agreement when the coupling contribution from the S-bends is taken into account. The relatively large insertion losses due to small cross sectional areas of these devices can be alleviated by using mode transformers. Propagation losses of 5.5 dB/cm measured on straight waveguides with same dimensions are in good agreement with the literature [51] and are due to sidewall roughness and can be further reduced by controlled oxidation of the waveguide surfaces [51]. These results prove that geometrical birefringence based polarization control is possible in the thin core layers of SOI wafers. Even smaller devices can be made using smaller gaps and smaller waveguide dimensions using submicron core layers.

In conclusion, a SOI rib waveguide becomes birefringent as its size reduced. We used this idea to design and fabricate a directional coupler polarization splitter based on geometrical birefringence. The device uses 1 μm sized silicon-on-insulator waveguides. The length of the device is about 2500 μm for gap of 1.4 μm but is drastically shortened to about 120 μm for gap of 0.7 μm. We, thus have demonstrated the first polarization splitter that uses geometrical birefringence control of high-index optical waveguides on silicon-on-insulator platform [68].

Chapter 4

Ring/Racetrack Resonators: Analysis and Design

This chapter gives analysis of ring/racetrack resonators and design of such resonators based on SOI rib waveguides. I explain basic waveguide resonator theory in the first section then give design details in the second section. The chapter concludes with a section analyzing possible integrated micro-ring resonators on micromachined cantilevers to be used as a displacement sensor.

4.1 Analysis of Waveguide Ring/Racetracks Resonators

A ring resonator system is composed of one or two straight waveguides called bus waveguides and a ring placed very close to them as shown in Fig. 4.1. There are several figures of merit for a ring resonator. These are the modulation depth which shows the depth of the on/off ratio (in dB), free spectral range (FSR) which is the wavelength spacing between adjacent resonances, full width at half maximum (FWHM) of each resonance which shows how narrow the peak is at the resonance wavelength. The Q factor gives the ratio of resonance wavelength

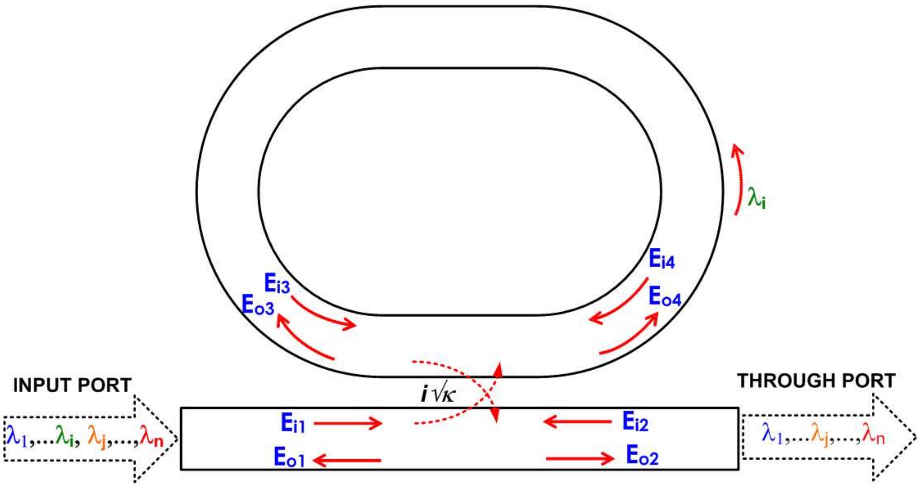

Figure 4.1: Schematic representation of a single bus racetrack resonator and the relevant propagating field amplitudes.

to FWHM of the resonance. Depending on the application, large or small values for FSR may be desirable but small FWHMs, large modulation depths and large Q factors are always preferred.

4.1.1 Single Bus System

Consider the single bus coupled ring structure in Fig.4.1. The general matrix for outgoing waves (E_o) in terms of incoming waves (E_i) in the coupling region of the system can be written as [69]

$$\begin{pmatrix} E_{o1} \\ E_{o2} \\ E_{o3} \\ E_{o4} \end{pmatrix} = \begin{pmatrix} 0 & \sqrt{1-\kappa} & 0 & i\sqrt{\kappa} \\ \sqrt{1-\kappa} & 0 & i\sqrt{\kappa} & 0 \\ 0 & i\sqrt{\kappa} & 0 & \sqrt{1-\kappa} \\ i\sqrt{\kappa} & 0 & \sqrt{1-\kappa} & 0 \end{pmatrix} \begin{pmatrix} E_{i1} \\ E_{i2} \\ E_{i3} \\ E_{i4} \end{pmatrix} \tag{4.1}$$

Here, κ is the fraction of power coupled between waveguide and ring, so that $1-\kappa$ is the transmitted portion of the power that is not coupled to the ring. In the case of no back reflections and E_{i1} being the input wave,

$$E_{i2} = E_{i4} = E_{o1} = E_{o3} = 0 \tag{4.2}$$

Then, solving the matrix for the remaining terms leads to transmitted amplitudes as

$$E_{o2} = \sqrt{1-\kappa}\ E_{i1} + i\sqrt{\kappa}E_{i3} \tag{4.3}$$

and

$$E_{i4} = \sqrt{1-\kappa}\ E_{i3} + i\sqrt{\kappa}E_{i1} \tag{4.4}$$

Matching the travelling waves in the ring gives,

$$E_{i3} = E_{o4}\exp\left(-\left(\frac{\alpha_T}{2} + i\phi\right)\right) \tag{4.5}$$

and using it to eliminate E_{i3} in the above equations results in

$$E_{o2} = \frac{\sqrt{1-\kappa}\ - \exp\left(-\left(\frac{\alpha_T}{2} + i\phi\right)\right)}{1 - \sqrt{1-\kappa}\ \exp\left(-\left(\frac{\alpha_T}{2} + i\phi\right)\right)}E_{i1} \tag{4.6}$$

where, α_T and ϕ are optical intensity loss and phase accumulated per round trip in the ring, respectively. For a resonator of length, $L = 2\pi R$ optical intensity loss coefficient, α and effective refractive index of n_e,

$$\alpha_T = \alpha L \tag{4.7}$$

and

$$\phi(\lambda) = \frac{2\pi}{\lambda}n_e L \tag{4.8}$$

where λ is the free space wavelength. The resonance takes place when $\phi = 2\pi m$, and m is an integer number. Then, the resonance field amplitudes become

$$E_{o2} = \frac{\sqrt{1-\kappa}\ - \exp\left(-\frac{\alpha_T}{2}\right)}{1 - \sqrt{1-\kappa}\exp\left(-\frac{\alpha_T}{2}\right)}E_{i1} \tag{4.9}$$

and

$$E_{o4} = \frac{i\sqrt{\kappa}}{1 - \sqrt{1-\kappa}\exp\left(-\frac{\alpha_T}{2}\right)}\ E_{i1} \tag{4.10}$$

An obvious result is that if

$$\sqrt{1-\kappa} = \exp\left(-\frac{\alpha_T}{2}\right) \tag{4.11}$$

no power is reflected so that $E_{o2} = 0$. This is the so-called critical coupling condition and all the power is coupled to the ring.

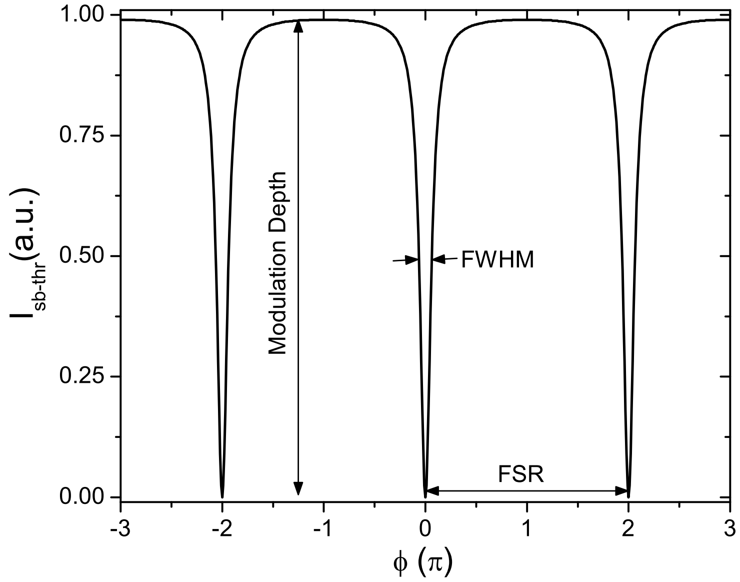

Figure 4.2: Phase dependence of transmitted power at the throughput port of a single bus ring resonator system.

One has to take square of the field E_{o2} and E_{o4} to find the corresponding optical intensities in terms of the input optical power. Therefore, the transmitted power at the through port of single bus system is

$$I_{sb-thr} = |E_{o2}|^2 = |\frac{\sqrt{1-\kappa}\ -\exp\left(-(\frac{\alpha_T}{2}+i\phi)\right)}{1-\sqrt{1-\kappa}\ \exp\left(-(\frac{\alpha_T}{2}+i\phi)\right)}\ E_{i1}|^2 \qquad (4.12)$$

The phase dependence of I_{sb-thr} can be seen in Fig.4.2. FSR, FWHM and modulation depth for this specific example are also shown in the figure.

4.1.2 Double Bus System

The above treatment can be easily extended to a ring structure coupled to two bus ring structure as shown in Fig.4.3. When there is a second bus, there will be a second coupling region allowing for the out coupling of trapped light in the ring. The expression for transmitted power at through port is exactly the same

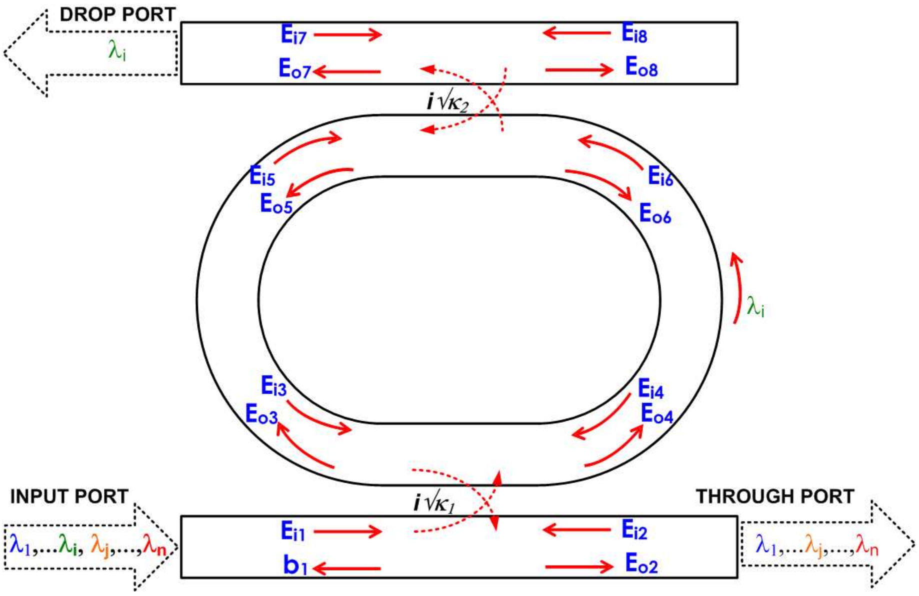

Figure 4.3: Schematic representation of a double bus racetrack resonator and the relevant propagating field amplitudes.

as in the single bus system apart from a change in the loss term to account for the coupled power to the second bus. The new loss term becomes

$$\alpha_{eff} = -\ln{(1-\kappa_2)}^{1/2} \ + \frac{\alpha_T}{2} \tag{4.13}$$

Therefore, the transmitted intensity at the throughput port of double bus system is given by

$$I_{db-thr} = |\frac{\sqrt{1-\kappa} - \exp{(-(\alpha_{eff}+i\phi))}}{1-\sqrt{1-\kappa}\ \exp{(-(\alpha_{eff}+i\phi))}}\ E_{i1}|^2 \tag{4.14}$$

which can be simplified to

$$I_{db-thr} = |\frac{\sqrt{1-\kappa_1}\ \ -\sqrt{1-\kappa_2}\exp{(-(\alpha_T/2+i\phi))}}{1-\sqrt{(1-\kappa_1)(1-\kappa_2}\ \exp{(-(\alpha_T/2+i\phi))}}\ E_{i1}|^2 \tag{4.15}$$

To calculate the power at the drop port, the field, E_{o8} in the output port can be defined in terms of E_{o4} as

$$E_{o8} = i\sqrt{\kappa_2}\ E_{o4}\exp{(-\frac{1}{2}(\frac{\alpha_T}{2}+i\phi))} \tag{4.16}$$

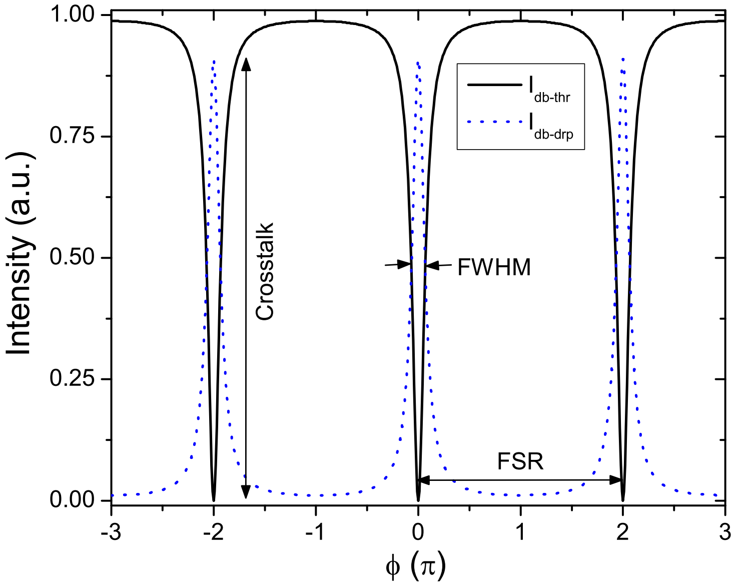

Figure 4.4: Phase dependence of transmitted power at the throughput port of single bus system.

By taking square E_{o8}, the optical power at drop port can be calculated to be

$$I_{db-drp} = \left| \frac{\sqrt{\kappa_1 \kappa_2} \exp\left(-\left(\frac{\alpha_T}{2} + i\phi\right)\right)}{1 - \sqrt{(1-\kappa_1)(1-\kappa_2)} \ \exp\left(-\left(\frac{\alpha_T}{2} + i\phi\right)\right)} E_{i1} \right|^2 \tag{4.17}$$

The phase dependence of I_{db-thr} and I_{db-drp} can be seen in Fig.4.4 FSR, FWHM and crosstalk (an other important characteristic of double bus system and defined as the difference between measured intensities at throughput and drop ports at a resonance) are also shown in the figure.

In above equations, κ_1 and κ_2 is the fraction of power coupled between the resonator and the first and the second buses, respectively. In most cases $\kappa_1 = \kappa_2 = \kappa$. However, analyzing the resonances and imposing that there is no reflected power , i.e. $I_{db-thr} = 0$, gives the critical coupling condition for the double bus system as,

$$\sqrt{1-\kappa_1} = \sqrt{1-\kappa_2} \ \exp\left(-\frac{\alpha_T}{2}\right) \tag{4.18}$$

or

$$\kappa_2 = 1 - (1 - \kappa_1)\exp(\alpha_T) \tag{4.19}$$

This condition defines an asymmetrically coupled resonator. κ_1 should be large enough to account for both resonator attenuation and coupling to the second bus. It should be noted that the through port power is minimized and crosstalk is maximized when this condition is satisfied.

4.1.3 Characteristics of Resonators

The basic characteristics of resonators are bandwidth (FWHM), free spectral range (FSR), finesse, Q-factor and modulation depth can be extracted from their responses. On the other hand, an analytical estimation can also be made for these characteristics. An relation can be derived for FWHM from its definition, the full width at half maximum (I_{sb-drp}=1/2 I_{inp}). Such a relation is ([70])

$$FWHM = \Delta\lambda = \frac{\lambda_0^2}{\pi L n_{eff}} \frac{(1 - \exp(-\frac{\alpha_T}{2})\sqrt{(1-\kappa)})}{\sqrt{\exp(-\frac{\alpha_T}{2})(1-\kappa)}} \tag{4.20}$$

This relation reduces to

$$FWHM = \Delta\lambda = \frac{\lambda_0^2 \kappa}{\pi L n_{eff}} \tag{4.21}$$

when optical loss is negligible [71]. This relation suggests that smaller coupling factors leads to narrower bandwidths. Furthermore, the accumulated phase of one particular resonance (λ_0) is 2πm and that of the successive resonance (λ_0+FSR) is 2π(m+1). The definition of accumulated phase can be used to calculate FSR as

$$FSR = \frac{\lambda_0^2}{L n_{eff} - \lambda_0} \tag{4.22}$$

which can be approximated as

$$FSR = \frac{\lambda_0^2}{L n_{eff}} \tag{4.23}$$

for large resonator circumferences. We can conclude from the above equation that smaller resonators have larger FSR's. From known FWHM and FSR one can easily calculate finesse and Q-factor as

$$Finesse = \frac{FSR}{FWHM} \tag{4.24}$$

and

$$Q = \frac{\lambda_0}{FWHM} \tag{4.25}$$

,respectively. Physical meanings of finesse and Q-factor can be understood as follows. The finesse equals to (to a factor of 2π) the number of round trips made by light before the power in the resonator reduces to 1/e of the initial value. Similarly, Q-factor is the number of field oscillations before field decreases to 1/e of its initial value. Finally, the expected modulation depth (M.D.) of a resonator can be calculated in the units of dB using resonance optical intensity at through port as

$$M.D. = 10\log(\frac{I_{sb-thr}(\lambda = \lambda_0)}{I_{inp}}) \tag{4.26}$$

Apart from mentioned resonator characteristics, intensity enhancement in a resonator can be found interesting. Constructive interference occurred in a resonator leads intensity to build up in the resonator. This feature of resonator is found very helpful in nonlinear optics experiments in which high optical intensities are required. For resonators with a single bus (all-pass configuration) the intensity enhancement (I.E.) factor is given by ([71])

$$I.E. = \frac{1 + \sqrt{1-\kappa}}{1 - \sqrt{1-\kappa}} \tag{4.27}$$

when resonator loss is negligible. The less coupling to a resonator leads more intensity building up in the resonator.

4.2 Design of SOI Racetrack Resonators

The design of SOI resonators starts by determining the largest waveguide dimensions that satisfy single mode condition. After a preliminary estimation using effective index methods, exact dimensions of the waveguides have been determined after extensive numerical simulations using the three dimensional beam propagation method (BPM). The waveguide has the same dimension of the waveguide

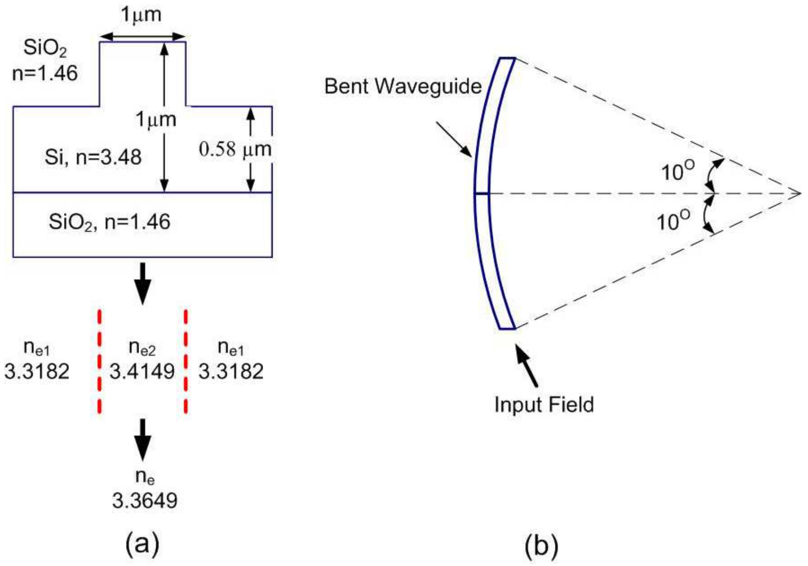

Figure 4.5: (a) 3D to 2D reduction using effective index method for analytical bending loss calculation for TE polarization. (b) 20° section of a bend defined for numerical bending loss calculation using BPM.

used in polarization splitter design (Fig. 3.2). This is followed by the estimation of the expected propagation losses which is critical in the design of high-Q waveguide resonators. Measurements on straight waveguides designed and fabricated with dimensions obtained in the simulation step, were performed to determine the upper limit on the expected propagation losses. In most Si rib waveguide devices, quasi single mode waveguides with large cross sections are preferred to minimize insertion losses. Design of ring resonators using SOI rib waveguides with typical widths and heights of 3 μm or larger, however, leads to rings with radii larger than 10 mm due to radiation losses at smaller radii. This would lead to poor free spectral range. To obtain compact devices suitable for higher integration that have larger free spectral range, ring resonators with curvatures of submillimeter radii, are needed. Thus, smaller waveguide dimensions are essential for compact ring resonators.

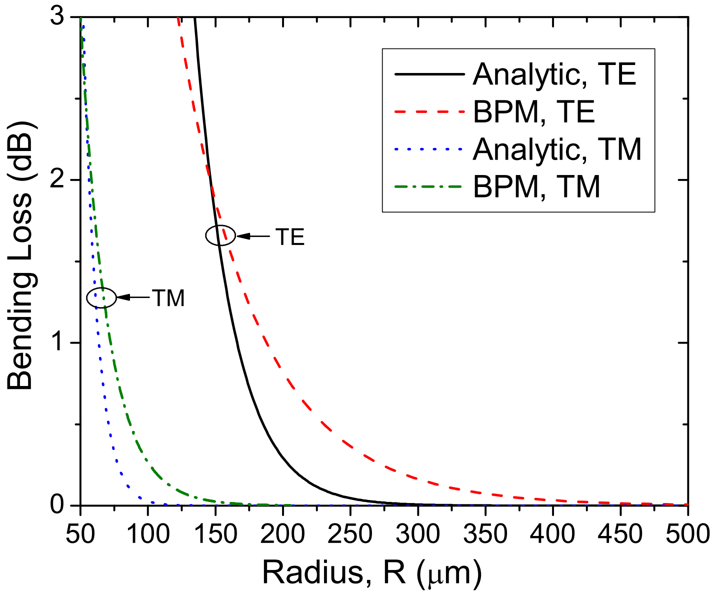

Figure 4.6: Simulated and analytically calculated bending losses for 1 μm SOI waveguide.

4.2.1 Bending Loss Calculation

A major issue in the design of ring resonators is the estimation of bending loss. We first calculated the bending loss using a two dimensional analysis based on Marcuse's equation for bending slab waveguides. The details of the analysis can be found in [72]. Briefly, in this approach, the 3-D waveguide structure is reduced to 2-D (See Fig.4.5 (a)) using the effective index method, and the resulting analysis leads to bending loss in dB's for a given angular section $\Delta\theta$ (in radians) of radius R as

$$Loss_{bend} = -10\log\left(\exp\left(-\alpha_{bend}\Delta\theta R\right)\right) \tag{4.28}$$

where α_{bend} is the optical bending loss coefficient and is given by

$$\alpha_{bend} = \frac{\alpha_y^2}{k_0^3 n_e(1+\alpha_y\frac{w}{2})}\frac{k_y^2}{(n_{e2}^2-n_{e1}^2)}\exp\left(\alpha_y w\right)\exp\left(\frac{-2\alpha_y^3}{3n_e^2k_0^2}R\right) \tag{4.29}$$

The other variables are defined as

$$\alpha_y = k_0(n_e^2-n_{e1}^2)^{1/2} \tag{4.30}$$

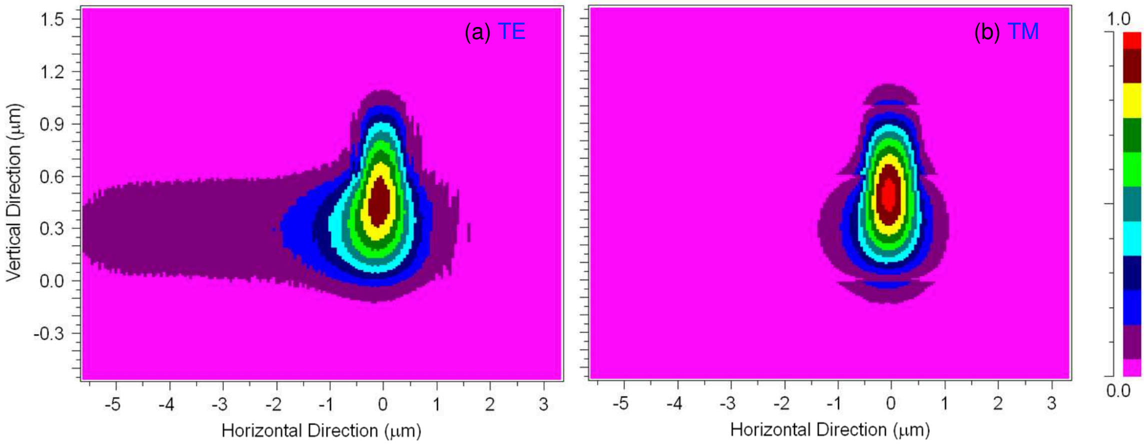

Figure 4.7: SOI waveguide mode fields for TE (a) and TM (b) polarizations after a propagation of 20° in a bend waveguide of 150 μm radius.

and

$$k_y = k_0(n_{e2}^2 - n_e^2)^{1/2} \tag{4.31}$$

with $k_0 = 2\pi/\lambda_0$.

Alternatively, we also made use of 3D-BPM under wide angle approximation conditions to simulate the bending loss by defining a 20° section of a bend shown in Fig.4.5 (b) and calculating the bending loss by launching the computed mode field of the straight waveguide into the curved section as explained in [72]. We approximate the total bending loss for 90° by scaling the loss simulated for 20°. Both analytically calculated (Eq.4.28) and BPM simulated bending losses are shown in Fig.4.6 for TE and TM polarizations. The results of both analysis show that the bending losses drastically decrease for radii larger than 250 μm and 120 μm for TE and TM polarizations respectively. For a better visualization of light propagating in an SOI bend waveguide, we show BPM calculated TE and TM mode profiles after a propagation in a 20° bend of 150 μm radius in Fig. 4.7. It is seen that after a 20° propagation a significant amount of TE mode field is outside the rib of the waveguide. On the other hand, TM mode still propagating under the rib. These results brings a more comprehensive explanation to the very different bending losses for TE and TM polarizations.

4.2.2 Coupling Factor Calculation

Following the determination of the range of radii that can be used in the design of ring resonators, the coupled power factor from the bus waveguide to an adjacent waveguide bend has to be calculated. 3D BPM simulations are also employed for this purpose. A straight waveguide is placed close to a bent waveguide similar to the one used to simulate the bending losses. The optical power launched into the straight waveguide is monitored at the output of the bent waveguide (inset of Fig.4.9). The minimum coupling gap is determined by the limits of optical photolithography which, in our case, is 0.7 μm. This value limits the gap coupling factor between the bus waveguide and the bent waveguide. To overcome this problem and increase coupling factor for critical coupling, straight waveguide sections are inserted into the bent waveguide sections in the coupling region next to the bus waveguide. This transforms our design to a *racetrack* resonator. With a coupling gap of 0.7-0.8 μm, the need for a racetrack shape becomes inevitable as the ring radii gets smaller, since coupling factor is too small for smaller radii. Output graphes of an coupling simulation is seen in Fig. 4.8. In the part (a) of the figure, XZ contour map shows optical field in the coupling region of a racetrack resonator. While the (b) part plots waveguide mode power as function of propagation distance. The calculated coupling factors for a number of radius as function of straight section length is given in Fig.4.9 for TE polarization. A similar calculation was performed for TM polarized light input and the results are plotted in Fig.4.10. A quick comparison shows that the TE coupling factors are much more higher than those calculated for TM polarization for the same same geometry. This is due to difference in the TE and TM mode profiles, which is also responsible for the difference in calculated bending losses for both polarizations.

Using equations computed in previous section for optical intensities (Eqs.4.12, 4.15 and 4.17), and estimating total optical loss in the resonators, one can find the necessary coupling factor. BPM results were used to find the gap and straight section length that provide necessary coupling factor. The total optical loss includes both bending and propagation losses. Bending loss is determined through analytic calculation and BPM simulations as mentioned earlier, while the propagation loss

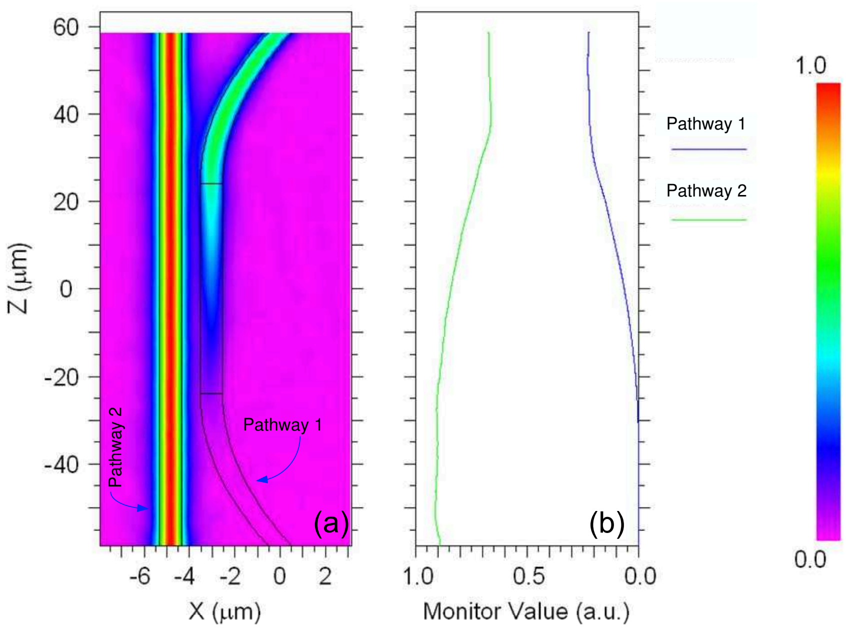

Figure 4.8: Output of a BPM simulation of coupling from a bus waveguide. Bends have radius of 200 μm and straight section length and the gap are 48 and 0.8 μm, respectively.

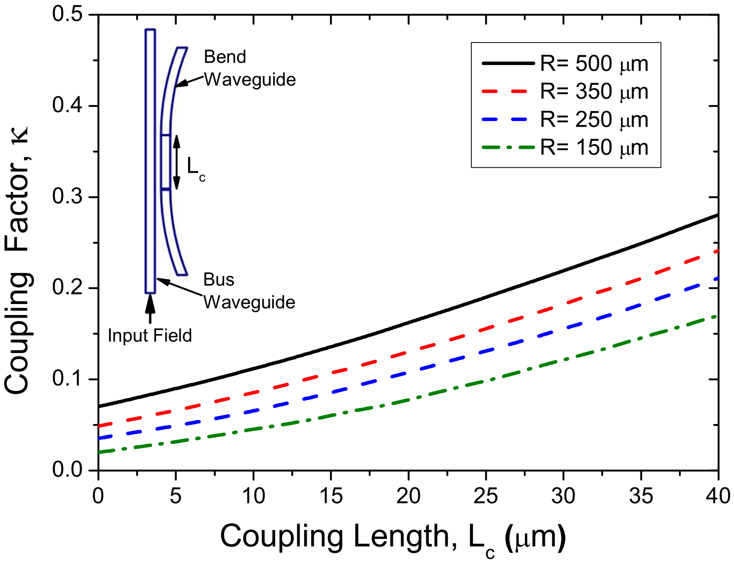

Figure 4.9: Power coupled from bus waveguide to racetracks with various radii for TE polarization as a function of straight section length for gap of 0.8 μm.

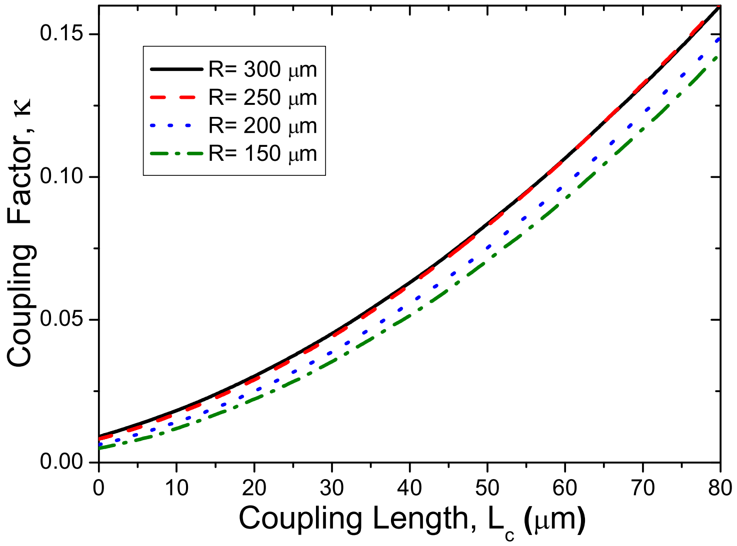

Figure 4.10: Power coupled from bus waveguide to racetracks with various radii for TM polarization as a function of straight section length for gap of 0.8 μm.

is experimentally measured on waveguides fabricated with same dimensions used for the bus waveguides of the ring resonator system. We find the upper limit for propagation loss to be 5.5 dB/cm (see Chapter 2).

Analytical results of the resonator analysis are used to write Mathcad programs to estimate the response of ring resonators. The programs let you to match resonator loss with a coupling factor, iteratively. This is needed, since to match a resonator loss with a coupling factor means increasing the straight section which means an increase in resonator length and loss. Resonator characteristics of designed resonator can also be extracted from the programs. A careful analysis is made to match these values. The gap between bus and ring which is 0.8 μm is large enough to print by photolithography and small enough to have reasonable straight resonator section lengths. The designed resonators have bends with radii ranging from 150 to 500 μm and racetrack shapes to increase coupled power from bus waveguide.

The second gap for double bus ring resonator is calculated by matching two coupling factors and the resonator loss which may be a greater deal. You may

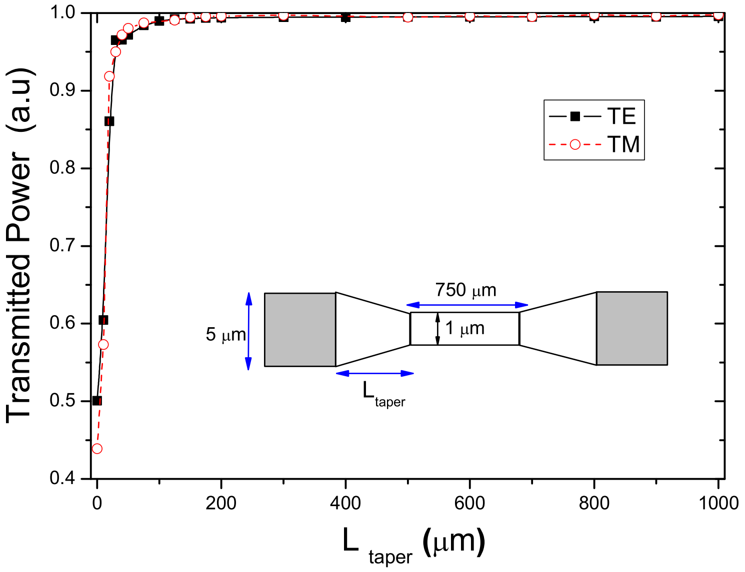

Figure 4.11: BPM simulation results for the design of tapers. The inset shows the layout used for simulations.

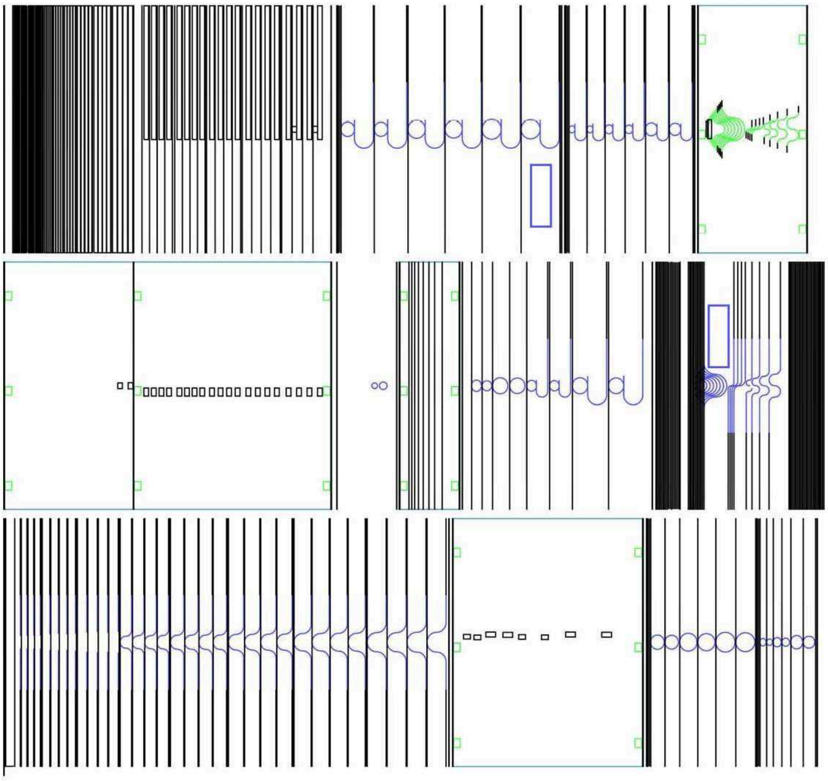

Figure 4.12: The layout of the drown mask for SOI racetrack resonators.

simply use the same value for the second gap (on drop port side) but a carefully chosen asymmetric gap may result in better resonator responses. I chose the second option in design of double bus resonators.

To increase the the coupling efficiency from single mode fibers to bus waveguide we implemented tapers at the beginning and end of the bus waveguides. The optimum taper design was obtained after a number of BPM simulations Fig. 4.11. According to simulations, a taper length of 200 μm is enough for optimum coupling. We implemented a length of 1000 μm in the designed mask.

We included all the resonators designed in a mask. The L-edit software [73] was used to draw the mask. Various values for bending radius and racetrack straight section lengths and coupling gaps were included. The overview of the drown mask is given in Fig.4.12.

4.3 Micro-Ring Resonators as Displacement Sensors

(The work reported in this section was performed in collaboration with Mr. C. Kocabas as a part of his Ms. Thesis [74].) During the design of the ring resonators, potential applications were also considered. As a part of this effort, integration of micro-ring resonators on micromachined cantilevers for displacement sensing purpose was proposed and analyzed. These designed sensors may be used for scanning probe microscopies [75].

Many scanning probe microscopies require the measurement of displacement with high sensitivity. A good example is atomic force microscope (AFM) [76] , based upon the principle of sensing the forces between a tip and a surface. These forces induce the displacement of the tip mounted on a cantilever. There is a great need to determine the displacement of the cantilever with high sensitivity to work out the attractive and repulsive forces between surface and the tip. There are many methods to determine the tip displacement; these are tunnelling [76]

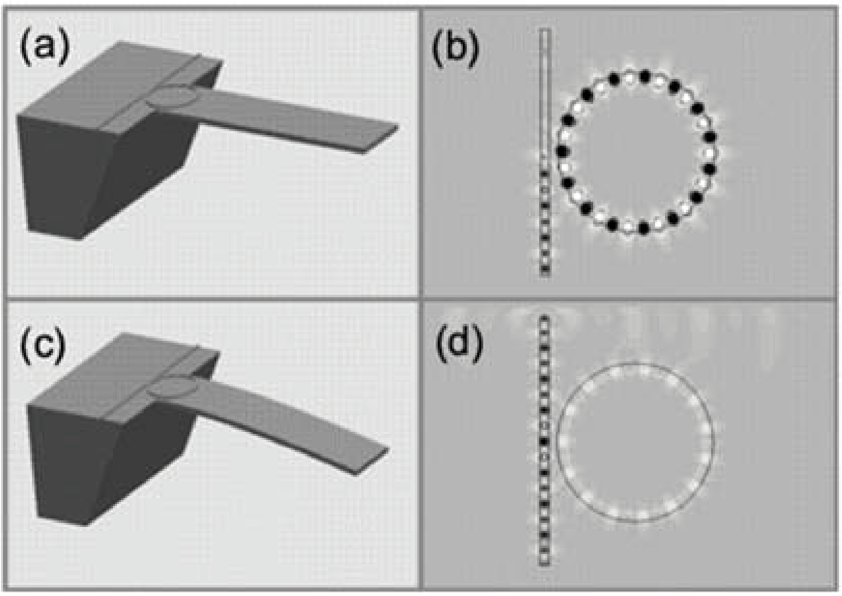

Figure 4.13: A schematic illustration of the operational principle for the integrated micro-ring resonator displacement sensor, (a and c) shows the cantilever for unbend and bend condition, (b and d) shows the field distribution on the ring resonator on the cantilever.

, optical lever [77] , interferometry [78] , piezo-resistive [79] and piezoelectric detections [80] and interdigital detection [81] techniques. Integrated optical detection method has many advantages over the others. First, an integrated sensor does not require any alignment during the scanning of the surface and it is possible to scan large areas. Second, integrated sensors are suitable for cantilever arrays due to their compactness, simplicity and potential for mass production. It should also be mentioned that integrated sensors such as piezo-resistive ones have less sensitivity than the external sensors such as optical levers. Using an integrated optical sensor, it is expect to achieve as high sensitivity as external sensors. Integrated optical devices can be inexpensive and they can be used in harsh environments such as UHV systems and electromagnetically active environments. Recently there have been many studies on the integrated optic pressure sensors, bio-sensors, temperature sensors and strain sensors. These sensors consist of an integrated optical device such as Mach-Zehnder interferometer [82] , directional couplers [83] , ring-resonators [84] , whose transmission characteristics change due to external effects.

Here, a new integrated optical sensor for scanning probe microscopes is proposed (see Fig. 4.13). In this design, an optical waveguide coupled to a high finesse micro-ring resonator integrated with a cantilever is used as a strain sensor to deduce displacement. Basically, stress due to displacement of the cantilever changes the local refractive index on the ring resonator through the photo-elastic effect , and index change cause modifications in the transmission characteristics of the optical waveguide coupled ring resonator. Monitoring the intensity modulation trough the optical waveguide, it is possible to determine the cantilever displacement with high accuracy. Finite Element Method (FEM) simulations were carried out to get optimum sensor design and Finite Difference Time Domain simulations (FDTD) are used to get the transmission characteristics of optical waveguide coupled ring resonators. To achieve high sensitivity, different types of ring resonators have been studied.

4.3.1 Physical Analysis

In the method employed in this work [85], a micro-ring resonator integrated on a cantilever is used to measure displacement. The atomic forces make the cantilever deflect from equilibrium and this deflection produces stress on the cantilever surface. Index change on the ring due to the stress causes a shift in the resonant wavelength. The stress reaches its maximum value at the supporting point of the cantilever and it decreases linearly along the cantilever. Maximum stress on the surface of the base of the cantilever as a function of tip displacement, z, can be written as;

$$\sigma_{max} = \frac{3Et}{2l^2} z \tag{4.32}$$

where E is the Young's modulus of the cantilever material, t is the thickness, and l is the length of the cantilever. Due to the photo-elastic effect, effective index changes due to the stress and through the equation,

$$n_{eff} = n_0 + \sum_i C_i \sigma_i \tag{4.33}$$

where, C_i is the stress optic constant of waveguide and σ_i is the local stress. For GaAs longitudinal and transverse stress optic coefficients are $1.7x10^{-11}\ Pa^{-1}$

$1x10^{-11}\ Pa^{-1}$, respectively [86]. Longitudinal stress is much larger than the transverse stress, which can be neglected, so that

$$\Delta n_{max} \simeq C_l \sigma_l \simeq \frac{3C_l Et}{2l^2} z \tag{4.34}$$

Change in refractive index can also be written as function of the force applied on the tip. From Hooke's law, force on the rectangular cantilever can be expressed as

$$F = kz = \frac{wEt^3}{4l^3} z \tag{4.35}$$

where k denotes the spring constant of the cantilever, then change in refractive index can be written as,

$$\Delta n_{max} \simeq \frac{6C_l l}{wt^2} F \tag{4.36}$$

From Eq. 4.35 and 4.36, the refractive index change depends on the geometry of cantilever and photo-elastic constant of the material. As the stress induced index change is not uniform on the ring total accumulated round trip phase on the ring can be written as,

$$\Delta\Phi = \frac{2\pi}{\lambda} \int_{ring} \Delta n \ dl \simeq \frac{2\pi C_l}{\lambda} \int_{ring} \sigma_l \ dl \tag{4.37}$$

where λ is the wavelength. In order to achieve large phase shifts, total length of the ring must be kept large and the cantilever material with a large elasto-optic coefficient must be chosen. A schematic illustration of the operational principle for the integrated micro-ring resonator displacement sensor extracted from Finite Difference Time Domain(FDTD) simulation is given in Fig. 4.13.

4.3.2 Waveguide Design

Although, it is possible to design the sensor for other material systems, we design and analyze ring resonators on GaAs/AlGaAs platform. The waveguides designed are deeply etched to achieve strong confinement [87] , which is essential to minimize waveguide bending losses. The general waveguide structure is seen in Fig. 4.14(a). The fraction of Al, x, and the geometry of the waveguide are chosen so that single mode propagation is assured. The basic limitation to the resonator and therefore to the waveguide design is the need to propagate light

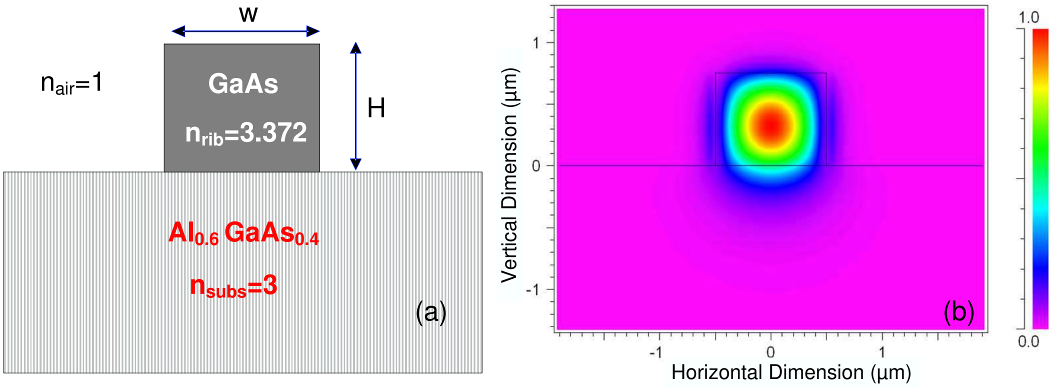

Figure 4.14: Single mode waveguide structure (a), and its mode distribution (b).

in a small radius of curvature of less than 25 μm with minimum loss, since a typical cantilever width is about 50 μm. A few trials of BPM simulations with different Al mole fraction and waveguide width, w, and height, H led us to a single mode waveguide structure which can be fabricated using optical lithography. This structure has 0.6 as x, 1 and 0.75 μm as w and H respectively. n_{eff} is 3.192 for TE polarization which is found by mode calculation using a commercial BPM program (see Fig. 4.14(b)). Performed bending loss analysis (as done in previous section for SOI waveguides) suggested that it would be safe to use an R value of 20 μm for the ring.

4.3.3 Ring Resonator as Displacement Sensor

For the purpose of sensing displacement, we are mainly interested in modulation applications of ring resonators. It should be possible to obtain a large modulation in transmitted optical power by small variations of the refractive index. This kind of modulation is useful only if the resonance wavelength shift remains in the bandwidth of the resonator. Such shifts can only be achieved through a controllable change in optical path length of resonators, which is a function of resonator physical length and effective refractive index. Here, stress induced refractive index change is employed. When the ring resonator is designed to have a high-Q factor, the modulation is dramatic due to steep fall of the transmission

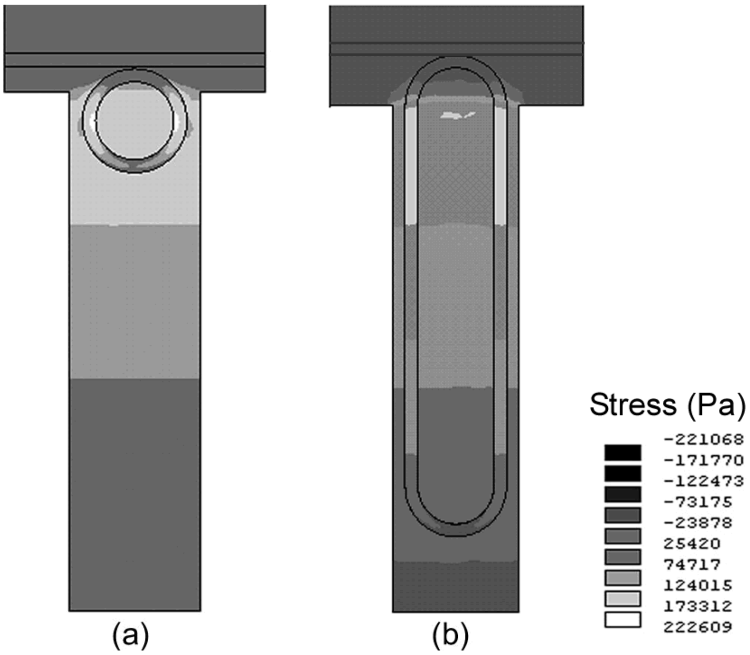

Figure 4.15: Longitudinal stress distribution on the cantilevers with a ring (a) and a race-track (b) shape resonator. Long straight arms in the race-track resonators are useful for increasing the accumulated phase shift.

dip. Transmission dips would be more stepper when resonators are designed to work at the critical coupling regime.

As the operational principle of the ring resonator coupled waveguide sensor depends on the stress distribution along the cantilever, we have calculated the 3-D stress distribution using Finite Element Method (FEM) simulations, for which; Young's Modulus of 0.86 $\times 10^{11}$ N/m^2, and Poisson's ratio of 0.31 were used. Static stress analysis was performed using ANSYS [88] software. The mesh was increased in the region where ring resonator was placed. The analysis performed here uses the stress at the surface. The local stress on the top surface decreases along the z direction and becomes negative on the opposite surface. Fig. 4.15 (a) shows the stress contours on the the ring resonator obtained from the FEM simulation. Maximum stress occurs at the supporting point of the cantilever and decreases linearly along the cantilever. From the figure, it is clearly observed that large stress occurs on the two sides of the ring which are parallel with the major symmetry axis of the cantilever. Calculated total accumulated phase on the ring with a radius of 20 μm is 5×10^{-4} *rad* for 100 $\mathring{A}$ deflection of the cantilever. In order to increase the accumulated phase shift, the parallel sides may be kept longer. The optimum design is a race-track shaped resonator, because of its two long parallel sides where stress is much larger than the curved sides. Fig.4.15 shows the stress contours on the race-track resonator. Stress distribution reaches to its maximum value on the surface of the waveguide and decreases linearly along its thickness. For the sensitivity calculations, we averaged stress along the thickness of the waveguide. Average value of the stress is equal to the stress in the middle of the waveguide where the intensity of the guided light is maximum. As the stress distribution is calculated with the waveguides on the surface of the cantilever, stress also varies along the width of the waveguides in the curved sections of the devices. We neglected the variation of stress in the curved sections and used the value of the stress in the middle of the waveguide in the calculations. Phase shift can be approximated as;

$$\Delta\Phi \simeq \frac{3\pi C_l E t L_{rt}}{2\lambda l^2}\, z \tag{4.38}$$

where L_{rt} is the length of the race-track resonator. From the equation, it is observed that the phase shift is linearly proportional to the cantilever deflection and it is related to the cantilever geometry and mechanical properties of the cantilever material. For higher sensitivity, total length of the ring and the elasto-optic coefficient of the material must be large. Phase shift can also be written as a function of force applied on the tip so that,

$$\Delta\Phi \simeq \frac{6\pi C_l l L_{rt}}{\lambda w t^2}\, F \tag{4.39}$$

where F is the applied force, w is the width of the cantilever. In order to increase the phase shift due to the applied force we have to keep the length long and the thickness of the cantilever small which results in a trade-off between force and displacement sensitivity. It is not possible to achieve high displacement sensitivity as well as high force sensitivity. We can conclude that short and thick cantilever is sensitive to displacement measurements whereas long and thin cantilevers is more sensitive for force detection. One interesting result which is seen from Eq. 4.39 is that the phase shift does not depend on the Young's modulus of the cantilever. For small displacements, output intensity is a linear function of displacement.

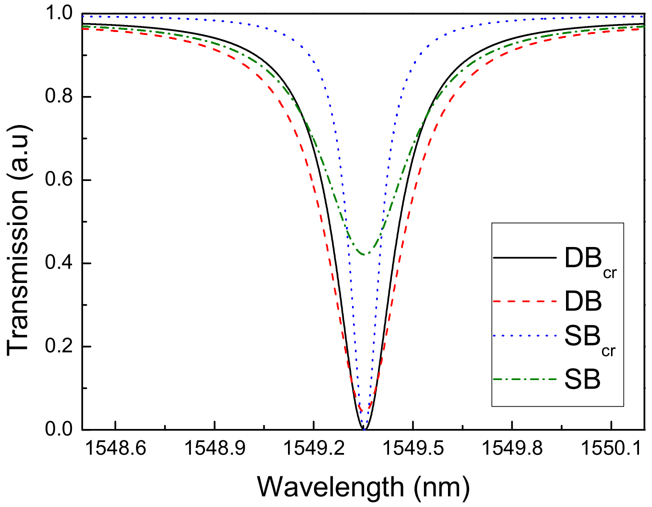

Figure 4.16: Transmission spectrum of single bus and double bus race-track resonators for both with (SB$_{cr}$ and DB$_{cr}$) and without (SB and DB) critical coupling condition, respectively. The increase in slope of the resonance when critical coupling is achieved is clearly observed.

4.3.4 Cantilever Design and Sensitivity Analysis

Fundamental mechanical parameters of an AFM cantilever are its spring constant and resonant frequency. The optimal values of these parameters depend on the mode of the operations, namely contact mode, non-contact mode, and intermittent contact mode. $GaAs$ has a large photo-elastic constant which makes it a suitable material for fabrication of integrated optical devices and cantilever [89, 90, 91]. Other materials such as Si_3N_4 and Si can also be used with varying sensitivities. Our design is based on rectangular cantilevers which are compatible with well established micromechanical fabrication technology. Typical micromachined cantilevers for AFM have lengths of 100 μm to 400 μm, widths of 20 μm to 50 μm and thicknesses of 0.4 μm to 10 μm. A large spring constant is preferable for non-contact mode and intermittent mode operations. On the other hand, low force constant is preferable for contact mode operations. The resonant frequency is required to be a few kHz in order to minimize the external effects [92] .

The sensitivity of displacement sensors is the essential property of the atomic force microscopies. The minimum detectable force and the displacement depend on the sensitivity of the sensor and the noise of the system. Integrated sensors have less sensitivity than external ones. There have been several studies to increase the sensitivity of the integrated sensor, but the best sensitivity achieved so far is $\sim 10^{-6}$ A^{-1} [89] , which is two orders of magnitude less than the sensitivity of the interferometric detection [78]. Force sensitivity can be defined as the variation of the current on the detector per unit force applied on the tip and with the same logic, displacement sensitivity can be defined as the variation of the current on the detector per unit displacement of the cantilever. The current on the detector is proportional to the light falling on it,

$$i = \frac{\eta I_t}{h\nu} \tag{4.40}$$

where η is the quantum efficiency of the photo detector, I_0 is the incident optical power, ν is the frequency of the light. Therefore,

$$\frac{\Delta i}{i_0} = \frac{\Delta I}{I_0} \tag{4.41}$$

The detected power, I_t depends on the transmission characteristics of the ring resonator coupled waveguide. Transmission of the single and double bus ring resonators are given in the Eq. 4.12 and Eq. 4.15, respectively. In Fig. 4.16, we plot the transmission spectrum for a single bus and double bus resonators with and without critical coupling condition. Achieving the critical coupling condition, it is possible to have very high modulation depth and very narrow spectral response. Output intensity variation with cantilever displacement is given in Fig. 4.17. We can write displacement and force sensitivities as

$$S_d = \frac{\Delta I_t}{I_0 \Delta z} = \frac{1}{I_0}\frac{dI_t}{d\phi}\frac{d\phi}{dz} \tag{4.42}$$

and

$$S_f = \frac{\Delta I_t}{I_0 \Delta F} = \frac{1}{I_0}\frac{dI_t}{d\phi}\frac{d\phi}{dF} \tag{4.43}$$

In Table 4.1, we compare the calculated sensitivities of the ring resonators for single bus and double bus configurations with and without critical coupling condition. The highest sensitivities are achieved under critical coupling conditions.

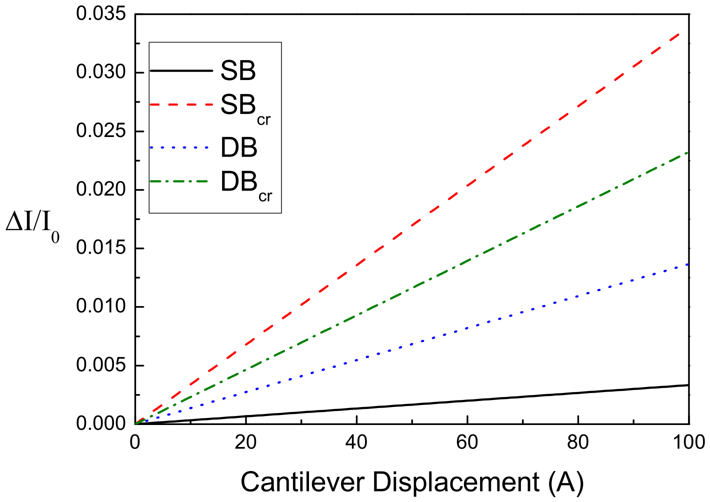

Figure 4.17: Transmitted intensity variation with cantilever displacement for single and double bus race-track resonator with (SB_{cr}, DB_{cr}) and without (SB, DB) critical coupling condition achieved. The best results are obtained under critical coupling condition.

The sensitivity of the ring resonator is wavelength dependent. Fig. 4.18 shows the wavelength dependence of the race-track ring resonator. The most sensitive operation can be achieved at the wavelength for which the output intensity has the steepest slope. The calculated sensitivities are promising and it should be possible to achieve sensitivities as high as the sensitivity of the interferometric detection. Sensitivity of the detector depends mainly on the design of the resonator and the waveguide. Considering the round trip losses, we design the resonator to accomplish the critical coupling condition. To achieve critical coupling, gap between straight waveguide and ring should be precisely controlled. In our design we estimate propagation loss to be on the order of 10 dB/cm for waveguides. Under this condition, gap size for critical coupling should be lower than 0.1 μm which can be defined by e-beam but not optical lithography. The solution for optical lithographic fabrication would be to vertically couple the ring resonator and the bus waveguide [45], for which coupling gap can be controlled precisely through standard deposition or epitaxial growth techniques. But even if critical coupling is not achieved, the calculated sensitivities are still very good, especially

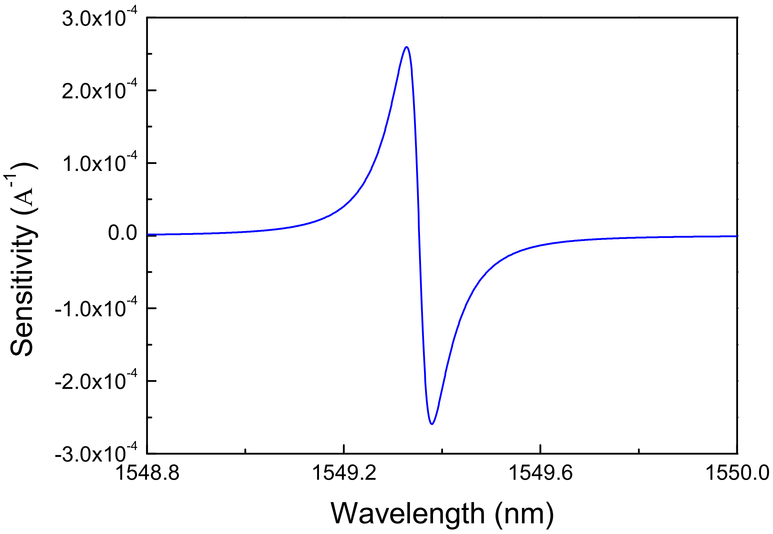

Figure 4.18: Sensitivity vs wavelength for single bus race-track case with critical coupling achieved.

for the double bus structure. In the double bus structure, the second bus can be placed next to the ring but opposite to the first waveguide.

Device	SB	SB_{cr}	DB	DB_{cr}
Sensitivity (Å^{-1})	3.37 10^{-5}	3.39 10^{-4}	1.37 10^{-4}	2.33 10^{-4}

Table 4.1: Calculated displacement sensitivities for single and double bus ring resonator with (SB$_{cr}$, DB$_{cr}$) and without (SB, DB) critical coupling condition achieved.

In summary, a novel integrated ring resonator displacement sensor was proposed for scanning probe microscopies. We design and analyze the feasibility of the integrated optical sensor. The concept based on elasto-optic effect is discussed. The design of the ring resonator was described and theoretical investigation of the force and displacement sensitivity was presented. The design of GaAs based cantilever with integrated ring and race-track resonator have been described in detail. We find that integrated optical sensor is attractive because of its high sensitivity and simplicity. We introduce a new application area for integrated optics. This design is a good alternative for piezoresistive cantilevers especially in electromagnetically active environments. Integrated sensors are suitable for cantilever arrays due to their compactness, simplicity and compatibility with mass production. No need for alignment, compactness, and high sensitivity are the main advantages of this method.

Chapter 5

SOI Racetrack Resonators: Fabrication and Results

This chapter is devoted to realization of the resonators designed in previous chapter and their characterization. There is no difference between resonators discussed in following 3 sections in terms of fabrication. They are realized on SOI chips following a fabrication sequence of optical photolithography (PL1), RIE (RIE1 or RIE2), SiO_2 deposition in PECVD and silicon substrata thinning for better cleavage as explained in Chapter 2. Fig. 5.1 summarizes the fabrication procedure.

The chips were mounted in our integrated optics measurement setup. The input optical signal was obtained from an external cavity tunable laser with a resolution of 1 pm coupled to the straight bus waveguides using a tapered and lensed fiber with a spot size of 2 μm. The polarization of the input light was controlled by a fiber polarization controller before being coupled to the chip. An infrared camera is used to align the fiber and the input facet. The light at the output of the bus waveguide was collected with a microscope objective and passed through a polarizer of high extinction ratio before reaching a Ge photodetector. The transmitted optical powers were obtained as a function of wavelength.

The results for resonators and details of further fabrication processes if any are given in the following sections along with detailed analysis.

5.1 High-Q Racetrack Resonators

The resonators results of which are given in this subsection are based on single mode SOI waveguides of 0.42 μm rib height. The chip had a length of 7 mm after cleavage. Optical micrograph showing one of the fabricated racetrack resonators is displayed in Fig.5.2. Single bus racetrack resonators of bending radii ranging from 150 to 500 μm are characterized for both TE and TM polarizations. The measured TE transmission spectra of some of fabricated resonators are shown in Fig.5.3 for various bending radii measured at the throughput port of the ring resonator system. A sample of spectra for TM polarization can be seen in Fig.5.4. In addition to the sharp dips in the throughput spectrum, small amplitude oscillations due to Fabry-Perot resonances between the ends of the straight bus waveguide are clearly observed. The optical (including free spectral range (FSR), full width at half maximum (FWHM), finesse, Q-factor and modulation depth(M.D.)) as well as some physical characteristics of the resonators shown in Fig.5.3 and Fig.5.4 are summarized in Table.5.1 and Table.5.2, respectively. Q-factors of as high as 119000 were observed for both polarizations.

Racetrack resonators of bending radius smaller than 150 μ were also fabricated with etch depth of 0.42 μm, to test level of validation of our bending loss estimation. A set of measured spectra is given in Fig.5.5. The resonance dips smear out for the resonators with R=120 μm bends for TE while resonance dips are observed even for resonators with R=60 μm bends for TM polarization. We should note that the resonator losses increase drastically for resonators with R=150 μm and smaller radius for both polarizations. However, the increase is larger in the case of the TE polarization. This should be a result of larger bending loss for TE polarization in small radii bends.

To compare resonator round trip losses, one can curve fit Eq.4.12 to measured spectra. I performed the fitting analysis for resonators of bending radii from

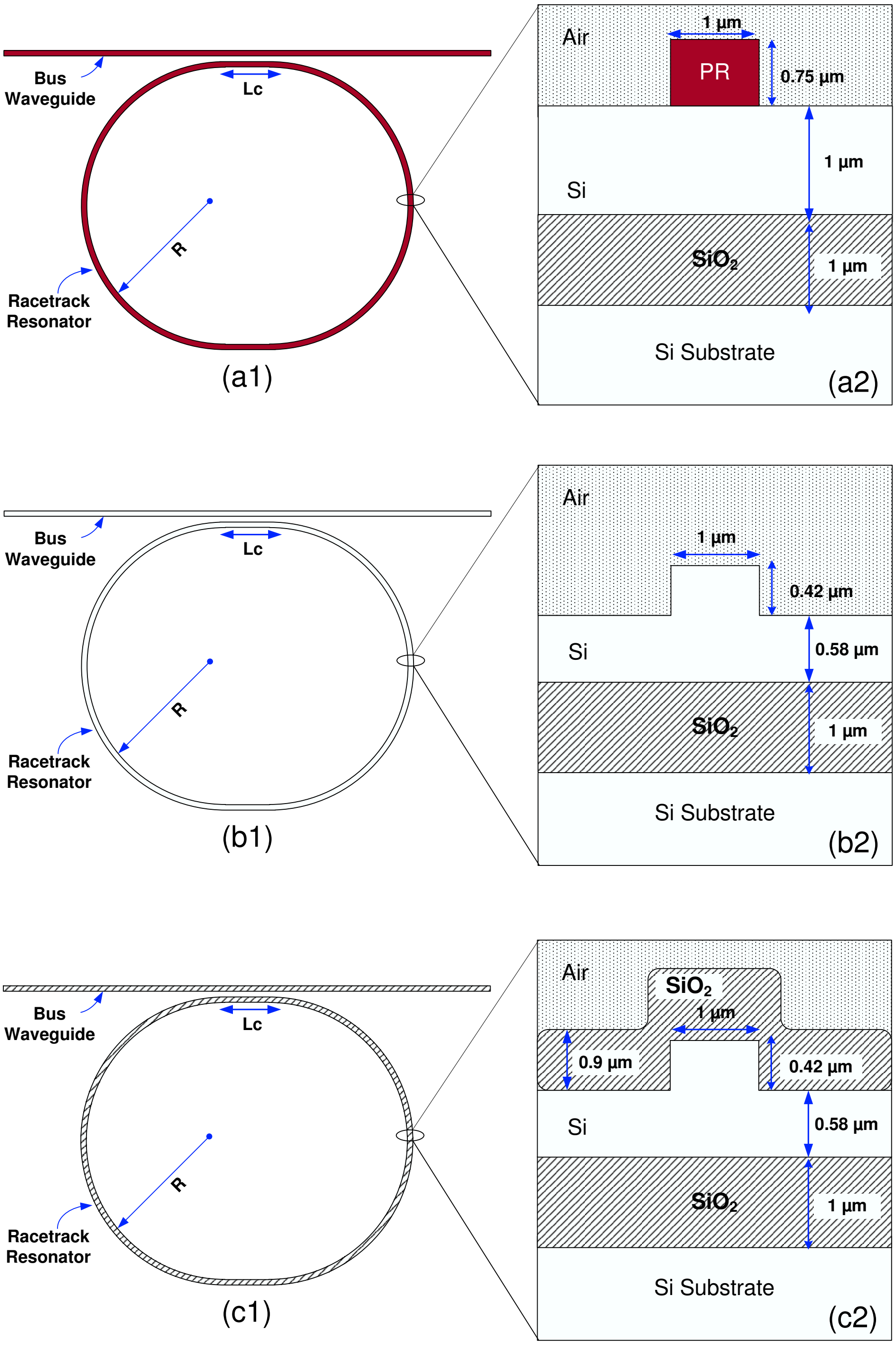

Figure 5.1: SOI rib waveguide racetrack resonator fabrication steps. Top and cross-sectional views are given. (a1,a2) Photolithography is used to transfer patterns to photoresist (PR), (b1,b2) Si layer is etched using RIE and remaining PR cleaned, (c1,c2) SiO_2 is deposited using PECVD.

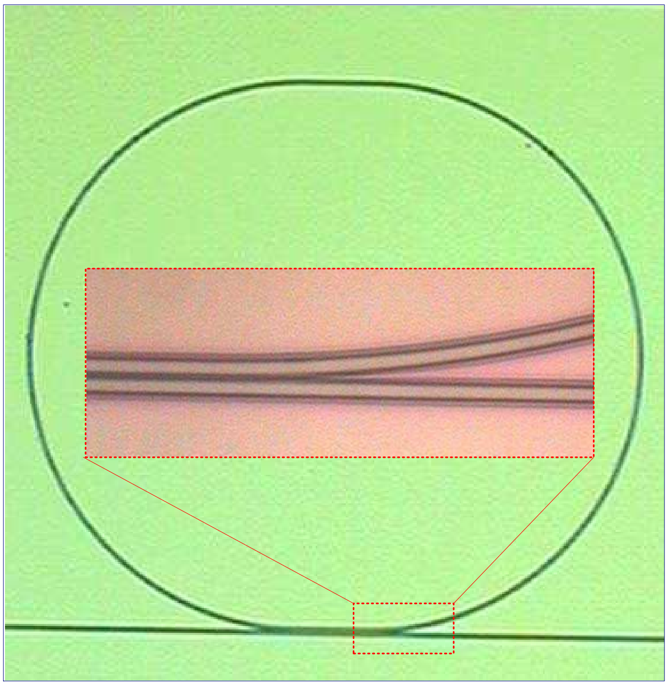

Figure 5.2: Optical micrograph of one of the fabricated racetrack resonators. Inset shows the coupling region.

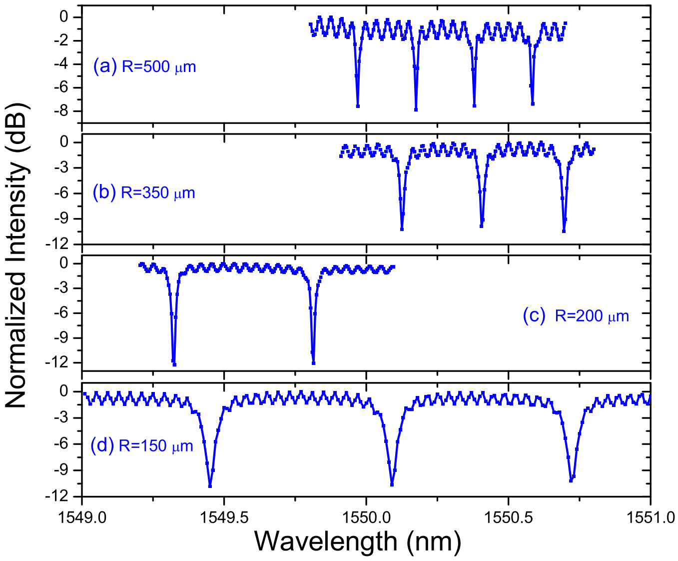

Figure 5.3: Measured TE transmission spectra of the fabricated silicon-on-insulator rib waveguide racetrack resonators for radii of 500, 350, 200 and 150 μm for the same span of wavelengths.

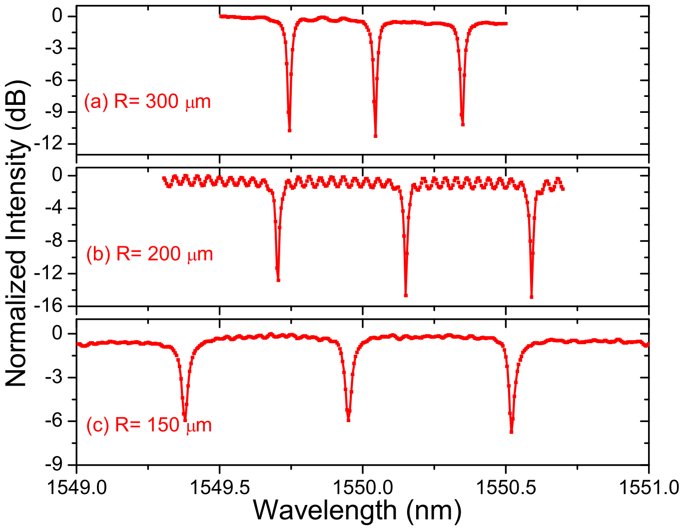

Figure 5.4: Measured TM transmission spectra of the fabricated silicon-on-insulator rib waveguide racetrack resonators for radii of 300, 200, and 150 μm for the same span of wavelengths.

50 to 500 μm using Mathcad programs mentioned earlier. Such a analysis can provide resonator loss and coupling factor between bus waveguide and racetrack. The Eq.4.12 is an interchangeable equation in terms of loss and coupling terms. That is, two different pairs of loss and coupling factor values may fit a set of measurement data. Therefore, in fitting process, one should start with good initial values in order to not to the get wrong fitting parameters. We have chosen to rely on the coupling factors from BPM calculations and use them as the starting value in fitting process. The best fit to data can be obtained by small iterations in coupling factor and resonator loss.

In Fig.5.6, two representative examples of fitting results are displayed. The extracted values from the analysis that is coupling factors and resonator losses are summarized in Table.5.3 for TE polarization and in Table.5.4 for TM polarization. In the tables, BPM calculated coupling factors for both coupling gaps in design and coupling gaps narrower than the design values by 0.1 μm are also included. The latter values (for narrower gaps) show much better agreement with the extracted coupling factors. This observation suggests that the fabrication

R (μm)	L$_c$ (μm)	FSR nm	FWHM pm	Fin.	Q-F.	M.D. (dB)
500	2	0.205	13	15.8	119000	7.8
350	32	0.290	13	22.3	119000	10.4
200	26	0.490	17	28.8	91000	12.2
150	38	0.630	35	18.0	44000	10.8
120	78	0.799	350	2.3	4430	7.4
100	72	1.070	315	3.4	4920	11.7
80	66	1.190	480	2.5	3230	5.4
60	62	1.510	652	2.3	2380	4.6

Table 5.1: Characteristics of resonators for which measured TE spectra are given in Fig.5.3 and Fig.5.5

R (μm)	L$_c$ (μm)	FSR nm	FWHM pm	Fin.	Q-F.	M.D. (dB)
300	110	0.300	13	23.1	119000	11.2
200	92	0.445	15	29.7	103000	14.8
150	88	0.570	13	43.8	119000	6.7
120	78	0.782	123	6.4	12600	7.7
100	72	0.945	164	5.8	9150	10.2
80	66	1.170	158	7.4	9810	8.5
60	62	1.500	234	6.4	6620	10.7
50	68	1.730	643	2.7	2410	9.7
40	74	1.980	875	2.3	1770	9.5

Table 5.2: Characteristics of resonators for which measured TM spectra are given in Fig.5.4 and Fig.5.5

procedure leads to narrower gaps than those in the design.

The extracted resonator round trip losses,$\alpha_{R.T.}$ are plotted as a function of resonator radius in Fig. 5.7(a). We can compare $\alpha_{R.T.}$ shown in Fig. 5.7(a) with calculated and simulated bending losses in Fig. 4.6. But, two notes should be pointed out. One is that $\alpha_{R.T.}$ is total loss in a resonator including bending and scattering and material (if any) losses and the other one is that the calculated bending losses in Fig. 4.6 are given for 90° bends. Keeping these points in mind, one can easily realize the good agreement between the Fig. 5.7(a) and Fig. 4.6. The increase in $\alpha_{R.T.}$ for smaller radii should be due to increase in bending loss. Therefore, resonators with radii larger than 200 μm for TE and larger than

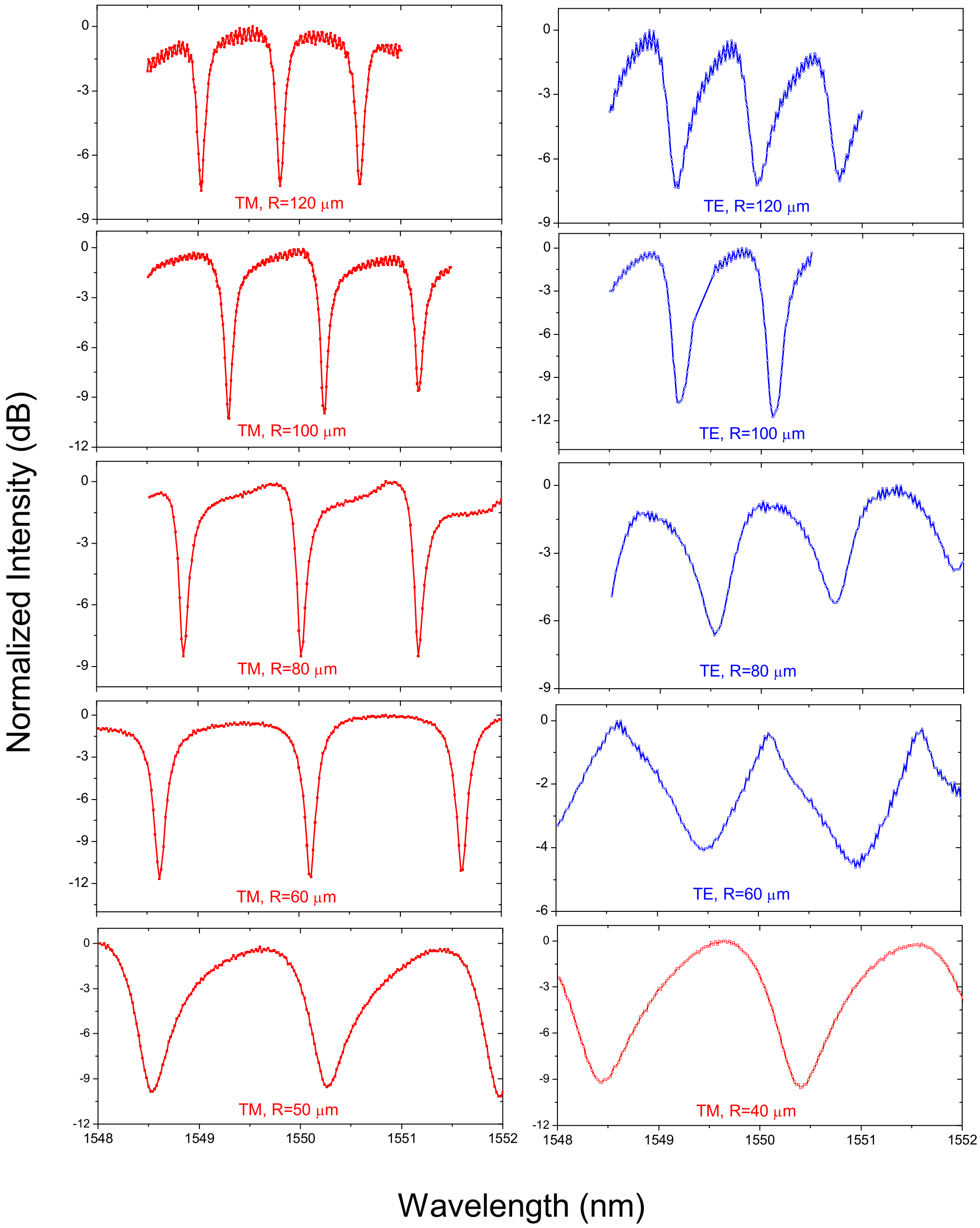

Figure 5.5: Measured TM and TE transmission spectra of the fabricated silicon-on-insulator rib waveguide racetrack resonators for radii of 40 to 120 μm.

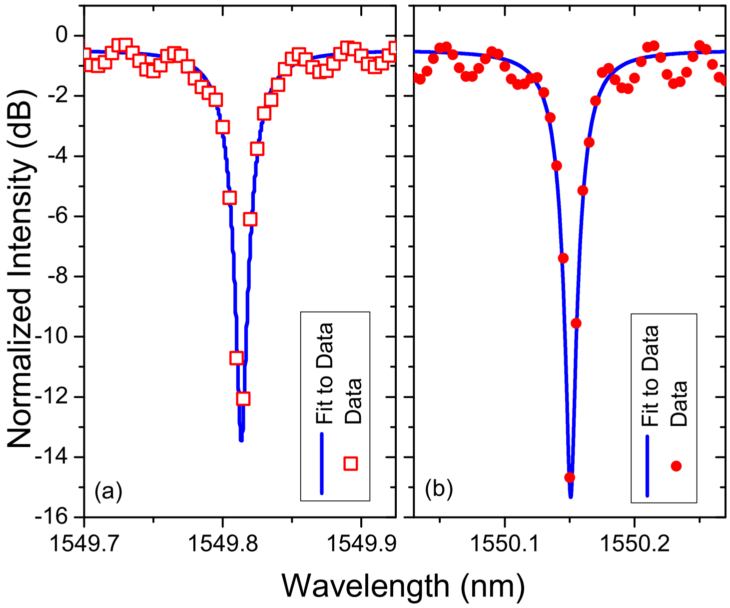

Figure 5.6: (a) Curve fit to measured TE transmission spectra for R=200 μm (b) Curve fit to measured TM transmission spectra for R=200 μm.

R (μm)	L$_c$ (μm)	g (μm)	κ_{BPM-g}	$\kappa_{BPM-g'}$	κ_{fit}	κ_c	$\alpha_{R.T.}$ (dB)	α (dB/cm)
500	2	0.8	0.08	0.12	0.11	0.26	1.29	4.1
350	32	0.8	0.21	0.31	0.31	0.18	0.86	3.8
200	26	0.8	0.12	0.19	0.18	0.11	0.52	4.0
150	38	0.8	0.16	0.25	0.21	0.35	1.88	18.5
120	78	0.7	0.58	0.78	0.77	0.96	13.5	148.0
100	72	0.7	0.51	0.71	0.71	0.85	8.2	106.0
80	66	0.7	0.44	0.62	0.62	0.92	11.1	175.0
60	62	0.7	0.38	0.56	0.99	1.0	51.1	1020

Table 5.3: Extracted values from curve fitting analysis of resonators for which measured TE spectra are given in Fig.5.3 and Fig.5.5. Results of BPM calculations for coupling factors are also included. ($g^{'} = g - 0.1$ μm)

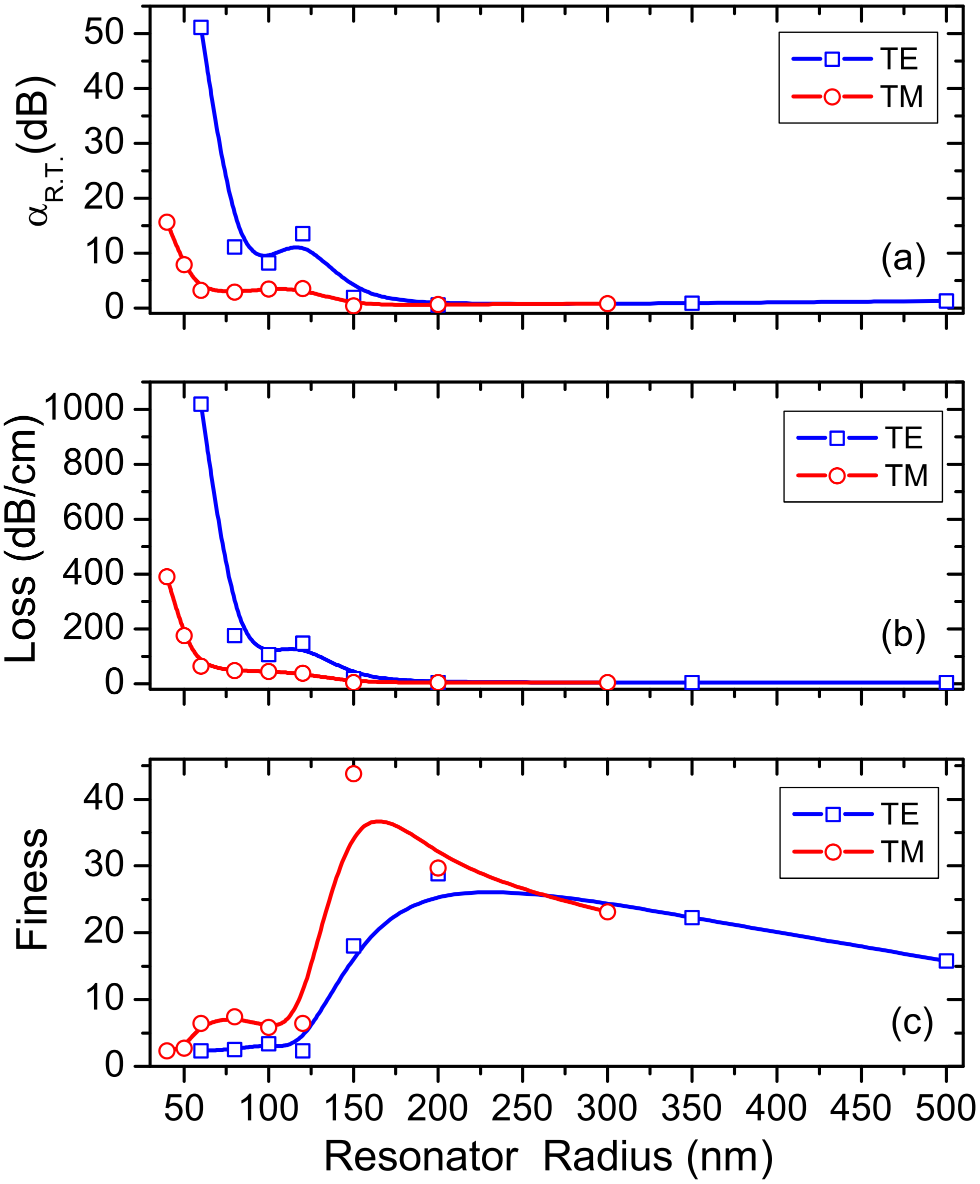

Figure 5.7: The extracted (a) resonator round trip and (b)effective propagation losses and (c) measured finesse values for TE and TM polarizations. The solid lines are to guide the eye.

R (μm)	L$_c$ (μm)	g (μm)	κ_{BPM-g}	$\kappa_{BPM-g'}$	κ_{fit}	κ_c	$\alpha_{R.T.}$ (dB)	α (dB/cm)
300	110	0.8	0.18	0.32	0.25	0.16	0.74	3.5
200	92	0.8	0.13	0.24	0.18	0.14	0.65	4.5
150	88	0.8	0.12	0.22	0.22	0.09	0.39	3.5
120	78	0.7	0.17	0.33	0.28	0.55	3.5	38.5
100	72	0.7	0.15	0.28	0.34	0.54	3.4	44.1
80	66	0.7	0.12	0.23	0.26	0.49	2.9	48.1
60	62	0.7	0.10	0.20	0.35	0.52	3.2	64.4
50	68	0.7	0.11	0.22	0.66	0.84	7.9	175.6
40	74	0.7	0.13	0.25	0.91	0.97	15.6	390.0

Table 5.4: Extracted values from curve fitting analysis of resonators for which measured TM spectra are given in Fig.5.4 and Fig.5.5. Results of BPM calculations for coupling factors are also included. ($g^{'} = g - 0.1$ μm)

150 μm for TM are bending loss free as we predicted during the design. Also the extracted resonator loss graph proves our prediction of larger bending losses for TE polarization at smaller radii to be correct. Another observation with extracted $\alpha_{R.T.}$ values is that resonators with lower $\alpha_{R.T.}$ values have the higher finesse value. This feature is shown in Fig. 5.7(a) and (b).

In the Table. 5.3 and 5.4, calculated coupling factors, κ_c that would be necessary to achieve critical coupling for characterized resonators are also tabulated. κ_c was calculated by Eq. 4.11 using extracted resonator losses from the fitting analysis. As a function of resonator radius, calculated κ_c's are plotted in Fig. 5.8. κ_c and κ_{fit} values are most close at radius of 200 μm for both polarizations. That is for 200 μm resonators are closer to critical coupling condition than other resonator. This conclusion can also be verified by a look at measured modulation depths in Table 5.1 and 5.2. The highest modulation depths are 12.2 dB for TE and 14.8 for TM polarizations which are measured for R=200 μm resonators.

As a conclusion for this section, we demonstrated resonators with quality factors as high as 119000 for both polarizations. Furthermore, resonators have finesse values larger than 28 for TE polarization and larger than 43 for TM polarization. Using standard optical photolithography technology, the quality factor values reported here are the highest Q values achieved in the SOI platform,

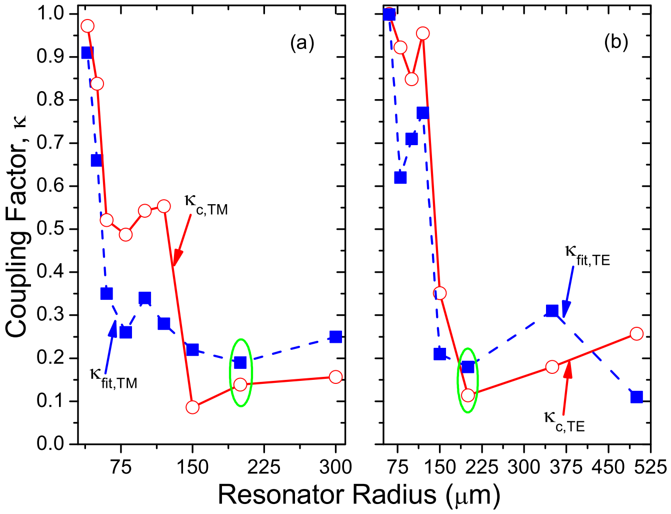

Figure 5.8: The extracted coupling factors from fitting analysis and coupling factors necessary to meet the critical coupling for TM (a) and TE (b) polarizations. The lines are to guide the eye.

excluding submicron Si wire resonators [93, 94]. It is clear that we do not achieve perfect critical coupling which would result in lower than maximum Q-factor [50], while low coupling factor results in low extinction ratio. Our results show that we reach a good compromise between good extinction ratios and high quality factors.

5.2 Compact Racetrack Resonators

The realization of high-Q waveguide resonators were achieved as explained in previous section. However, resonators with radii smaller than 120 μm showed relatively poor characteristics. Therefore, we studied the possibility of fabrication of these compact resonators with better resonance characteristics. For this purpose, very high bending losses for bends of smaller radii had to be reduced. We attained this goal by increasing the rib height of SM waveguide from 0.42 μm to 0.5 μm. The analytic bend loss calculation results show that the bending losses drastically decrease for radii larger than 30 μm and 80 μm for TM and

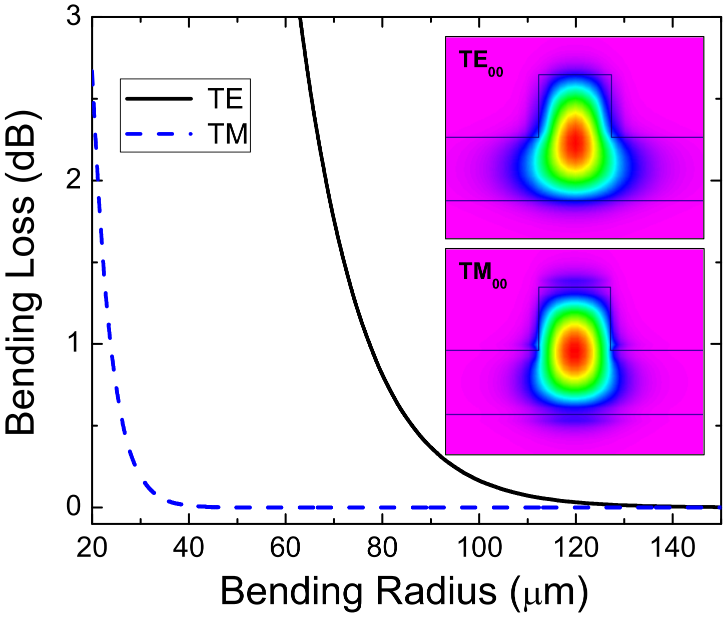

Figure 5.9: Analytically calculated bending loss for a 90° bend as a function of bending radius. The waveguide has dimensions of w and H are 1.0 μm and h is 0.5 μm. The calculated TE and TM mode profiles for the SOI waveguide is also included.

TE modes, respectively (Fig.5.9). The relatively small bending loss for TM when compared to TE is due to stronger lateral confinement of the TM mode. Mode profiles showing this feature can be seen in the inset of the figure. The effective refractive indices are calculated to be 3.3546 and 3.3402 for TE and TM modes, respectively.

A number of resonators of bending radii ranging from 10 μm to 120 μm were characterized for both polarizations. The measured TE and TM transmission spectra are given in Fig.5.10 and Fig.5.11, respectively. The resonance characteristics are summarized in Table.5.5 for TE and in Table.5.6 for TM. The free spectral range of 0.7 nm at 120 μm radius increases to 3.0 nm for 20 μm devices for TM polarization. Resonances for resonators are washed out due to excessive radiation loss with radius of 10 μm or smaller for TM polarization, while this takes place for resonators with radius of 40 μm or smaller for TE polarization.

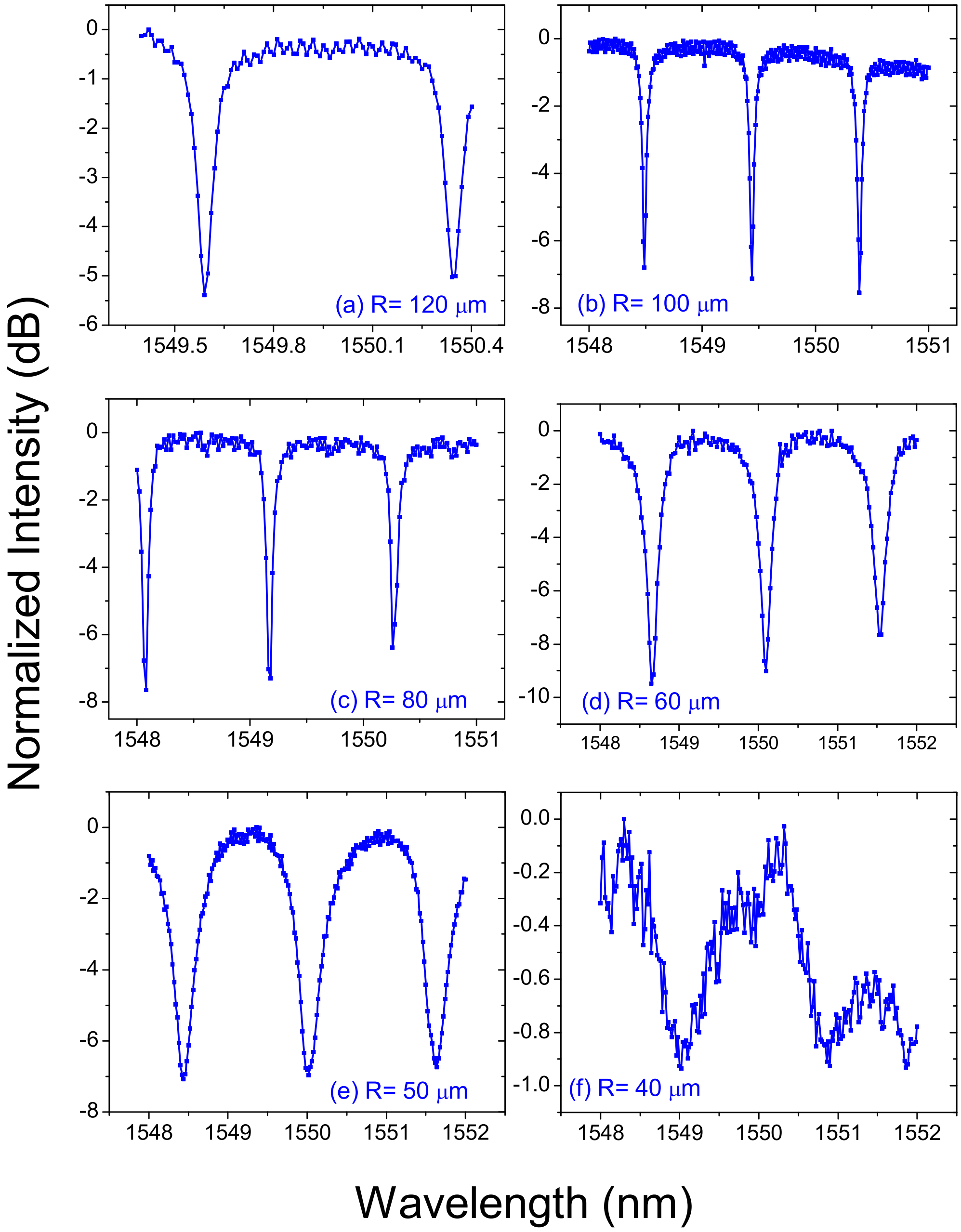

Figure 5.10: Measured TE transmission spectra of the characterized resonators.

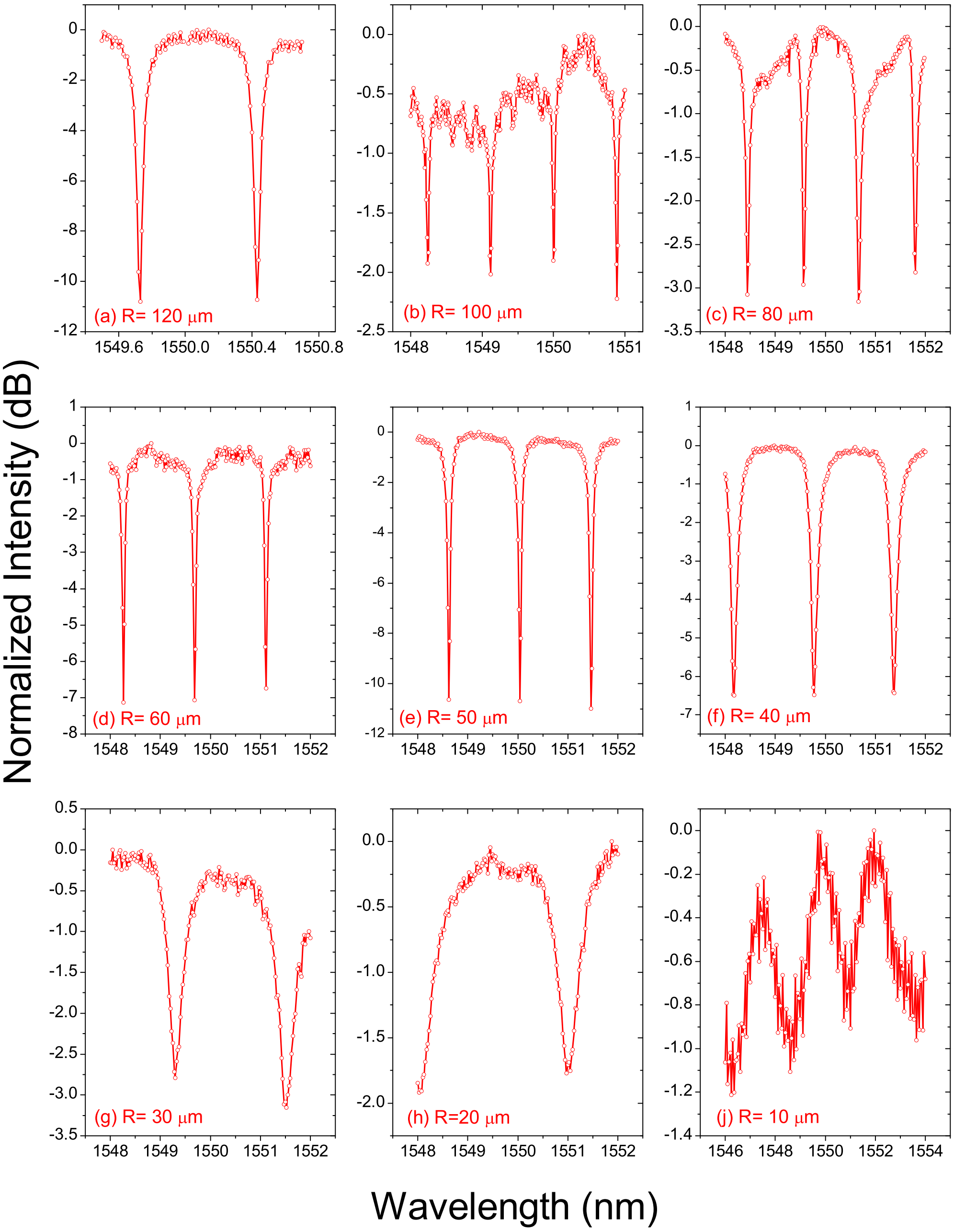

Figure 5.11: Measured TM transmission spectra of the characterized resonators.

R (μm)	L$_c$ (μm)	FSR nm	FWHM pm	Fin.	Q-F.	M.D. (dB)
120	52	0.754	47	16.0	32980	5.4
100	26	0.953	55	17.3	28180	7.0
80	42	1.089	75	14.5	20670	7.6
60	36	1.449	262	5.5	5910	9.5
50	48	1.575	370	4.3	4190	7.2
40	46	1.848	866	2.1	1790	0.9

Table 5.5: Characteristics of resonators for which measured TE spectra are given in Fig.5.10.

R (μm)	L$_c$ (μm)	FSR nm	FWHM pm	Fin.	Q-F.	M.D. (dB)
120	78	0.703	79	8.9	19620	10.8
100	48	0.885	83	10.7	18675	1.5
80	34	1.118	97	11.5	15980	3.2
60	36	1.430	78	18.3	19870	7.2
50	68	1.444	117	12.3	13250	10.7
40	74	1.614	154	10.5	10065	6.5
30	50	2.214	350	6.3	4430	2.8
20	44	2.966	467	6.4	3320	1.8
10	34	2.392	1093	2.2	1420	0.9

Table 5.6: Characteristics of resonators for which measured TM spectra are given in Fig.5.11.

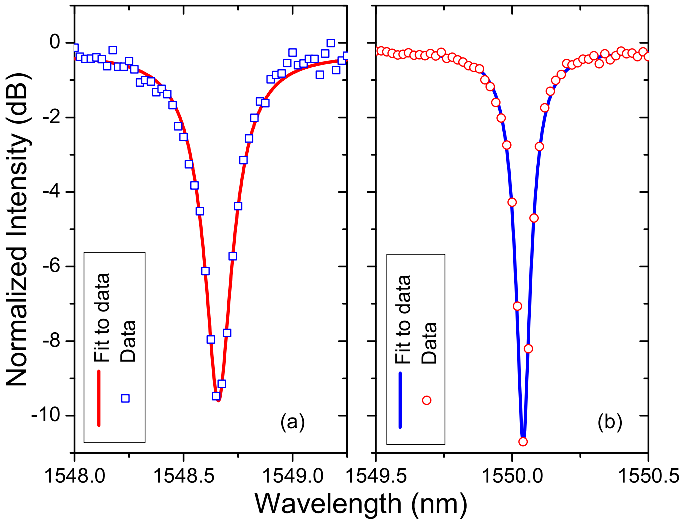

Figure 5.12: (a) Curve fit to measured TE transmission spectra for R=60 μm (b) Curve fit to measured TM transmission spectra for R=50 μm.

Curve fitting method was again applied to the measured spectra to get coupling factors and resonator losses using the method explained in previous section. A pair of examples fitted spectra is given in Fig. 5.12. All the extracted results from the analysis and the BPM calculated coupling factors used for fitting are tabulated in Table 5.7 and Table 5.8 for TE spectra given in Fig. 5.10 and TM spectra given in Fig. 5.11, respectively.

The extracted resonator round trip, effective propagation losses tabulated are

R	L$_c$	g	κ_{BPM-g}	$\kappa_{BPM-g'}$	κ_{fit}	κ_c	$\alpha_{R.T.}$	α
(μm)	(μm)	(μm)					(dB)	(dB/cm)
120	52	0.8	0.06	0.10	0.12	0.35	1.89	22.0
100	26	0.8	0.02	0.04	0.10	0.23	1.16	17.0
80	42	0.8	0.03	0.06	0.13	0.28	1.41	24.0
60	36	0.7	0.05	0.08	0.30	0.52	3.14	70.0
50	48	0.7	0.06	0.12	0.38	0.70	5.29	129.0
40	46	0.8	0.03	0.06	0.10	0.88	9.27	270.0

Table 5.7: Extracted values from curve fitting analysis of resonators for which measured TE spectra are given in Fig.5.10. Results of BPM calculations for coupling factors are also included. ($g' = g - 0.1$ μm)

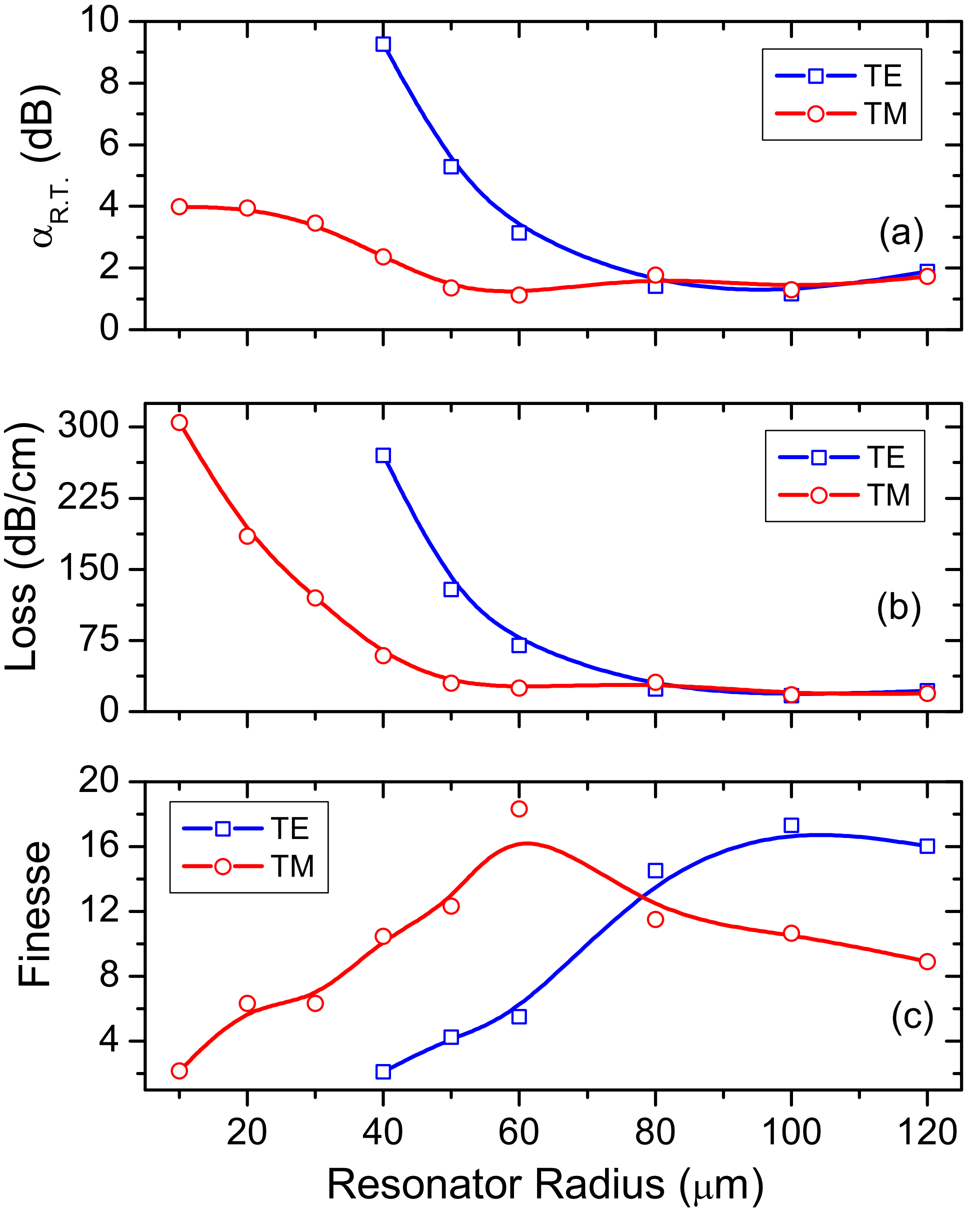

Figure 5.13: (a) Resonator round trip loss (b) effective propagation loss and (c) finesse values for TE and TM polarizations

R (μm)	L$_c$ (μm)	g (μm)	κ_{BPM-g}	$\kappa_{BPM-g'}$	κ_{fit}	κ_c	$\alpha_{R.T.}$ (dB)	α (dB/cm)
120	78	0.7	0.02	0.06	0.20	0.33	1.73	19.0
100	48	0.8	0.01	0.02	0.02	0.26	1.30	18.0
80	34	0.7	0.01	0.02	0.07	0.33	1.77	31.0
60	36	0.7	0.01	0.02	0.09	0.21	1.12	25.0
50	68	0.7	0.02	0.04	0.16	0.27	1.35	30.0
40	74	0.7	0.02	0.05	0.18	0.42	2.36	59.0
30	50	0.7	0.01	0.04	0.12	0.55	3.46	120.0
20	44	0.7	0.01	0.03	0.09	0.60	3.95	185.0
10	34	0.7	0.01	0.02	0.04	0.60	3.99	305.0

Table 5.8: Extracted values from curve fitting analysis of resonators for which measured TM spectra are given in Fig.5.11. Results of BPM calculations for coupling factors are also included.

plotted as a function of resonator radius in Fig. 5.13 (a) and (b). Extracted resonator losses for TM polarization decrease dramatically for resonator of 50 μm radius and follow a horizontal line with increasing resonator radius. However, resonator losses for TE polarization are high for radius smaller than 80 μm. The difference between TE and TM resonator losses of radius smaller than 80 μm seen in Fig. 5.13 (a) and (b) is due to higher bending losses applied to TE mode of the SOI curved waveguide for small radii. This explanation agrees very well with our analytical calculation for bending loss of the SOI waveguide with 0.5 μm rib height given in Fig. 5.9. Furthermore, we plotted measured finesse values for both polarizations in Fig. 5.13 (c). Comparison with resonator round trip loss plot shows that the finesse values increase rapidly as resonator losses decrease. Poor finesse values for TE polarization at smaller radius reach values higher than 15 for radius larger than 80 μm. The decrease in resonator losses shows itself also as increase in Q-factors of the resonators for both polarizations.

In summary to this section, we demonstrated that it is possible to realize SOI rib waveguide based racetrack resonators with radius as small as 20 μm resonating TM polarized light [95]. We also showed TE polarized light resonances in resonators with radius as small as 50 μm. Free spectral ranges of 3.0 nm, finesse values of 18.3 and Q-factors of 32980 have been observed. This more compact SOI resonators can become key components for silicon based integrated optical devices and even can be more easily integrated with MEMS structures (diaphragms and cantilevers etc.) for sensor applications.

5.3 Thermo-optical Tuning of SOI Resonators

Ring resonators are distinguished from other integrated optics components with their high wavelength selectivity, a key issue for many device applications ranging from wavelength multiplexers [45] to modulators [96]. Recently, high-Q resonator based modulators with significantly lower switching powers have become an important alternative to Mach-Zehnder (M-Z) modulators. Ability to tune the output wavelength is the first step to the development of devices for applications such as optical modulators and switches. Wavelength tuning capability is also required to fine tune to the desired wavelength when the target wavelength is not met during the fabrication process due to imperfections or material non-uniformity. Electro-optical [96], thermo-optical [10] and all-optical [97] tuning are the most commonly used mechanisms in device applications. Although electro-optical effect can be implemented for fast tuning and switching on compound semiconductors, due to inversion symmetry crystal silicon lacks an electro optic coefficient and is, therefore does not lend itself to this mechanism. On the other hand, silicon is known for its large thermo-optic coefficient [11]. Use of thermo-optic effect in silicon devices is a simple, straightforward and cost-effective way for applications requiring moderate modulation speeds.

In this section, we concentrate on thermo-optical tuning of high-Q racetrack resonators on SOI rib waveguide of 1 μm size and their operations as low-power optical switch.

Fig. 5.14 (a) shows schematic top view of the designed SOI resonator with the metal heater and contact pads. Cross-sectional detail of the SOI waveguide is shown in Fig. 5.14 (b). This SOI waveguide geometry optimized by beam propagation method simulations have been experimentally proved to be single mode. These low loss single mode rib waveguides have already been used in the

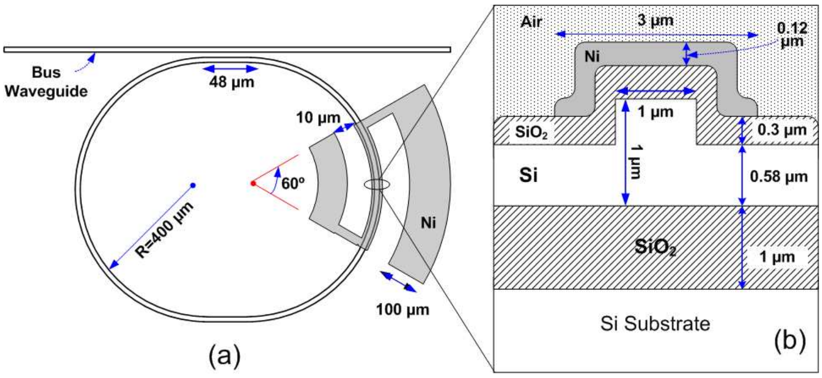

Figure 5.14: Schematic views showing critical dimensions. (a) Top view of the SOI resonator and (b) cross-sectional view of SOI rib waveguide.

demonstration of polarization splitters and high-Q racetrack resonators [68, 94].

All pattern definitions throughout the fabrication of SOI resonators and their thermo-optical tuning elements were done with optical photolithography. Resonator patterns were defined on an SOI wafer which had a 1.00 μm top Si and a 1.00 μm oxide layers on a 625 μm thick substrate. The patterns were transferred to silicon layer by an amount of 0.42 μm using an RIE process resulting in smooth sidewalls [94]. The etch was followed by deposition of about 0.3 μm SiO_2 passivation layer on the wafer using plasma enhanced chemical vapor deposition at 250 C°. The 0.12 μm thick nickel heaters and contact pads were then defined through a process sequence comprising photolithography, metal sputtering and lift-off steps. The optical micrographs of a finished resonator and its overlaying metal heater are shown in Fig. 5.15.

We cleaved the wafer to a chip of 8 mm length. The measured transmission spectrum of the resonator with radius of 400 μm, straight coupling section of 48 μm and coupling gap of 0.8 μm is given in Fig. 5.16. The simulated spectrum of the resonator using Eq.4.12 is also plotted in the figure. We used BPM calculated coupling factors as initial values in the simulation. After a few iterations coupling factor of 0.45 and resonator loss of 1.57 dB was obtained. This is to be expected since we have already shown in [94] that SOI rib bend waveguides with radius of

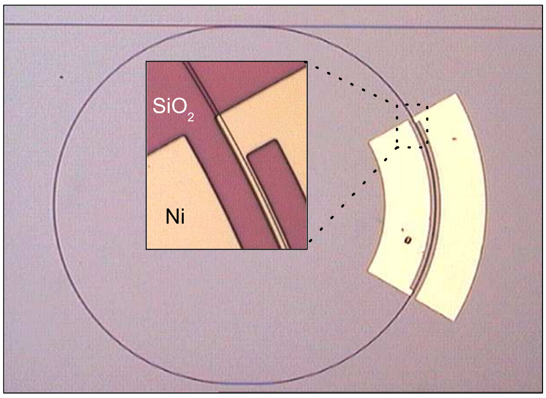

Figure 5.15: (a) Optical micrographs showing top view of a fabricated racetrack resonator and overlaying metal heater.

300 μm or larger do not suffer from radiation loss due to curvature. Scattering from imperfections due to fabrication is estimated to be the source of the resonator loss. The free spectral range can be determined to be 248 pm from the figure. The resonator shows a good modulation depth of larger than 11 dB. The full width at half maximum (bandwidth) can be extracted from the curve fit to be 40 pm. Using this value with resonance wavelength and free spectral range of the resonator, we calculated a Q-factor of 38000 and a finesse value of 6.2.

The resonance wavelengths of a resonator are determined through the phase term, ϕ of Eq. 4.12 and can be tuned by either changing the resonator circumference, L or the effective index, n_e. Silicon is known for its large thermo-optical coefficient of $1.84x10^{-4}1/C^{\circ}$ which have been employed to realize modulators on SOI wafers [11]. Thermo-optical modulation of effective refractive index is attained by placing a metal heater electrode near the waveguide. High-Q resonators have narrow bandwidths and can be tuned to off-resonance with lower electrical powers [10]. After passive characterization of the resonator, we applied electrical power to the contact pads using micro-probes. The heater is a 0.12 μm thick and 3 μm wide nickel layer in the shape of a circular bend to assure maximum overlapping of heat flow with optical field in the resonator. It is just above the rib of the waveguide with only a 0.3 μm thick SiO_2 in between (Fig. 5.14 (b)). The

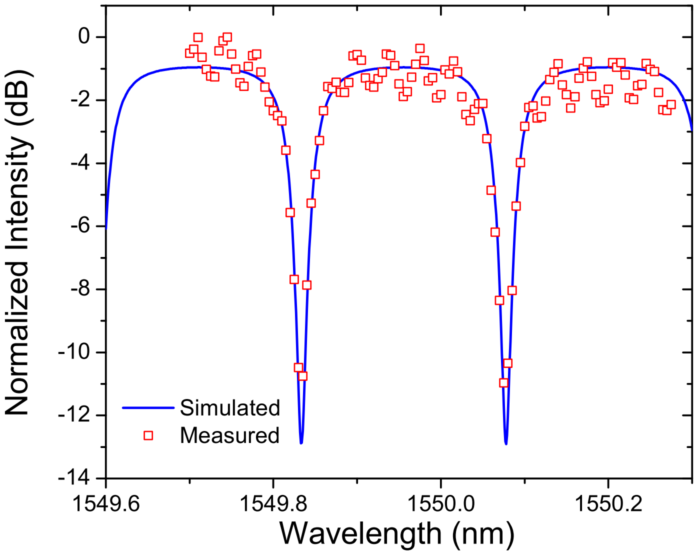

Figure 5.16: Measured and simulated TE transmission spectrum of the fabricated SOI rib waveguide racetrack resonator.

bend shaped heater spans an angle of 60°. The 100 μm wide nickel contact pads were also designed in circular shape. They are well separated from the heater (Fig. 5.14(a) and Fig. 5.15). The pads and heater combination was measured to have a resistance of 170 Ωs. The measured transmission spectra of the resonator under applied power are shown for four different applied power values in Fig. 5.17(a). There is an obvious tuning of resonance wavelength with applied power. We also plot the resonance wavelength shift as a function of applied electrical power in Fig. 5.17(b). It can be deduced from the figure that a total of 57 mW of electrical power is sufficient to scan the resonator over its full free spectral range.

In order to relate the effective index change, Δn_{eff} required to shift a specific resonance by $\Delta\lambda$ the following argument can employed. The resonance condition requires that the round trip phase, ϕ should be an integer multiple of 2π, that is

$$\phi = (2\pi/\lambda_0)n_{eff}L = m2\pi \tag{5.1}$$

If the effective index changes so does the resonance wavelength. If we follow the same resonance m does not change. Therefore for two different effective indices

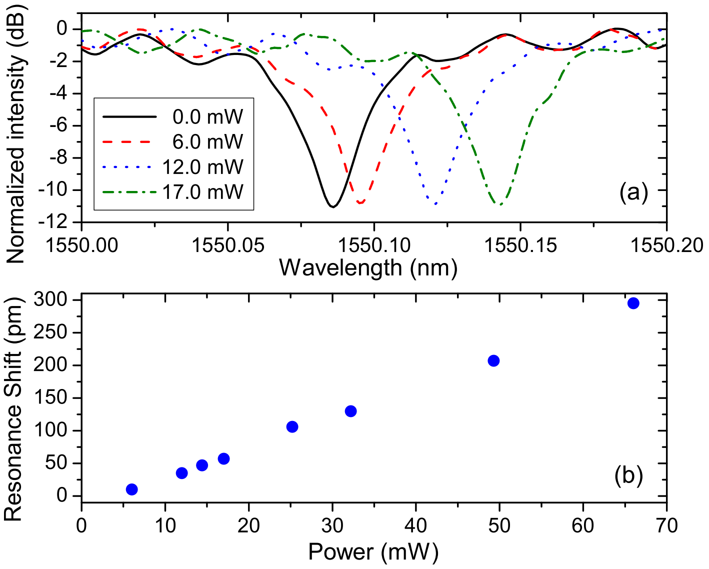

Figure 5.17: (a) Measured TE transmission spectrum as electrical power applied to the metal heater. (b) Shift in resonance wavelength as a function of applied power.

we get two different resonance wavelengths such that

$$m2\pi = (2\pi/\lambda_0)n_{eff}L = (2\pi/\lambda_0^{'})n_{eff}^{'}L \tag{5.2}$$

This equation can be rewritten as

$$2\pi\ L(\frac{n_{eff}}{\lambda_0} - \frac{n_{eff}^{'}}{\lambda_0^{'}}) = 0 \tag{5.3}$$

which leads to

$$n_{eff}\lambda_0^{'} = n_{eff}^{'}\lambda_0 \tag{5.4}$$

One can define $\lambda_0^{'} = \lambda_0 + \Delta\lambda$ and $n_{eff}^{'} = n_{eff} + \Delta n_{eff}$ so that

$$n_{eff}(\lambda_0 + \Delta\lambda) = (n_{eff} + \Delta n_{eff})\lambda_0 \tag{5.5}$$

or

$$\Delta n_{eff} = (\Delta\lambda/\lambda_0)n_{eff} \tag{5.6}$$

If we set $\Delta\lambda = FWHM$, we get

$$\Delta n_{eff} = (FWHM/\lambda_0)n_{eff} = n_{eff}/Q \tag{5.7}$$

where Q is the Q-factor of the resonator. This equation suggests that the required effective index change for a FWHM shift in a resonance is inversely proportional to Q-factor. This relation explains why higher Q-factors lead to lower tuning and switching powers.

In our case, the heater does not have the same length as circumference of resonator, L. Therefore we should modify Eq. 5.7, by defining $L = L_1 + L_H$. We can start with rewriting Eq. 5.2 as

$$m2\pi = (2\pi/\lambda_0)n_{eff}L_1 + (2\pi/\lambda_0)n_{eff}L_H = (2\pi/\lambda_0)n_{eff}L_1 + (2\pi/\lambda_0^{'})n_{eff}^{'}L_H \quad (5.8)$$

which simplifies to

$$n_{eff}L_1(\frac{1}{\lambda_0} - \frac{1}{\lambda_0^{'}}) = L_{1H}(\frac{n_{eff}^{'}}{\lambda_0^{'}} - \frac{n_{eff}}{\lambda_0}) \quad (5.9)$$

This equation can even be more simplified when $\lambda_0^{'} = \lambda_0 + \Delta\lambda$ and $n_{eff}^{'} = n_{eff} + \Delta n_{eff}$ are introduced. The resulting equation relating change in effective index to the measured change in resonance wavelength for our case is

$$\Delta n_{eff} = (\Delta\lambda/\lambda_0)n_{eff}(L/L_H) \quad (5.10)$$

From Fig. 5.17(b), we find that, 17 mW of electrical power resulting in a shift of 57 pm in the spectrum is sufficient to switch the resonator from OFF (at resonance wavelength) to ON (at off-resonance wavelengths) state. Substituting n$_{eff}$=3.3637 in Eq. 5.10, Δn_{eff}=7.71x10^{-4} is calculated for switching from OFF to ON state at a given wavelength. We can express $\Delta n_{eff} = (dn_{eff}/dT)\Delta T$. Although, dn$_{eff}/dT$ is a waveguide-geometry dependent term, we can calculate the minimum change in local temperature to be 4.19 C° by approximating dn$_{eff}$/dT $\simeq$ (dn/dT)$_{Si}$.

To observe the frequency response of the switch, applied power was modulated by a small signal sinusoidal driving voltage. The optical signal was monitored with an InGaAs photodetector of 70 MHz bandwidth. Normalized modulation depth versus driving voltage frequency for the switch is plotted in Fig. 5.18. A relatively high 3 dB cutoff frequency of 210 kHz was found for the device. To the best of our knowledge, this device is the fastest SOI thermo-optical switch up to date with no differential control [98, 37, 99].

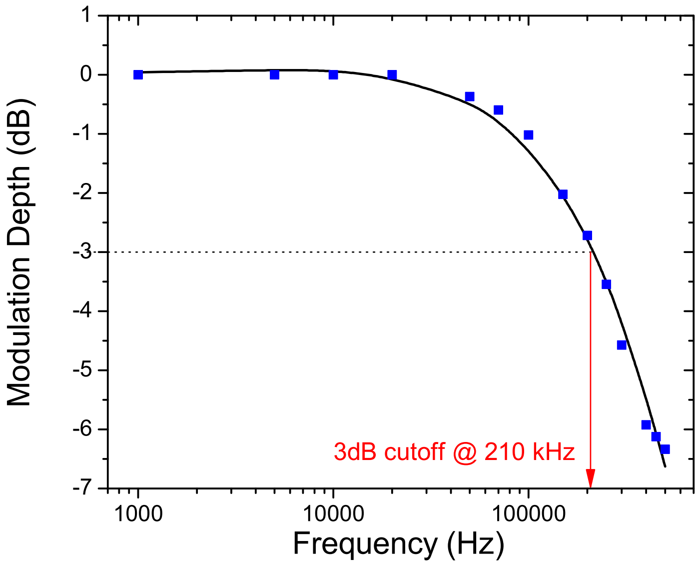

Figure 5.18: Measured modulation response to frequency change of a small-signal sinusoidal driving voltage.

As a summary to the current section, a silicon-on-insulator optical rib waveguide resonator is fabricated through single etch step and characterized to show high Q-factor of 38000. This resonator shows thermo-optical tunability and operates as a wavelength selective optical switch with low-power consumption of 17 mW. The device was tested to function as a switch at frequencies up to 210 kHz.

5.4 Asymmetrically Coupled SOI Resonators as Add/Drop Filters

So far, we gave results on single bus SOI resonators. Double bus resonators with its additional drop port have some important differences. These resonators can function as wavelength add and drop filters in addition to all properties of single bus resonators. We have designed a set of double bus resonators as discussed

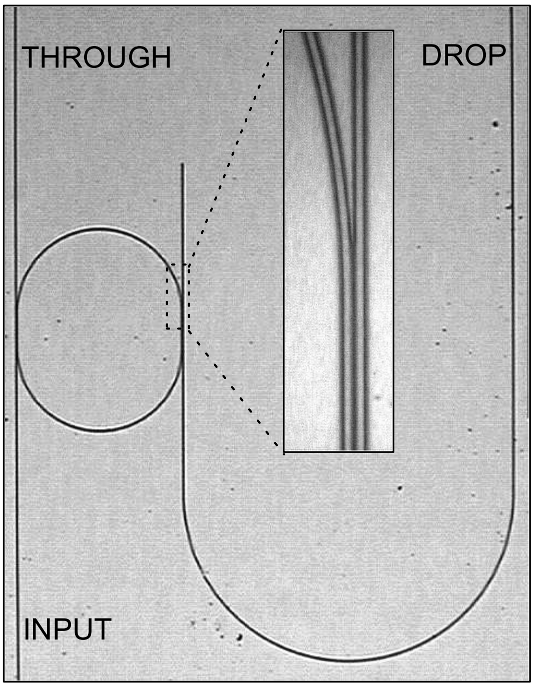

Figure 5.19: Optical micrograph of one of the fabricated add/drop filter. Inset shows the coupling region.

in previous chapter. These are designed as asymmetrically coupled resonators in order to get better filter characteristics [100]. The fabrication of these resonator has no difference with respect to single bus ones. Optical micrograph of one of the fabricated resonator are shown in Fig. 5.19. The output light at both through and drop ports of resonator are monitored with a photodetector separately.

We characterized a number of resonators with both TE and TM polarized light at input ports. The optical intensity at drop ports are normalized with respect to intensity at through ports. Transmission and drop spectra for TE polarization of characterized resonators are shown in Fig.5.20. Small amplitude oscillations due to Fabry-Perot resonances between the ends of the straight bus waveguide are observed even for drop spectra. The measured spectra for TM polarized light from through and drop ports of the resonator with R=200 μm and L_c=74 μm is also given in Fig.5.21. The geometrical and spectral characteristics of the double

R (μm)	L_c (μm)	g_1 (μm)	g_2 (μm)	FSR (nm)	FWHM (pm)	Fin.	Q-F.	M.D. thr(dB)	M.D. drp(dB)	C.Talk. (dB)
150	64	0.8	0.9	0.607	148	4.1	10470	10.2	5.6	
200	72	0.7	0.9	0.461	88	5.2	17610	2.4	11.6	-3
200	48	0.8	0.9	0.468	81	5.2	19130	12.3	12.1	-10
250	42	0.8	0.9	0.389	56	6.9	27680	5.0	5.2	
400	30	0.8	1.0	0.250	30	8.3	51660	5.9	6.7	
500	46	0.8	1.0	0.210	30	7.8	51660	8.2	11.1	-2.2
200	72	0.7	0.9	0.467	118	4.0	13130	6.8	8.8	-7.5

Table 5.9: Characteristics of add/drop filters for which measured TE spectra are given in Fig.5.20. Results for the filter TM spectra of which is shown in Fig. 5.21 is also included at the last row of the table.

bus resonators shown in Fig.5.20 and 5.21 are tabulated for convenience in Table 5.9.

A better understanding of the filter characteristics can obtained through analyzing the spectra by curve fitting the measured responses to the expected responses given in Eq. 4.15 and Eq. 4.17. As representative examples, we applied this analysis two filters that were shown in Fig. 5.20 (c) and (f) with radii of 200 and 500 μm respectively. The filters are referred as filter 1 and filter 2 in the rest of this section. Such an analysis yields coupling factors and resonator loss values, as observed in previous sections. Coupling factors numerically calculated using BPM were used as starting values for curve fitting. The results of the measurements as well as the fit curves using the design equations are given in Fig. 5.22. We give coupling factors and resonator losses extracted from this analysis in Table 5.10. Results of BPM calculations using the designed coupling gaps are also included for comparison. The results displayed in the table suggests that simulated and extracted coupling coefficients for 1 and 0.9 μm gap are very close. However, the difference between simulated and extracted coefficients increase for gaps of 0.8 μm. To understand this difference we performed BPM simulations for coupling gaps narrower than the design values by 0.1 μm, which showed much better agreement with the extracted values. This suggests that the fabrication procedure leads to narrower gaps than expected as the gaps get smaller.

Greater resonator loss for filter 1 is estimated to be mostly due to higher

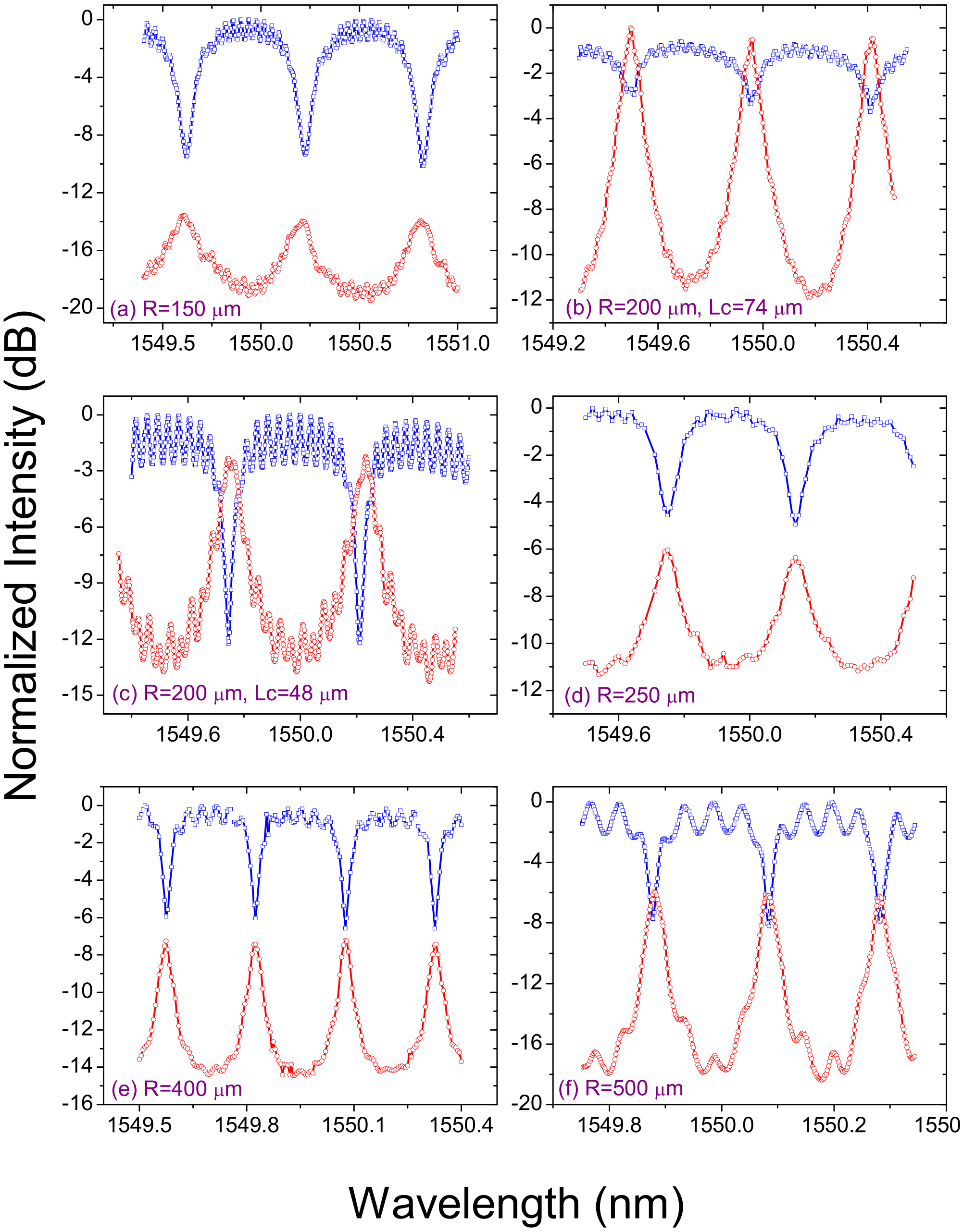

Figure 5.20: Measured TE transmission and drop spectra of the characterized double bus resonators.

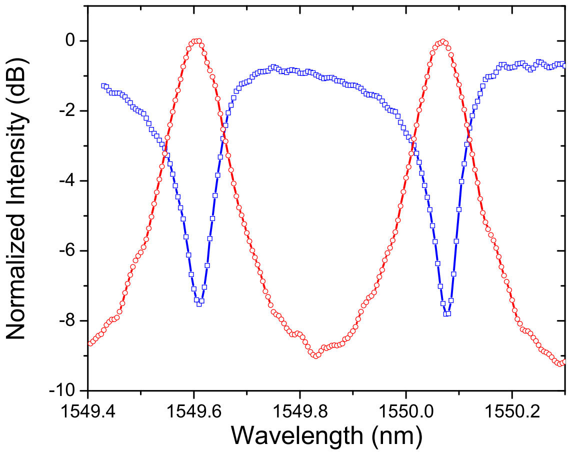

Figure 5.21: Measured TM transmission and drop spectra of the double bus resonator with R=200 μm and L_c=72 μm.

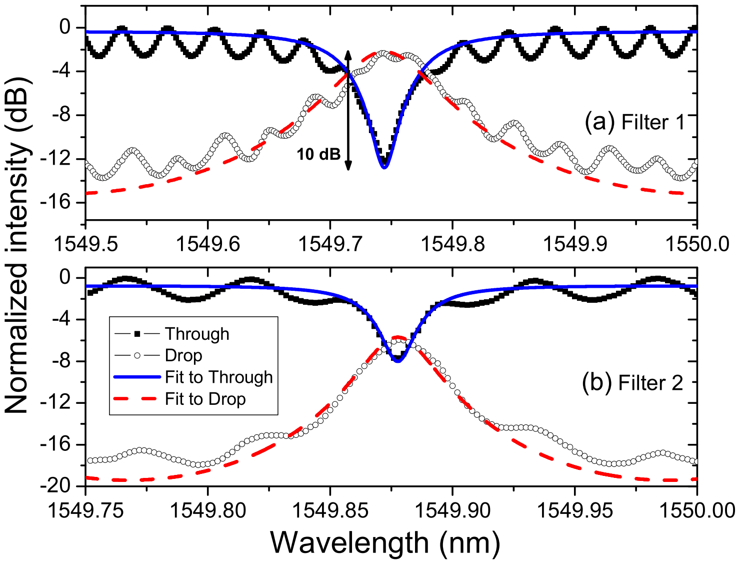

Figure 5.22: Fit to the measured transmission and drop spectra about (a) λ_0=1549.773 nm for R=200 μm and (b) λ_0=1549.878 nm for R=500 μm using the analytic functions in Eq.3 and Eq.4.

	$\kappa_{1-extracted}$	κ_{1-BPM}	$\kappa_{2-extracted}$	κ_{2-BPM}	$\alpha_{R.T.}$ (dB)
Filter 1	0.43	0.25	0.20	0.17	0.54
Filter 2	0.45	0.35	0.17	0.15	0.23

Table 5.10: Coupling factors which are numerically (BPM) calculated and extracted from fit to measured data (Fig. 5.22)

radiation loss for 200 μm. Scattering loss should also have a considerable contribution to round trip loss of filter 1 because the propagating light in the resonator is affected by waveguide sidewall roughness more as the waveguide curvature decreases. In the light of the fitting analysis and critical coupling condition, we should note that resonator losses were overestimated for both device in the filter design. The analytical model that we used for calculation of radiation loss may not be precise enough, but its simplicity makes it a very useful tool for the design of waveguide resonators. The crosstalk was determined to be -10.0 dB for filter 1 and -1.9 dB for filter 2. The better crosstalk of filter 1 shows that it is much closer to critical coupling. We verified this conclusion by substituting extracted filter characteristics into the critical coupling relation. Even more reduced crosstalks can be achieved with a better fulfillment of the critical coupling condition. This can be achieved with larger κ_2 (a narrower gap) for both filters. Crosstalk of a filter shows separation level of ports of the filter.

In summary to this section, wavelength add/drop filters based on asymmetrically coupled silicon-on-insulator high-Q racetrack resonators are fabricated, characterized and analyzed. The resonators are realized using single mode large cross-section SOI rib waveguides having bending radii ranging from 150 to 500 μm. The resulting filters show Q-factors as high as 51000 and relatively low crosstalks of -10.0 dB which can be reduced even further by a better match of critical coupling condition [101].

Chapter 6

Hybrid and Layer Transferred SOI Devices

We discuss the use of a layer transfer method for SOI wafers and a set of devices realized with this method in this chapter. First, the transfer of SM SOI waveguides is studied in the first section. Then in the second section, the method is applied to SOI M-Z interferometers to test the method further. Finally, asymmetric vertical couplers (AVC) and their realization using a hybrid technology is discussed.

6.1 Layer Transferred SOI Waveguides

In this section, the feasibility of the silicon layer transfer process of SOI for integrated optical purposes is tested. Two waveguide chips were prepared. Layer transfer process is applied to one of the chip, while the other is labelled as conventional and used for comparison purposes.

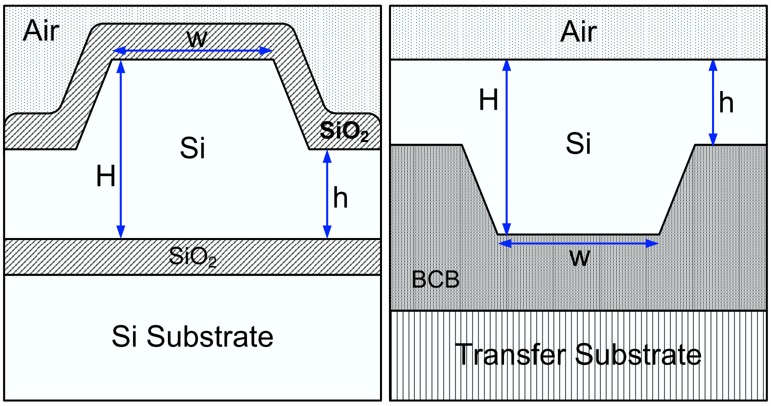

(a) (b)

Figure 6.1: Cross-sectional schematic view for (a) conventional SOI waveguide (b) Si-polymer waveguide

6.1.1 Waveguide Fabrication and Si Layer Transfer

The optical waveguides reported in this section (Fig. 6.1) were fabricated on a SOI wafer with silicon layer thickness, H, of 5 μm and buried oxide layer thickness of 1 μm. Waveguides are designed to be single mode with a width, w, of 5 μm and slab height, h, of 2.5 μm. The initial fabrication process is the same for both conventional and substrate removed waveguides. We cleave two pieces with dimensions of about 1.5 cm x 1.5 cm from the SOI wafer. The term conventional is used in the text for no applied substrate remove process. After the samples are degreased by three solvent cleaning process a 2000 Si_3N_4 layer is deposited using plasma enhanced chemical vapor deposition (PECVD) at 250 °C. Photoresist is used as the mask during optical lithography (PL2) defining the waveguide patterns which are then transferred to the Si_3N_4 layer by a dilute HF etch. After removing the photoresist mask in acetone, the samples become ready for wet chemical etching in 33 percent potassium hydroxide (KOH) at 40 °C. We add isopropyl alcohol to the solution to get smoother side walls at a ratio of 1:3 [54]. After the KOH etch, fabrication of conventional SOI waveguides is finalized by the deposition of a 1 μm upper cladding layer of PECVD grown SiO_2, whereas, the fabrication process for the waveguide sample to be transferred continues. The SEM micrographs of fabricated SOI waveguides is given in Fig. 6.2.

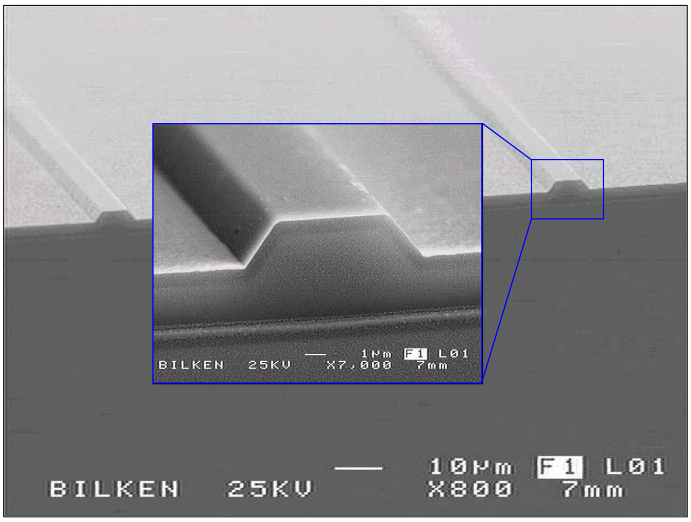

Figure 6.2: Sem images of KOH fabricated conventional SOI single mode large cross-section waveguides. The detailed inset image shows the smooth side walls and deposited SiO_2 layer.

A piece of silicon wafer slightly larger than that of the waveguide, which is to be used as transfer substrate, and the sample with the waveguides are both deposited with a very thin (about 500 $\mathring{A}$) PECVD oxide layer at 250 °C. This oxide layer promotes adhesion between silicon and benzocyclobutane (BCB) polymer. First, BCB polymer is spun onto the waveguide sample and left in an oven at 210 °C under nitrogen environment until the polymer is partially cured, which takes about 30 minutes. This first polymer spin is done to planarize the sample surface. The edge accumulation of the polymer on the planarized sample during spin process is removed by cleaving the edges of the wafer. This is followed by coating the transfer substrate also with BCB and placing it on a hot plate set at 165 °C. The polymer shows low viscosity and flows at this temperature. The planarized waveguide sample is placed on the transfer substrate with the waveguides facing the polymer surface. The sample can be easily moved on the transfer substrate to align the crystallographic axes of the two substrates. The resulting stack is put into the oven at 250 °C for 2 hours under nitrogen atmosphere to fully cure the BCB [102].

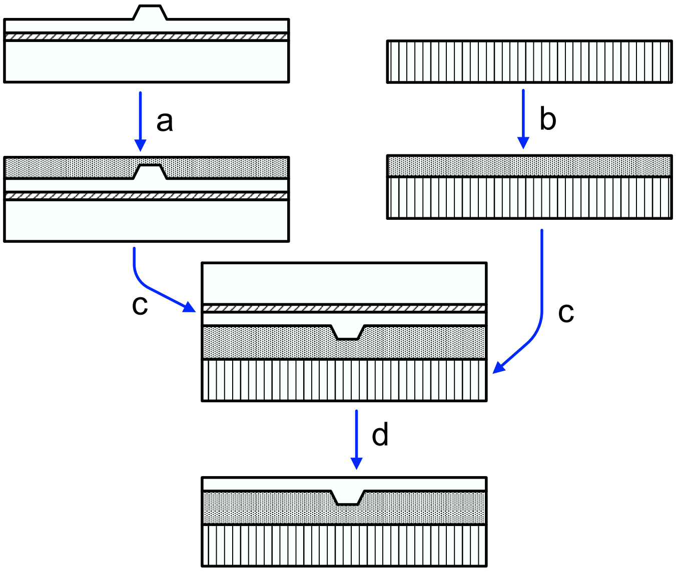

Figure 6.3: Schematic representation of the layer transfer process. a) Planarization of waveguide sample with partially cured BCB. b) BCB coating of transfer substrate. c) Stacking of waveguide sample and transfer substrate with full cure of BCB. d) Substrate and oxide removal for waveguide sample.

After the full cure, the stack is bonded to a handle wafer and all surfaces of the stack except the backside of the waveguide sample are covered with blackwax. The new stack is placed in a KOH solution at a ratio of 1:3 at 50 °C and left there until the Si substrate of the waveguide sample is totally etched away. Buried oxide layer acts as an etch stop layer and is removed after the KOH etch by a dilute HF solution. The silicon layer transfer is schematically summarized in Fig. 6.3. A polished flat silicon surface remains after oxide removal. After cleaning the blackwax and detaching the handle substrate, fabrication of the Si-polymer waveguides is over.

6.1.2 Waveguide Characterization

Both the conventional and the substrate removed (Si-polymer) waveguides are optically cleaved and analyzed on an optical test setup using an external cavity tuneable laser. The input light polarization state is controlled by a fibre polarization controller. TE and TM measurements are made separately. Near field

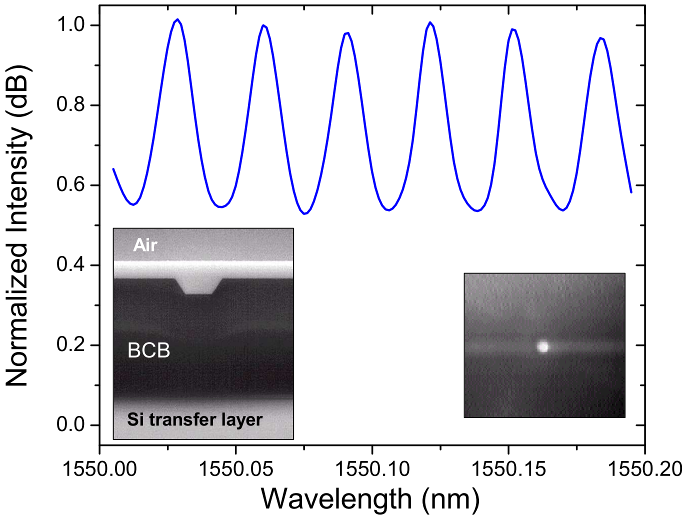

Figure 6.4: A representative Fabry-Perot oscillation. Insets show a SEM view of Si-polymer waveguide facet and a far field image of Si-polymer waveguide mode.

image of guided modes are viewed on an IR camera. We tested the waveguides for single mode guiding and conclude that both waveguides are single mode. The waveguides are then tested for their propagation losses and compared. For this purpose, we employ the Fabry-Perot interference method. The light at output waveguide facet is monitored with a Ge photodetector. The wavelength of the input light is scanned over a 1nm range around 1550 nm in steps of 5 pm. This measurement process is performed for both polarization states. The output power through the waveguide is plotted as a function of wavelength. These plots show Fabry-Perot oscillations (Fig. 6.4). Using the minima and maxima of the oscillations with the reflectivity of Si, the propagation losses are calculated for both TE and TM polarizations. The calculated average TE and TM propagation losses for both the conventional SOI waveguides and the Si-polymer waveguides are given in Table 6.1. Higher than expected losses are due to assumption of perfect facets, which is very hard to get for silicon waveguides of this thickness [103] by cleaving. In this study, we emphasize the comparison of losses between the conventional waveguides and the transferred rather than the absolute values which can be improved by chemo-mechanical polishing.

	TE Propagation Loss (dB/cm)	TM Propagation Loss (dB/cm))
SOI Waveguides	3.6 ± 1.1	3.5 ± 1.2
Si-Polymer Waveguides	3.9 ± 1.2	3.9 ± 1.7

Table 6.1: Measured TE and TM propagation losses for SOI and Si-polymer waveguide.

The comparison of modal and loss characteristics of the both waveguides clearly proves the feasibility of the silicon layer transfer process of SOI for integrated optical purposes. The use of a polymer as the bonding agent makes the bonding of a processed (i.e. having thickness variations) surface to another wafer possible by planarizing it. Finally, this process prepares the backsides of the waveguides for further processing. The quality of the backside surface is so high that many micro fabrication processes including photolithography, metallization and etching, can easily be performed. We believe that such a layer transfer process is a promising way of high-level hybrid integration of waveguide devices.

6.2 Layer Transferred Mach-Zehnder Thermooptic Modulator

In this section we further test the layer transfer method by applying on a Mach-Zehnder (M-Z) modulator fabricated on a chip of 30x20 mm. This process is very difficult when compared to what was done with straight waveguides. The M-Z had thin metal layers of 20 μm wide, which makes the layer transfer more challenging.

There have been a lot of research to develop thermooptic modulators and switches on SOI platform. This is mainly due to lack of electrooptic effect in Si. Additionally, large thermooptic coefficient of silicon makes realization of cost-effective modulators operating on SOI posiible. The devices realized operated with switching powers on the order of a few hundred mW depending on device

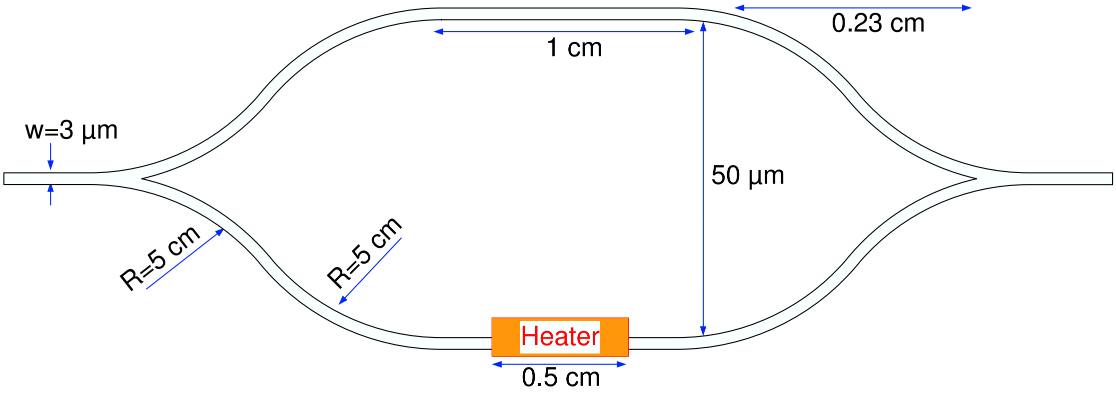

Figure 6.5: Schematic top view of a M-Z modulator. The dimensions are for the structure used in fabrication.

and heater length. Apart from being an extreme demonstration of layer transfer method, we expect that use of layer transfer method on SOI M-Z modulators should decrease the switching powers drastically.

6.2.1 Modulator Design

Waveguide M-Z interferometer is one of the basic integrated optic devices. The device has a junction that equally separates the input light into two arms. These are called 3-dB junctions. A top view of an M-Z interferometer with a Y-junction is given in Fig. 6.5. The geometrical dimensions shown in the figure is those of the modulator that we used in fabrication. This was an already available modulator mask. We thank Nadir Dagli for providing us with that mask. The Y-junction section has s-bends having radius of 5 cm and the M-Z arms are separated from each other by 50 μm. These arms combine on a second junction. The light signals at the arms interfere at the second junction. Phase of one or both the signals can be altered through physical mechanisms such as thermooptic effect. Therefore the output light shows an interferometric feature. The time dependence of input field can be given by

$$E_{in} = E_0 \cos(\omega t) \tag{6.1}$$

where ω is defined as $2\pi c/\lambda$ in terms of free space wavelength. The optical field at each arm is $E_{in}/2$. If phase of one of the arms is changed by an amount of $\Delta\phi$, the electric field at the output port becomes

$$E_{out} = \frac{E_0}{2}[\cos(\omega t + \Delta\phi) + \cos(\omega t)] \tag{6.2}$$

Then, the optical intensity at the output becomes

$$I_{out} = |E_{out}|^2 = E_0^2 \cos^2(\Delta\phi) = I_0 \cos^2(\Delta\phi) \tag{6.3}$$

The optical intensity changes sinusoidally between a maximum and a minimum, if the phase difference changes continuously. Therefore, M-Z interferometers can be used as modulators or optical switches. The phase difference in a M-Z arm is obtained through the use of a physical effect to locally change the effective refractive index of the waveguide mode. The effects mostly used are electrooptic and thermooptic as we discussed in the previous chapter. Here, we concentrate on the use of thermooptic effect to modulate a M-Z interferometer. To employ this effect, a thin metal heater of length L_H is placed on one arm of the interferometer. The phase change corresponding to the change (Δn_{eff}) in effective index is defined as

$$\Delta\phi = (2\pi/\lambda_0)\Delta n_{eff} L_H \tag{6.4}$$

In this equation, Δn_{eff} is given as $dn_{eff}/dT\Delta T$ in terms of thermooptical coefficient of the material and the change in local temperature.

6.2.2 Fabrication and Results

The M-Z modulators were fabricated on the same SOI wafers used in previous section (Si-polymer waveguides). We used an RIE process to define ribs on the wafer instead of anisotropic KOH etching. This is due to S-bends used in M-Z design. Nickel was used as a mask in the etch process. The Ni M-Z waveguide interferometer patterns were formed on the wafer using an image reversal photolithography (PL3) followed by Ni sputter and lift-off processes. An amount of 2.35 μm was etched on the top silicon layer using SF_6 and O_2 gases (RIE2). This is followed by a PECVD growth to deposit 0.3 μm SiO_2 passivation layer on the etched patterns. The Ni heaters and connections to contact pads were formed with another Ni sputtering and liftoff after the second photolithographic step.

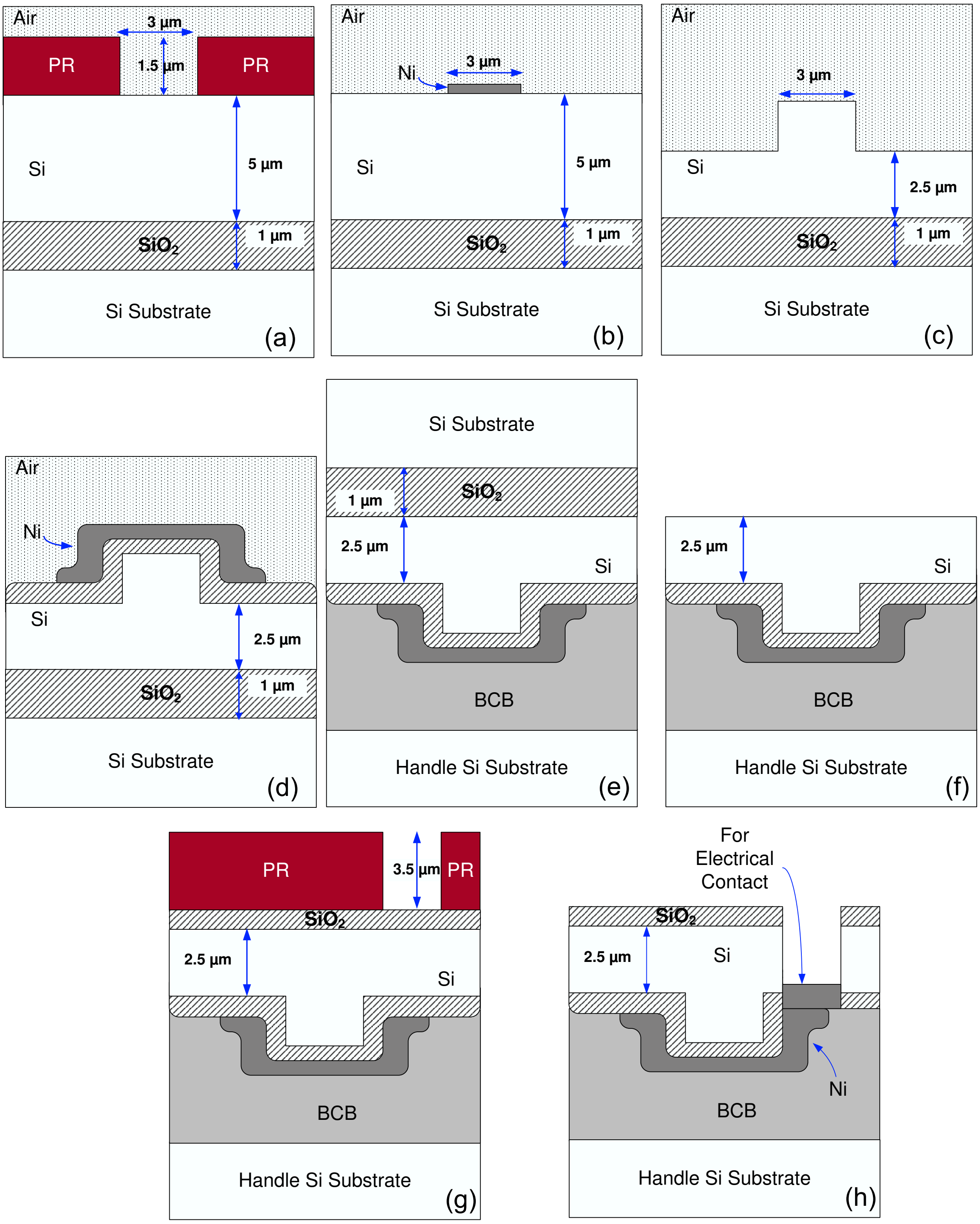

Figure 6.6: Schematic fabrication steps of layer transferred SOI M-Z modulator.

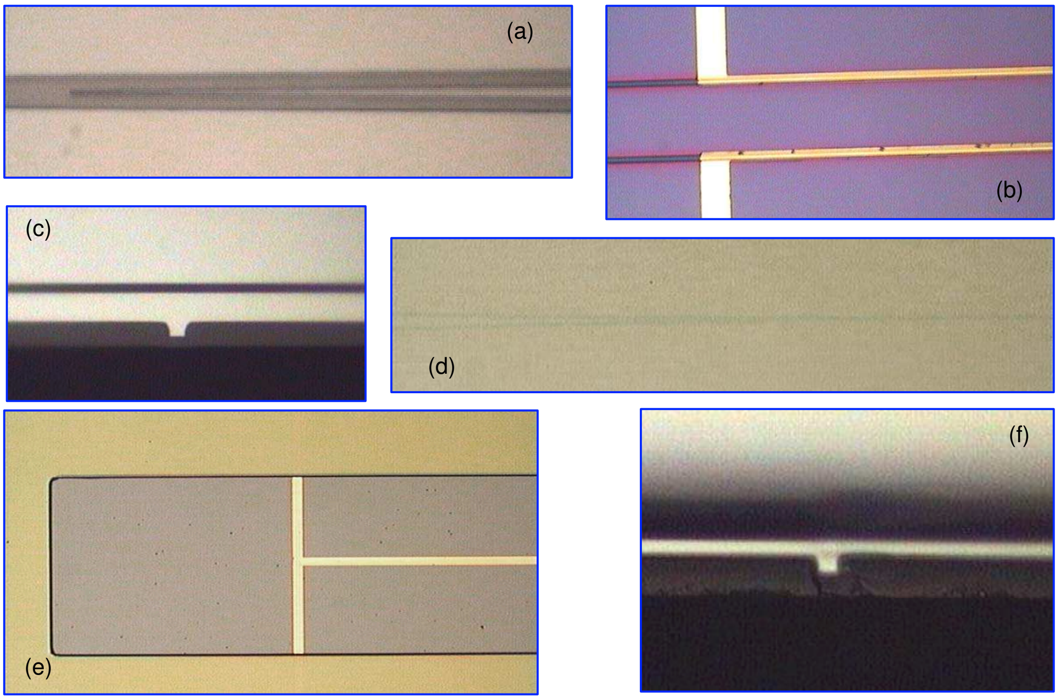

Figure 6.7: Optical micrographies taken during the fabrication of M-Z modulator:(a)Y-junction after first photolithography (b) Ni heaters defined on each arm (c) After planarization using BCB (d) Y-junction seen from backside after layer transfer. (e) Openings for electrical contact (f) Input waveguide facet after cleavage.

The substrate removal process is the same as explained in the previous section. After 525 μm thick substrate was removed, another 0.3 μm SiO_2 layer was deposited on the newly revealed backside of the top silicon layer. Large rectangular holes were opened on the backside to form pads and connect them to previously fabricated heaters. This process was done by successive RIE etches of a SiO_2 (RIE4), a Si (RIE3) and another SiO_2 (RIE4) layer after a third photolithography (PL5). During, this process trenches of 10 μm wide were also opened between arms of M-Z structures. A final photolithography (PL2) and metal sputtering steps were performed to form Ni contact pads and finalized the fabrication of substrate removed SOI M-Z modulators. The fabrication steps are schematically summarized in Fig. 6.6. The optical microscope photos taken during the fabrication process are given in Fig. 6.7.

The fabricated chip was cleaved and mounted on the experimental setup.

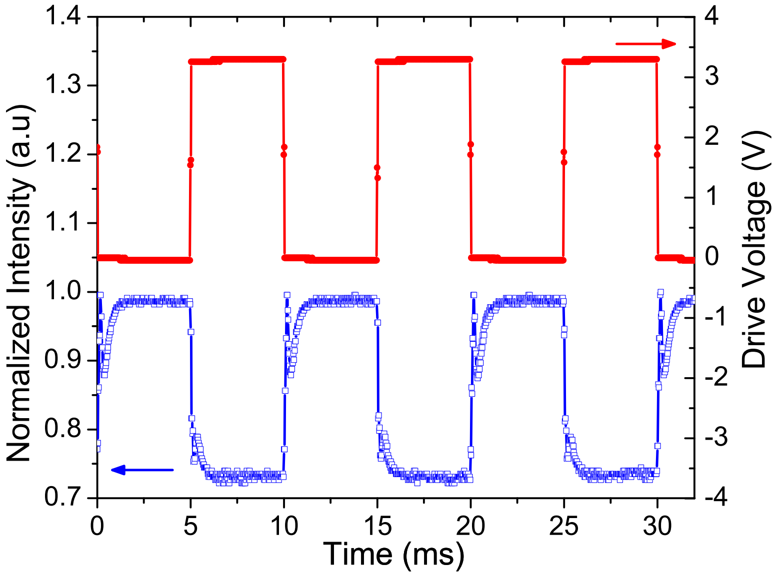

Figure 6.8: Temporal response of the layer transferred M-Z modulator to a square drive voltage.

Light with wavelength of 1550 nm was launched into the input facet of M-Z modulator. The light outcoupled from the output facet was monitored with a Ge detector. The device showed an insertion loss of 11 dB. This value is expected for SOI devices of 5x3 μm^2 facets. Then, we touched the contact pads with microprobes and applied electrical power. The pad and heater combination was measured to have a resistance of 400 Ω. The modulation observed with a square driving voltage with amplitude of 3.8 V and frequency of 100 Hz is given in Fig. 6.8. Although, the modulator does not show perfect switching (30 %), it has a significantly reduced P_π as compared to usual SOI M-Z modulators. We calculated a P_π value of 36 mW which is five times lower than an modulator fabricated by our group with the similar geometries [104].

We also tested the M-Z for its modulation speed. We increased the frequency of the driving voltage and measured the modulation depth of the optical signal. The measured data is plotted as a function of frequency in Fig. 6.9. The 3-dB cutoff frequency of 65 kHz was observed. This value is expectable for an SOI

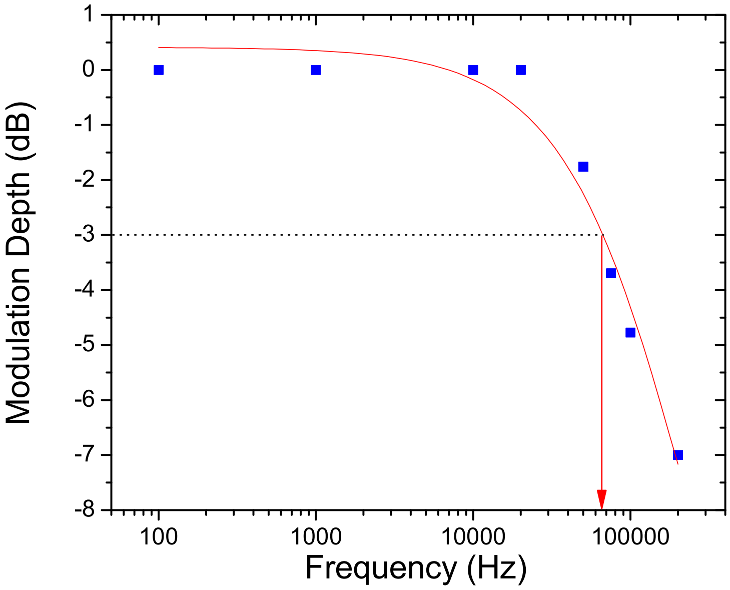

Figure 6.9: Measured modulation response to frequency change of driving voltage.

M-Z modulator of that geometry [104, 9]. The modulation speed of SOI M-Z modulator is not lowered by the layer transfer.

To summarize, we have applied a layer transfer method to an SOI M-Z modulator successfully. The resulting chip is an demonstration of an hybrid technology. The layer transferred SOI M-Z modulators was tested and observed to have similar temporal responses as ordinary SOI M-Z modulators with significantly reduced P_π. We should not that this is the first attempt demonstration of the feasibility of this approach. This method can be applied to M-Z modulators based on SOI nanowires for flexible integrated optics circuitry. Such an application would result in submiliwatt P_π values [37].

6.3 Silicon-polymer Asymmetric Vertical Coupler

6.3.1 Coupler Theory and Design

Whenever two optical waveguides are close enough, light may leak from one to the other through the coupling mechanism which is one of the mostly used physical effects in integrated optical devices, such as couplers, splitters, modulators and switches. The coupling between waveguides is generally analyzed by the coupled mode theory, predictions of which agrees extremely well with experimental results. In coupled mode theory, it is assumed that coupling changes the field amplitudes of modes, while their propagation constants remain unchanged.

Consider two slab waveguides in Fig. 6.10. The guiding regions have different refractive indices of n_1 and n_2 while all cladding regions are with index of n_c. This is an example for non-degenerate or asymmetric vertical coupler. We apply the coupled mode theory to this structure. We will not derive coupled mode equations and just make use of them. Derivations for these well known equations can be found in many introductory optoelectronics books [5, 6]. The coupled equations that relate the field amplitudes of the waveguide modes are

$$\frac{dA_1}{dz} = -j\kappa_{21} exp(j\Delta\beta z)A_2(z) \tag{6.5}$$

and

$$\frac{dA_2}{dz} = -j\kappa_{12} exp(j\Delta\beta z)A_1(z) \tag{6.6}$$

here, the difference between propagation constants is given as

$$\Delta\beta = \beta_1 - \beta_2 \tag{6.7}$$

and it is the measure of the phase mismatch. Also, κ_{21} and κ_{12} are coupling coefficients and are

$$\kappa_{21} = \frac{1}{2}(n_2^2 - n_c^2)\frac{k_0^2}{\beta_1}\int_{h_2+g}^{h_2+g+h_1} \varepsilon_1(y)\varepsilon_2(y)dy \tag{6.8}$$

and

$$\kappa_{12} = \frac{1}{2}(n_1^2 - n_c^2)\frac{k_0^2}{\beta_2}\int_{0}^{h_2} \varepsilon_2(y)\varepsilon_1(y)dy \tag{6.9}$$

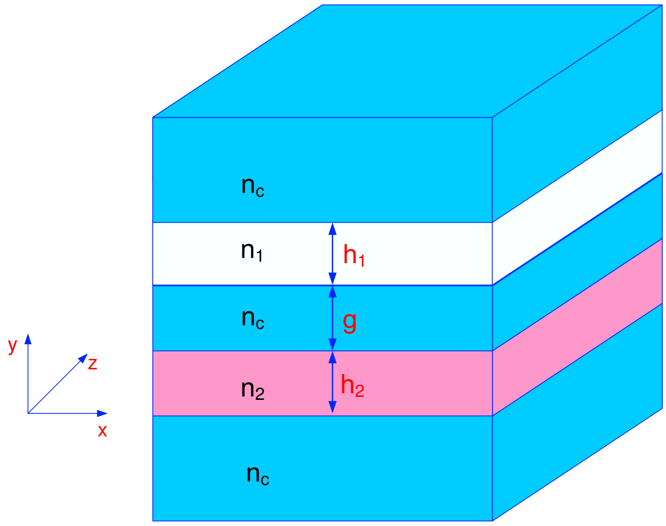

Figure 6.10: Two slab waveguides with different refractive index

for the mode fields ε_1 and ε_2. The energy conservation of the system requires that the coupling coefficients should be equal. Thus for the waveguide mode fields

$$\kappa_{12} = \kappa_{21} = \kappa \tag{6.10}$$

Applying the initial conditions, ie. $A_1(0) = 1$ and $A_2(0) = 0$, the equations can be solved to give two oscillating solutions for $A_1(z)$ and $A_2(z)$. Then, the optical powers are calculated by taking absolute square of the field amplitudes and found to be

$$P_1(z) = cos^2(\gamma z) + (\frac{\Delta\beta}{2\gamma})^2 sin^2(\gamma z) \tag{6.11}$$

and

$$P_2(z) = (\frac{\kappa^2}{\gamma^2}) sin^2(\gamma z) \tag{6.12}$$

where

$$\gamma^2 = (\frac{\Delta\beta}{2})^2 + \kappa^2 \tag{6.13}$$

is the *modified* coupling coefficient when there is a phase mismatch.

The optical power exchanges between waveguides with the period π/γ. The phase matching condition is achieved when the waveguides are identical, that is $\Delta\beta = 0$. The distance required for full power exchange under phase matching condition is

$$L_0 = \frac{\pi}{2\kappa} \tag{6.14}$$

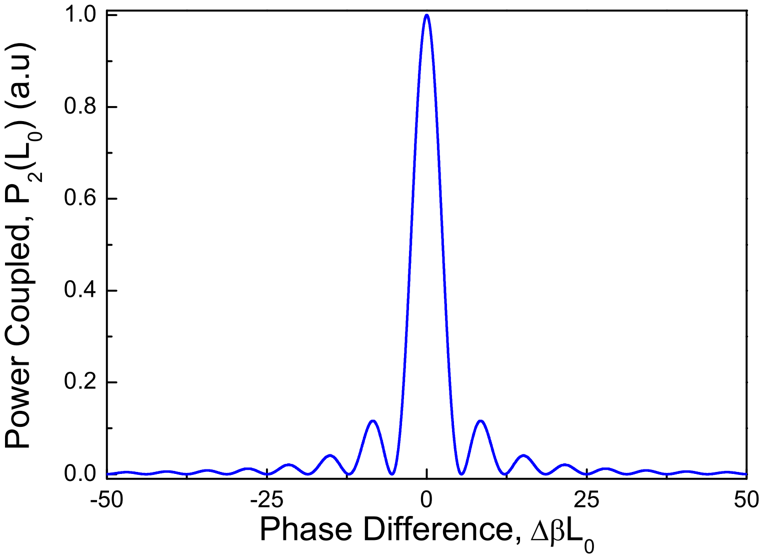

Figure 6.11: Power transferred as function of phase mismatch

However, the power transferred has very interesting behavior at the distance $L_0 = \frac{\pi}{2\kappa}$ when there is a phase mismatch between waveguide modes. It shows a diffraction like behavior and can be calculated using (6.12) and (6.13) to be

$$P_2(L_0) = (\frac{\pi}{2})^2 sinc^2\{\frac{1}{2}[1 + (\frac{\Delta\beta L_0}{\pi})^2]^{1/2}\} \tag{6.15}$$

where $sinc(x) = \sin(\pi x)/(\pi x)$ and the transmitted power is $P_1(L_0) = 1 - P_2(L_0)$. The transferred power can be understood better by drawing (6.15) as a function of $\Delta\beta L_0$ (Fig. 6.11). Phase mismatch, $\Delta\beta$ can also be written in terms of effective index difference and free space wavelength as

$$\Delta\beta = \frac{2\pi}{\lambda}\Delta n_{eff} \tag{6.16}$$

The coupled mode theory can be applied to a structure made of a low index waveguide on SOI substrate. It has been shown that such devices are highly wavelength selective [105]. In that case, n_1, n_2 and n_c becomes indices of silicon ($\sim$ 3.5), a low index material ($\sim$ 1.5), and SiO_2 ($\sim$ 1.46) respectively. If the low index waveguide is single mode but silicon slab has several modes, which can

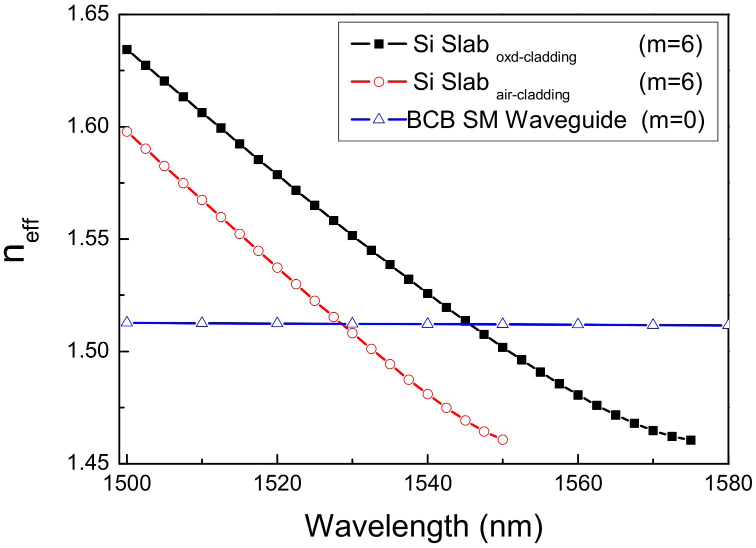

Figure 6.12: Effective TE refractive index change with free space wavelength for highest order mode ($m = 6$) of Si slab with SiO_2 and air as lower cladding and SM BCB waveguide

be achieved by choosing h_1 and h_2 appropriately, it can be clearly seen that the fundamental modes of silicon slab and the low index waveguide are never phase matched. Therefore, no significant power coupling happens between fundamental modes. However, the dispersion of the highest order mode of the silicon slab waveguide (see Fig. 6.12 for the transverse electric (TE) mode) can be used to phase match them with low index waveguide mode. A simple mode analysis shows that fundamental mode has negligible dispersion compared to higher order modes. Thus effective index, n_{sm} of single mode low index waveguide can be treated as constant. On the other hand, (Fig. 6.12) the highest order mode shows a nearly linear behavior between two cut-off wavelengths and this dispersion can be written as

$$n(\lambda) = n_{\lambda_{off1}} + m\lambda \qquad (6.17)$$

where $n_{\lambda_{off1}}$ is the effective index at smaller cut off wavelength and m is the associated slope in Fig. 3. Then, the effective index difference becomes $\Delta n_{eff} =$

$n(\lambda) - n_{sm}$ while phase mismatch is rewritten as

$$\Delta\beta = \frac{[n_{\lambda_{off1}} + m\lambda - n_{sm}]2\pi}{\lambda} \tag{6.18}$$

Therefore, transferred power (6.15) can be analyzed in the wavelength domain using (6.18).

What happens if a SM rib low index waveguide is placed instead of a slab waveguide to take advantage of butt coupling with a SM fiber? The solution is straight forward, mode analysis shows that mode dispersion of such a waveguide is also nearly constant. Thus the modified transferred power equations (Eq. 6.15 with Eq. 6.18) can be used but n_{sm} becomes effective index of the rib waveguide.

6.3.2 Fabrication and Results

We demonstrate an asymmetric vertical coupler by a hybrid integration of BCB waveguides with Si slabs on the same wafer. We propose two integration schemes. First is to define BCB waveguide on an SOI wafer through reactive ion etching of BCB polymer. The other one uses channels opened in a thick SiO_2 layer on a Si wafer as waveguide templates for BCB and Si layer transfer. Although the first scheme is simpler, the second one gives the opportunity of further processing of the Si layer and would be useful for novel device applications. The summary of the fabrication of asymmetric vertical coupler through the first scheme is shown in Fig.6.13. A SiO_2 layer of 2 μm was grown on a SOI wafer of 1.5 μm Si top layer. BCB was spin coated to form a 6 μm thick layer. Then, the wafer was put to the oven to cure the BCB. Straight PR strips of 6 μm width was patterned over BCB layer using photolithography (PL2) and etched down (RIE5) to form a BCB rib of 3 μm in height. A thick SiO_2 cladding deposition ended the fabrication of asymmetric couplers.

The fabricated wafer is cleaved to a chip of 10 mm in length and mounted in the experimental setup. The input light from the tunable laser is scanned from 1500 nm to 1580 nm an the light from output port of BCB waveguide is monitored with Ge photodetector. The measured spectrum is given in Fig. 6.14.

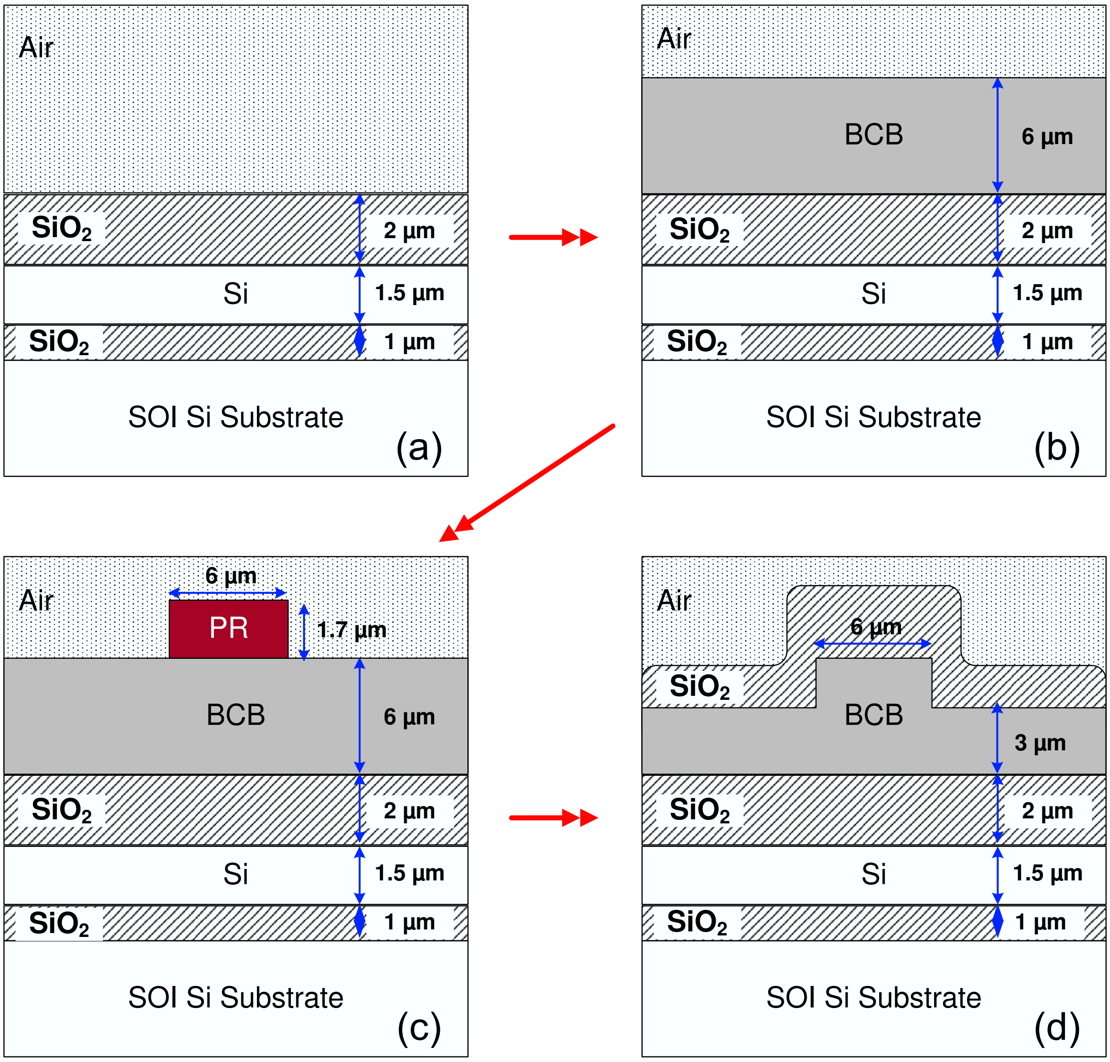

Figure 6.13: AVC fabrication steps first scheme (a) A SiO_2 layer is deposited on an SOI wafer of 1.5 μm top Si layer. (b) A BCB layer of 6 μm is spin coated on the wafer. (c) Waveguide strips are photolithographically defined to PR. (d) The unprotected BCB is etched down to define a rib. Finally a SiO_2 cap cladding layer covers the rib.

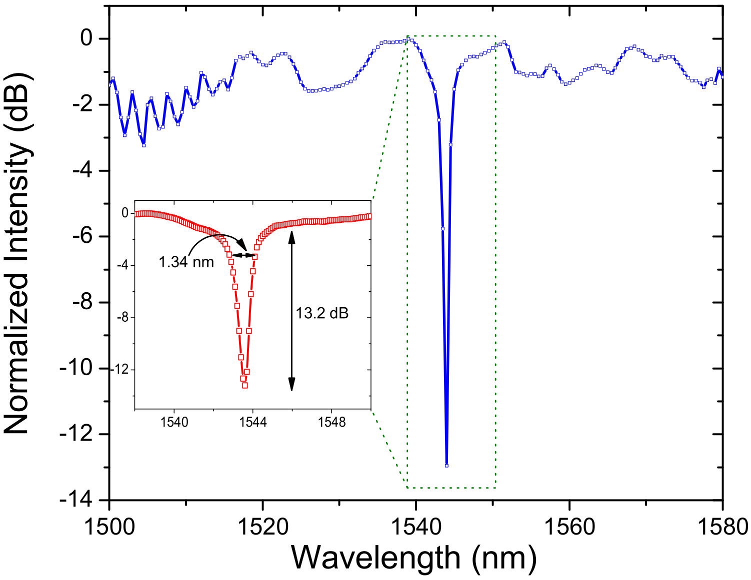

Figure 6.14: The measured spectrum of asymmetric vertical coupler fabricated through first scheme. The inset shows the drop in more detail.

The more detailed spectrum of the drop is given in the inset. An analysis of the figure produces a bandwidth of 1.34 nm and an modulation depth of 13.2 dB. The analytic calculations and BPM simulations estimated bandwidths in the order of 0.34 nm for a gap of 2 μm. The discrepancy can be explained as follows. These calculations assumed perfect thickness uniformity. However, the SOI wafer we used in fabrication has a Si layer with ± 20 nm thickness uniformity. Strong dependence of the response of the coupler on the Si layer thickness and its uniformity explains the increase in bandwidth.

Further BPM simulations showed that an decrease of 5 nm in thickness of Si layer resulted in a blue-shift of nearly 5 nm in drop wavelength of the spectrum. Therefore, the drop spectrum can be tuned by decreasing the silicon layer thickness. We made use of this fact to realize a multi channel wavelength drop filter. To realize such a device, we need to define and etch some parts of the Si layer. This further process is impossible with the first fabrication scheme. However, the second fabrication scheme which uses layer transfer method is appropriate

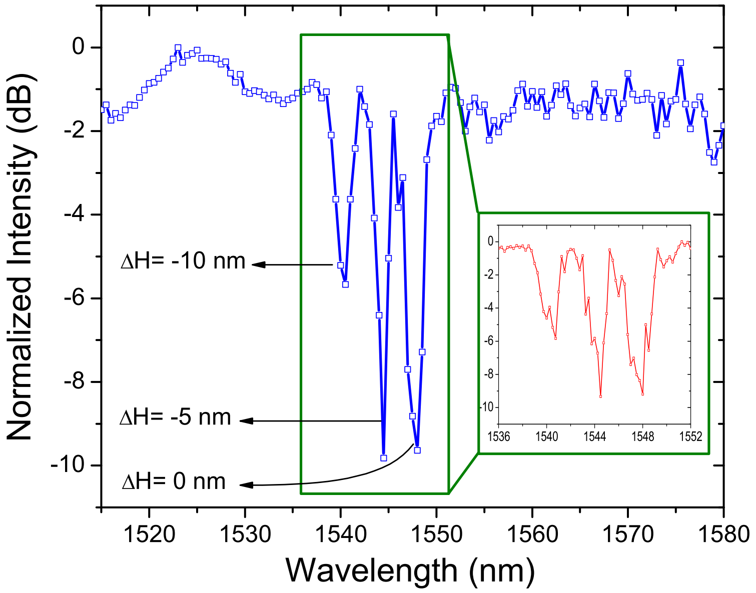

Figure 6.15: The measured spectrum of asymmetric vertical coupler fabricated through second scheme. The inset shows the drops in more detail.

for the process. Once the Si layer is transferred, backside of the layer is ready for pattern definition and etching. We start with preparation of templates for BCB waveguides on a thick SiO_2 overlaying a handle Si wafer. These are channel openings. Straight strips of 5 μm were defined with PR through image reversal photolithography. A thin Ni layer was sputtered on the wafer. A liftoff process leaded 5 μm openings on Ni layer. Then, Ni was used as the mask for the 3 μm etching of SiO_2 in a RIE process (RIE4). After Ni removal using piranha etch the templates are ready.

A BCB layer of 3 μm was spun on the handle wafer. This process filled the openings and resulted in a upside down rib waveguide. Meanwhile, a piece of an SOI wafer of 1.5 μm top Si layer was deposited with SiO_2 layer of 2 μm thickness. The SOI chip was bonded to the handle wafer after the BCB spin coating as explained in first section. The bonded wafers were put to an oven to cure BCB. The some parts of the stuck of wafers were covered with black wax and put in a KOH solution to remove substrate of SOI wafer. The more details of

BCB curing and substrate removing is explained in first section. The transferred Si layer was successively patterned to three parts and etched. A staircase like pattern was resulted with 5-10 nm steps. A PECVD grown SiO_2 layer finished the fabrication process. The spectrum obtained from an AVC fabricated with layer transfer method is shown in Fig. 6.15. Three independent drops are seen in the spectrum as expected. However, the exact positions of dips are different than the expected. The channels may not be fully filled with BCB. Remaining air bubbles in the channel may change the effective index of the waveguide and the position of dips.

In this section, we explained the physical principles behind operation of asymmetric vertical couplers and fabricated and measured Si-BCB couplers with two different fabrication schemes. These couplers may be used as wavelength filters, detectors and sensors [105, 106]

Chapter 7

Conclusions and Suggestions

Silicon photonics which is a novel research field and getting more attraction among researchers at both academic and industrial institutions is the main topic of this thesis work. We have designed, fabricated and characterized a number of both monolithic and hybrid integrated optical devices using silicon-on-insulator (SOI) wafers. The devices were designed using both analytical calculation and numerical simulations (beam propagation method, BPM).

So far researchers in the field of silicon integrated optics have been interested on either large cross-section SOI or nanowire waveguides. Formers are good for efficient coupling of light from a single mode fiber. Latter promise realization of very compact devices needed for a dense integration on a single chip. Hoverer, SOI rib waveguides having dimensions of the order of 1 μm have become a new branch of optical SOI waveguides [107]. These waveguides have sizes smaller than the conventional large cross-section SOI waveguides ($\geq$3 μm) but larger than those of SOI nanowires ($\leq$0.4 μm). Their geometrically controllable birefringence may be very helpful for polarization diversity in SOI integrated optical devices. We have used these waveguides to realize polarization splitters [68]. A polarization-independent racetrack resonator [93] has also been realized using SOI rib waveguides. Finally, we showed that dimensions not larger than 1 μm make fabrication of high-Q resonators with radii as small as 20 μm possible [94, 95].

An SOI rib waveguide becomes more birefringent as its size is reduced. We used this idea to design and fabricate a directional coupler polarization splitter based on geometrical birefringence. The device uses 1 μm sized silicon-on-insulator waveguides. The length of the device is about 2500 μm for gap of 1.4 μm but is drastically shortened to about 120 μm for gap of 0.7 μm. The polarization splitter is the first realized SOI integrated optical device that splits light to its TE and TM parts [68].

We have carried an in depth analysis of optical waveguide ring and racetrack resonators. Expected responses from one and two bus coupled resonators were driven. Issues that should be considered during the design of resonators were identified. We apply the analysis and design one and two bus coupled racetrack resonators on SOI rib waveguides. The geometry of the waveguide was similar to ones used in the design of polarization splitters. The bending losses and coupling factors are the most important points when designing waveguide resonators. The SOI rib waveguides used in the design were optimized for low bending losses. The racetrack shape was preferred for better control of the coupling factor.

We have proposed a novel integrated ring resonator displacement sensor for scanning probe microscopies. We designed and analyzed the feasibility of the integrated optical sensor. The concept based on elasto-optic effect is discussed. The design of the ring resonator was described and theoretical investigation of the force and displacement sensitivity was presented. The design of GaAs based cantilever with integrated ring and race-track resonator have been described in detail. We find that integrated optical sensor is attractive because of its high sensitivity and simplicity. We introduce a new application area for integrated optics. This design is a good alternative for piezoresistive cantilevers especially in electromagnetically active environments. Integrated sensors are suitable for cantilever arrays due to their compactness, simplicity and compatibility with mass production.

We have designed and fabricated SOI racetrack resonators and characterized them. Resonators with quality factors as high as 119000 were demonstrated for both polarizations. Furthermore, resonators have finesse values larger than 28 for TE polarization and larger than 43 for TM polarization. Using standard optical photolithography technology, the quality factor values reported here are the highest Q values achieved in the SOI platform, excluding submicron Si wire resonators. The response of resonators were analyzed by fitting the analytical functions. Resonator losses and coupling factors were extracted from the fitting process. Losses increases as resonator radius decrease in accordance with expectations. Extracted coupling factors were compared with those obtained from BPM simulations for various waveguide resonator gaps. Comparisons suggest that the fabrication procedure emmployed in this study leads narrower gaps than those in the mask. These high-Q resonators are suitable for applications such as quantum optics.

We investigated the resonators using SOI rib waveguides further and a waveguide structure with stronger light confinement was designed. We demonstrated that it is possible to realize SOI rib waveguide based racetrack resonators with radii as small as 20 and 40 μm for TM and TE polarized light, respectively. Free spectral ranges of 3.0 nm, finesse values of 18.3 and Q-factors of 33000 have been observed with the resonators based on new waveguide structure. This more compact SOI resonators can become key components for silicon based integrated optical devices and can even be easily integrated with MEMS structures (diaphragms and cantilevers etc.) for sensor applications. A good application for these resonators is the realization of displacement sensosr that we proposed in chapter 4. We have designed a mask and the fabrication of the sensor will be done by a member of our research group in the near future.

We have studied the thermooptical tunability of resonators that we fabricated. We also investigate possible use of such resonators as a wavelength selective switch. Our measurements show that resonators show thermo-optical tunability and operates as wavelength selective optical switches with low-power consumption of 17 mW. The devices were tested to function as switches at frequencies up to 210 kHz, the highest modulation frequency observed for SOI thermo-optical devices to the best of our knowledge.

Two bus coupled resonators were also fabricated and characterized. They were asymmetrically coupled to get better characteristics. These resonators functions as wavelength add/drop filters, a key element for WDM systems. Their Q-factors are limited by the coupling to the second bus waveguide. The resonators with bending radii ranging from 150 to 500 μm were fabricated and characterized. The resulting add/drop filters show Q-factors as high as 51000 and relatively low crosstalks of -10.0 dB. The crosstalk value can be reduced even further by a better match of critical coupling condition.

We have applied for the first time a layer transfer method to SOI wafers for integrated optical applications. The transfer method was previously used in GaAs/AlGaAs material system. To demonstrate the feasibility of the technique we fabricated straight waveguides, Mach-Zehnder modulators, asymmetric vertical couplers and hybrid silicon disk resonators. We optimized layer transfer method for SOI wafers. In particular, wafer preparation, bonding, protection during wet etching of silicon and the etching process were the steps that are handled for optimization.

We have fabricated and compared SOI waveguides on two chips. One was saved for comparison and the other was further processed for layer transfer. The comparison of modal and loss characteristics of the both waveguides clearly proves the feasibility of the silicon layer transfer process of SOI for integrated optical purposes. The use of a polymer as the bonding agent makes the bonding of a processed (i.e. having thickness variations) surface to another wafer possible by planarizing it. Finally, this process prepares the backsides of the waveguides for further processing. The quality of the backside surface is so high that many micro fabrication processes including photolithography, metallization and etching, can easily be performed. We believe that such a layer transfer process is a promising way of high-level hybrid integration of waveguide devices.

Furthermore, we have applied the layer transfer method to an SOI M-Z modulator. This process differs from the one for SOI waveguides on two points. These points makes the process even more challenging. First the area of transferred silicon layer is much larger and the the second the transfer layer have patterned thin metal parts on the surface. The resulting chip was an demonstration of an hybrid technology. The layer transferred SOI M-Z modulators was tested and observed to have similar temporal responses as ordinary SOI M-Z modulators and with significantly reduced P_π, electrical power required for a phase difference of $_\pi$. It is also believed that integration of a thick layer of material having large thermal conductivity (such as copper) may lead the device to operate at higher frequencies. This method can be applied to M-Z modulators based on SOI nanowires. Such an application would result in submiliwatt P_π values.

We also analyzed asymmetric vertical couplers and their potential applications. These couplers include a low index single mode waveguide in close proximity of a high index multimode waveguide. The coupling generally occurs between fundamental mode of the low index waveguide and the highest order mode of the high index one. The fundamental modes show no dispersion while the higher order modes does. The couplers are highly wavelength selective devices due to this difference between the dispersion of the waveguides and their response strongly depends on thickness of the layer with high refractive index. We fabricated and measured Si-BCB couplers with two different fabrication schemes. These couplers may be used as wavelength filters, detectors or sensors.

Finally, the research presented in this PhD thesis have resulted in five published or accepted journal papers, three submitted papers and seven published proceedings in technical conferences (see Appendix).

Bibliography

[1] G. Giesecke “Lattice Constants: Semiconductors and Semimetals 2”, New York:Academic (1976).

[2] H. Nishihara, M. Haruna and T. “Suhara Optical integrated circuits”, N.Y.:McGraw-Hill, (1989).

[3] R. Marz, “Integrated Optics”, Boston:Artech Hause, Inc., (1995).

[4] L. D. Hutcheson, “Integrated Optical Circuits and Components”, New York:Marcel Dekker, Inc., (1987).

[5] B. E. A. Saleh and M. C. Teich, “Fundamentals of Photonics”, N.Y.:John Wiley & Sons, (1991).

[6] Pollock C. R., “Fundamentals of Optoelctronics”, Chicago:Richard D. Irwin Inc., (1995).

[7] A. Ozcan, M. J. F. Digonnet, G. S. Kino, F. Ay and A. Aydinli, “Characterization of thermally poled germanosilicate thin films”, Optics Express, **12**:20, (2004).

[8] A. Liu, R. Jones, L. Liao, D. Samara-Rubio, D. Rubin, O. Cohen, R. Nicolaescu and M. Paniccia “A high-speed silicon optical modulator based on a metal-oxide-semiconductor capacitor”, Nature, **427**:p615, (2004).

[9] G. V. Treyz “Siliocn Mach-Zehnder Waveguide Interfereometers Operating at1.3μm”, Electronics Lettres, **27**:2, (1991).

[10] W. M. J. Green, R. K. Lee, G. A. DeRose, A. Scherer and A. Yariv, “Hybrid InGaAsP-InP Mach-Zehnder racetrack rasonator for thermooptic switching and coupling control,” Opt. Express, **13**:5, (2005).

[11] R. L. Espinola, M. C. Tsai, J. T. Yardley, and R. M. Osgood, Jr., “Fast and low-power thermooptic switch on thin silicon-on-insulator,” IEEE Photon. Technol. Lett., **15**:10 (2003).

[12] B. Jalali, S. Yegnanarayanan, T. Yoon, T. Yashimoto, I. Rendina, and F. Coppinger “Advances in Silicon-on-Insulator Optoelectronics”, IEEE Journal of Selected Topics in Quantum Electronics, **4**:6, (1998).

[13] R. A. Soref, F. Namavar and J. P. Lorenzo, “Optical Waveguiding in a Single-Crystal Layer of Germanium Silicon Grown on Silion”, Optics Letters, **15**:p270, (1990).

[14] T. Miya “Silica-Based Planar Lightwave Circuits: Passive and Thermally Active Devices”, IEEE Journal of Selected Topics in Quantum Electronics, **6**:1, (2000).

[15] R. Germann, H. W. M. Salamink, R. Beyeler, G. L. Bona, F. Horst, I. Massarek and B. J. Offrein “Silicon-Oxynitride Layers for Optical Waveguide Applications”, IBM Research Report, Engineering and Technology, **RZ 3102**:93147, (1999).

[16] F. Ay, A. Aydinli and S. Agan, “Low-loss as-grown germanosilicate layers for optical waveguides”, Applied Physics Letters, **83**:4743 (2003).

[17] A. Splett, J. Schmidtchen, B. Schuppert, K. Petermann,E. Kesper and H. Kibbel, “Low Loss Optical Ridge Waveguides in Strained GeSi Epitaxial Layer Grown on Silicon”, Electronics Letters, **26**:p1035, (1990).

[18] R. A. Soref, F. Namavar, “Optical Waveguiding in Ge_xSi_{1-x}/Si Heterostructures”, Journal of Applied Physics, **70**:p3370, (1990).

[19] S. F. Pesarcik, G. V. Treyz, S.S. Iyer, and J. M. Halbout, “Silicon Germanium Optical Waveguides With 0.5 dB/cm Losses for Single Mode Fiber Optic Systems”, Electronics Letters, **28**:p159, (1992).

[20] V. P. Kesan, P. G. May, E. bassous, and S. S. Iyer,"Integrated Waveguide/Photodetector using Si/SiGe Multiple quantum Wells For Long Wavekength Operation", in IEDM Tech. Dig.,p1035, (1990).

[21] R. A. Soref and J. P. Lorenzo, "All-silicon Active and Passive Guidedwave Components", IEEE Journal of Quantum Electronics, **22**:p873, (1986).

[22] A. Splett and K. Petermann , "Low Loss Single Mode Optical Waveguides with Large Cross-section in standard Epitaxial Silicon", IEEE Photonics Technology Letters, **6**:p425, (1994).

[23] B. Schuppert, J. Schmidtchen, A. Splett, U. Fisher, T. Zinke, R. Moosburger, K. Petermann, "Integrated Optics in Silicon and SiGe-Heterostructures", Journal of Lightwave Technology, **14**:10, (1996).

[24] S. K. Ghandhi, "VLSI Fabrication Principles, Silicon and gallium Arsenide", New York:John Wiley & Sons, (1994).

[25] M. Bruel, "Silicon on Insulator Material Technology ", Electronics Letters, **31**:14, (1995)

[26] SOITEC Silicon on Insulator Thechnologies, Bernin, France, http://www.soitec.com

[27] U. Fisher, J. R. Kropp, F. Arndt and K. Petermann, "0.1 dB/cm Waveguide Losses in Single-Mode SOI Rib Waveguides", IEEE Photonics Technology Letters, **8**:5, (1996).

[28] T. Zinke, U. Fisher, A. Splett, B. Schuppert, and K. Petermann, "Comparision of Optical Waveguide Losses in Silicon-on-Insulator", Electronics Letters, **29**:23, (1993).

[29] A. G. Rickman, G.T. Reed, "Silicon-on-Insulator Optical Rib Waveguides; Loss, Mode Characteristics, Bends and Y-junctions", IEEE Proc.-Optoelectronics, **141**:6, (1994).

[30] A. G. Rickman, F. Namavar, "Silicon-on-Insulator Optical Rib Waveguides Loss and Mode Characteristics", Journal of Lightwave Technology , **12**:10, (1994).

[31] R. M. Emmons, B. N. Kurdi, and D. G. Hall, “Buried-Oxide Silicon-on-Insulator Structures I: Optical Waveguide Characteristics”, IEEE Journal of Quantum Electronics, **28**:1, (1992).

[32] P. D. Trinh, S. Yegnanarayanan, B. Jalali, ”Integrated Optical Directional Couplers in Silicon-on-Insulator”, Electronics Lettres, **31**:24, (1995).

[33] P. D. Trinh, S. Yegnanarayanan, B. Jalali, “5x9 Integrated Optical Star Coupler in Silicon-on-Insulator Technology”, IEEE Photonics Technology Lettres, **8**:6, (1996).

[34] P. D. Trinh, S. Yegnanarayanan, B. Jalali, “Guided-Wave Optical Circuits in Silicon-on-Insulator Technology”, in Tech. Dig. Integrated photonics Research Conf., Boston **6**:p227, (1996).

[35] U. Fisher, T. Zinke, and K. Petermann, “Comparision of Optical Waveguide Losses in Silicon-on-Insulator”, Electronics Letters, **30**:5, (1994).

[36] B. E. Little, J. S. Foresi, G. Steinmeyer, E. R. Thoen, S. T. Chu, H. A. Haus, E. P. Ippen, L. C. Kimerling, and W. Green, “ Ultra-compact Si-SiO2 microring resonator optical channel dropping filters”, IEEE Photonics Tech. Lett. **10**:p549, (1998).

[37] M. W. Geis, S. J. Spector, R. C. Williamson, and T. M. Lyszczarz, “Submicrosecond submilliwatt silicon-on-insulator thermooptic switch”, IEEE Photon. Technol. Lett., **16**:11, (2004).

[38] W. Bogaerts, V. Wiaux, D. Taillaert, S. Beckx, B. Luyssaert, P. Bienstman and R. Baets, “Fabrication of Photonic Crystals in Siliconon- Insulator Using 248-nm Deep UV Lithography”, IEEE J. Sel. Top. Quant. Electron., **8**:4 (2002).

[39] Haisheng Rong, Richard Jones, Ansheng Liu, Oded Cohen, Dani Hak, Alexander Fang and Mario Paniccia, “A continuous-wave Raman silicon laser”, Nature, **433**:p725, (2005).

[40] A. Miliou, R. Srivastava and R. V. Ramaswamy, “A 1.3-μm directional coupler polarization splitter by ion exchange”, J. Lightwave Thecnol. **11**:2, (1993).

[41] K. Okamoto, M. Doi, T. Irita, Y. Nakano and K. Tada, “Fabrication of TE/TM mode splitter using completly buried GaAs/GaAlAs waveguide”, Jpn. J. Appl. Phys., **34**:1, (1990).

[42] P-K. Wei and W-S. Wang, “A TE-TM mode splitter on lithium niobate using Ti, Ni, and MgO diffusions”, IEEE Photon. Technol. Lett., **6**:2, (1994).

[43] C. Pu, Z. Zhu, and Y-H. Lo, “Surface micromachined integrated optic polarization beam splitter”, IEEE Photon. Technol. Lett., **15**:9, (2003).

[44] D. Taillaert, H. Chong, P. I. Borel, L. H. Frandsen, R. M. De La Rue and R. Beats, “A compact two-dimensional grating coupler used as a polarization splitter”, IEEE Photon. Technol. Lett., **15**:9, (2003).

[45] B. E. Little, J. S. Foresi, G. Steinmeyer, E. R. Thoen, S. T. Chu, H. A. Haus, E. P. Ippen. L. C. Kimerling, and W. Greene, “Verticaly coupled glass microring resonator channel droping filters,” IEEE Photon. Technol. Lett. **11**:p215, (1999)

[46] B. E. Little, H. A. Haus, J. S. Foresi, L. C. Kimerling, E. P. Ippen, and D. J. Ripin, “Wevelength switching and routing using absorption and resonance”, IEEE Photonics Tech. Lett. **10**:p816, (1998).

[47] A. F. J. Levi, R. E. Slusher, S. L. McCall, J. L. Glass, S. J. Pearton, and R. A. Logan, “Directional light coupling from microdisk lasers,” Appl. Phys. Lett. **62**:p561, (1993).

[48] D. J. W. Klunder, E. Krioukov, F. S. Tan, T. Van der Veen, H. F. Bulthuis, G. Sengo, C. Otto, H. J. W. M. Hoekstra, and A. Driessen, “Verticaly and laterally waveguide-coupled cylindirical microsesonators in Si_3N_4 on SiO_2 technology,”Appl. Phys. B **73**:p603, (2001).

[49] S. T. Chu, B. E. Little, W. Pan, T. Kaneko, S.Sato, and Y. Kokubun, “Second-order filter response from parallel coupled glass microring resonators,” IEEE Photon. Technol. Lett. **11**:p1426, (1999)

[50] J. Niehusmann, A. Vörckel, P. H. Bolivar, T. Wahlbrink, W. Henschel, and H. Kurz, “Ultrahigh-quality-factor silicon-on-insulator microring resonator,” Opt. Lett. **29**:p2861, (2004).

[51] K. K. Lee, D. R. Lim, L. C. Kimerling, j. Shin and F. Cerrina, “Fabrication of ultralow-loss Si/SiO_2 waveguides by roughness reduction”, Optics Lett., **43**:5, (2004).

[52] C. Colinge, B. Roberds, and B. Doyle, “Silicon layer transfer using wafer bonding and debonding”, J. Electron. Mater. **30**:p841, (2001).

[53] S. R. Sakamoto, C. Ozturk, Y. T. Byun, J. Ko, and N. Dagli, “Low-loss substrate removed (SURE) optical waveguides in GaAs-AlGaAs epitaxial layers embedded in organic polymers”, IEEE Photon. Tech. Lett. **10**:p985, (1998).

[54] I. Kiyat,“Silicon-on-insulator optical waveguides and waveguide devices,” Ms. Thesis, Bilkent University, (2000).

[55] A. Kocabas, F. Ay, A. Dana, I. Kiyat and A. Aydinli“High refractive index measurement using elestomeric grating coupler”, Accepted for publication in Opt. Lett., (2005).

[56] R. A. Soref, J. Schmidchen, K. Petermann, “Large Single Mode Rib Waveguides in GeSi-Si and Si-onSiO_2”, IEEE Journal of Quantum Electronics, **27**:8, (1991).

[57] S. P. Pogossian, L. Vescan, and A. Vonsovici”The Single Mode Condition for Semiconductor Rib Waveguides with Large Cross Section”, Journal of Lightwave Technology, **16**:10, (1998).

[58] RSoft Designing Group, Ossining, NY, USA; http://www.rsoftdesign.com

[59] R. Wolf and R. N. Tauber, “Silicon Processing, Volume1-Process Technology”, Sunset Beach, CA:Lattice Press, (1986).

[60] Clariant AG, http://www.clariant.com

[61] R. Williams, “Modern GaAs Processing Techniques”, Nowood, MA:Artech Hauses Inc., (1990).

[62] C. Z. Zhao, G. Z. Li, E. K. Liu, Y. Gao and X. D. Liu, “Silicon on Insulator Mach-Zehnder Waveguide Interferometers Operating at 1.3 μm”, Applied Physics Letters, **67**:17, (1995).

[63] K. E. Bean, “Anisotropic Etching of Silicon”, IEEE Transactions on Electron Devices, **ED-25**:10, (1978).

[64] W-T Tsang, C-C Tseng, and S. Wang, “Optical Waveguides Fabricated by Preferential Etching”, Applied Optics, **14**:5, (1975).

[65] R. G. Hunsperger, “Integrated Optics”, Berlin: Springer-Verlag, (1995).

[66] P. D. Trinh, S. Yagnanarayanan and B. Jalali, “Integrated optical directional couplers in silicon-on-insulator”, Electron. Lett., **31**:24, (1995).

[67] D. Dai and S. He, “Analysis of the birefringence of a silicon-on-insulator rib waveguide”, Applied Optics, **43**:5, (2004).

[68] I. Kiyat, A. Aydinli and N. Dagli, “A Compact Silicon-on-Insulator Polarization Splitter,” IEEE Photon. Technol. Lett. **17**:p100, (2005).

[69] J. L. Altman, “Microwave Circuits”, Princeton, N. J: Van Nostrand, (1964).

[70] D. G. Rabus, “Realization of optical filters using ring resonators with integrated semiconductor optical amplifiers in GaInAsP/InP,” PhD. Thesis, Technical University of Berlin, (2002).

[71] R. Grover, “Indium phosphide based optical micro-ring resonators,” PhD. Thesis, University of Maryland, (2003).

[72] V. Subramaniam, G. N. De Brabander, D. H. Naghski and J. T. Boyd, “Measured of mode field profiles and bending and transition losses in curved optical channel waveguides,” J. Lightwave Technol. **15**:p990, (1997).

[73] L-edit, the Layout editor, Tanner Research INC.

[74] C. Kocabas, “Integrated optical displacement sensors for scanning force microscopies,” Ms. Thesis, Bilkent University, (2003).

[75] I. Kiyat, C.Kocabas and A.Aydinli, “Integrated micro-ring resonator displacement sensor for scanning probe microscopies”, Journal of Micromechanics and Microengineering, **14**:14, (2004).

[76] G. Binning, C. Quate and C. Gerber, “Atomic force microscope”, Phys. Rev. Lett. **56**:p930, (1986).

[77] G. Meyer and N. M. Amer, “Novel optical approach to atomic force microscopy” , Appl. Phys. Lett. **53**:p1045, (1988).

[78] D. Rugar, H. J. Mamin and P. Guethner, “Improved fiber-optic interferometer for atomic force microscopy”, Appl. Phys. Lett. **55**:p2588, (1989).

[79] M. Tortonese, H. Yamada, R. C. Barrett and C. F. Quate, “Atomic force microscopy using a piezoresistive cantilever” Proceeding of IEEE conferance on Tranducers, p448, (1991).

[80] S. Akamine, T. R. Albrecht, M. J. Zdeblick and C. F. Quate, “Microfabricated scanning tunneling microscope”, IEEE Electron Device Letters, **10**:p490, (1989).

[81] S. R. Manalis, S. C. Minne, A. Atalar and C. F. Quate, “Interdigital cantilever for atomic force microscopy”, Appl. Phys. Lett., **69**:3944,(1996).

[82] C. Wagner, J. Frankenberger and P. P. Daimel, “Optical pressure sensor based on Mach-Zehnder interferometer integrated with a lateral a-Si:H p-i-n photodiode”, IEEE Electronic Device Letters **10**:p1257, (1993).

[83] B. J. Luff, R. D. Harris, J. S. Wilkinson, R. Wilson, and D. J. Schiffirin ,“Integrated-optical directional coupler biosensor”, Opt. Lett. **21**:p618, (1996).

[84] G. N. De Brabander, J. T. Boyd and G Beheim, “Integrated optical ring resonator with micromechanical diaphragm for pressure sensing”, IEEE Photonics Tech. Lett. **6**:p671, (1994).

[85] PCT application with aplication No. PCT/TR03/053 (filled 18 June 2003) Integrated Optical Sensors for Scaning Probe Microscopies

[86] K. Okamoto, “Fundamentals of Optical Waveguide”, New York: Academic Press, (2000).

[87] M. K. Chin, C. Youtsey, W. Zhao, T. Pierson, Z. Ren, S. L. Wu, L. Wang, Y. G. Zhao, and S. T. Ho, “GaAs microcavity channel-dropping filter based on a race-track resonator”, IEEE Photon. Technol. Lett., **11**:12, (1999).

[88] ANSYS inc., http://www.ansys.com/

[89] A. J. Brook, S. J. Bending, J. Pinto, A. Oral, D. Ritchie, H. Beere, A. Springthorpe and M.Henini, “Micromachined III-V cantilevers for AFM-tracking scanning hall probe microscopy”, Journal of Micromechanics and Microengineering, **13**:p124, (2003).

[90] A. J. Brook, S. J. Bending, J. Pinto, A. Oral, D. Ritchie, H. Beere, M. Henini and A. Springthorpe, “Integrated piezoresistive sensors for atomic force-guided scanning Hall probe microscopy”, Applied Physics Letter, **82**:p3538, (2003).

[91] R. G. Beck, M. A. Eriksson, M. A. Topinka, R. M. Westervelt, K. D. Maranowski and A. C. Gossard, “GaAs/AlGaAs self-sensing cantilevers for low temperature scanning probe microscopy”, Applied Physics Letter, **73**:p1149, (1998).

[92] M. Tortonese, “Cantilevers and tips for atomic force microscopy”, IEEE Engineering in Medicine and Biology, **March/April**:p28, (1997).

[93] W. R. Headley, G. T.Reed, S. Howe, A. Liu, and M. Paniccia, “Polarization-independent optical racetrack resonators using rib waveguides on silicon-on-insulator”, Appl. Phys. Lett., **85**:p5523, (2004).

[94] I. Kiyat, A. Aydinli and N. Dagli, “High-Q silicon-on-insulator optical rib waveguide racetrack resonators”, Opt. Express, **13**:p1900, (2005).

[95] I. Kiyat, A. Aydinli and N. Dagli, “Polarization Characteristics of Compact SOI Rib Waveguide Racetrack Resonators”, Accepted for publication in IEEE Photonics Tech. Lett.(To apear in October 2005 issue).

[96] T. Sadagopan, S. June Choi, S. Jun Choi, K. Djordjev, and P. D. Dapkus, “Carrier-induced refractive index changes in InP-based circular microresonators for low-voltage high-speed modulation”, IEEE Photon. Technol. Lett., **17**:2, (2005).

[97] V. R. Almeida, C. A. Barrios, R. R. Panepucci, M. Lipson, M. A. Foster, D. G. Ouzounov and A. L. Geata “All-optical switching on a silicon chip” Opt. Lett., **29**:24, (2004).

[98] M. Harjanne, M. Kapulainen, T. Aalto, and P. Heimala, “Sub-μs switching time in silicon-on-insulator Mach-Zehnder thermooptic switch”, IEEE Photon. Technol. Lett., **16**:9, (2004).

[99] I. Kiyat, A. Aydinli and N. Dagli, “Low-Power Thermooptical Tuning of SOI Resonator Switch”, Submitted to IEEE Photonics Tech. Lett., (2005).

[100] A. Vorckel, M. Monster, W. Henschel, P. H. Bolivar, and H. Kurz, IEEE Photon. Technol. Lett., **15**:p921, (2003).

[101] I. Kiyat, A. Aydinli and N. Dagli, “Add/drop filters based on asymmetrically coupled high-Q SOI racetrack resonators”, Submitted to Applied Phys. Lett., (2005).

[102] C. Ozturk “Tunable hybrid polymer-compound semiconductor devices for WDM applications”, PhD Thesis, University of California, Santa Barbara, (2002).

[103] T. E. Murphy, “Design, Fabrication and Measurement of Integrated Bragg Grating Optical Filters”, PhD Thesis, Massachusetts Institute of Technology, (2001).

[104] A. Kocabas, “Polarization independent thermo-optic modulators for integrated optics,” Ms. Thesis, Bilkent University, (2003).

[105] B. Pezeshki, F. Agahi, J. A. Kash, J.J Welser and W-K. Wang, “Wavelength selective waveguide photodetectors in silicon-on-insulator”, Appl. Phys. Lett., **68**:p741, (1996).

[106] I. Kiyat, A. Kocabas, I. Akca and A. Aydinli, “Integrated asymmetric vertical coupler pressure sensor”, Photonics Europe, 26-30 April, 2004, Strasburg, France, Conference 5455, n. 04, (2004).

[107] WS. P. Chan, C. E. Png, S. T. Lim, G. T.Reed, and V. M. N. Passaro, “Single-Mode and polarization-independent silicon-on-insulator waveguides with small cross section”, J. Lightw. Technol., **23**:6, (2005).

Appendix A

List of Publications

Published or Accepted for Publication in Peer-reviewed Journals:

1) A. Kocabas, Feridun Ay, Aykutlu Dana, I. Kiyat, A. Aydinli, "High refractive index measurement using elestomeric grating coupler", Accepted for publication in Optic Letters (2005).

2) I. Kiyat, A. Aydinli and Nadir Dagli, "Polarization Characteristics of Compact SOI Rib Waveguide Racetrack Resonators", Accepted for publication in IEEE Photonics Technology Letters, (2005).

3) I. Kiyat, A. Aydinli and Nadir Dagli, "High-Q silicon-on-insulator optical rib waveguide racetrack resonators", Optics Express, v.13, n.6, pp.1900-1905 (2005).

4) I. Kiyat, A. Aydinli and Nadir Dagli, "A Compact Silicon-on Insulator Polarization Splitter", IEEE Photonics Technology Letters, v.17 n.1, pp.100-102 (2005).

5) I. Kiyat, C. Kocabas and A. Aydinli, "Integrated Micro-Ring Resonator Displacement Sensor for Scanning Probe Microscopies", J. Micromech. Microeng. v.14, n.3, pp.374-381, (2004).

Submitted to Peerreviewed Journals:

1) I. Kiyat, A. Aydinli and Nadir Dagli, “Low-Power Thermooptical Tuning of SOI Resonator Switch”, Submitted to IEEE Photonics Technology Letters., (2005).

2) P. Zorlutuna, A. Tezcaner, I. Kiyat, A. Aydinli and V. Hasirci, “Cornea Engineering on Polyester Carriers”, Submitted to Journal of Biomedical Materials Research: Part A, (2005).

3) I. Kiyat, A. Aydinli and Nadir Dagli, “Add/drop filters based on asymmetrically coupled high-Q SOI racetrack resonators,” Submitted to Applied Physics Letters., (2005).

Proceedings of Technical Conferences:

1) I. Kiyat, A. Aydinli and Nadir Dagli, “Geometrical Birefringence Based Polarization Splitter”, 30th European Conference on Optical Communications (ECOC 2004), 5-9 September, 2004, Stockholm, Sweden, Proceedings v.3, We4.P.049, (2004)

2) H. Kenar, I. Kiyat, A. Tezcaner, A. Aydinli and V. Hasirci, “Design of Micropatterned Polymeric Surfaces for Neo-Organ Preparation Using Nanotechnological Approaches”, 11th International Biomedical Science and Technology Days, 6-10 September, 2004, Ankara, Turkey.

3) I. Kiyat, A. Kocabas, I. Akca and A. Aydinli, “Integrated Asymmetric Vertical Coupler Pressure Sensor”, Photonics Europe, 26-30 April, 2004, Strasburg, France, Conference 5455, n. 04, (2004).

4) I. Kiyat, C. Kocabas and A. Aydinli, “Pressure Sensing Using Micromachined Asymmetric Integrated Vertical Coupler”, IEEE Lasers and Electro-Optics Society (LEOS) 2003 Annual Meeting, Tucson, AZ, WE1, Vol. 2, p.515, (2003).

5) A. Aydinli, I. Kiyat and C. Kocabas, “Novel Integrated Optical Displacement Sensor For Scanning Force Microscopies”, IEEE Lasers and Electro-Optics

Society (LEOS) 2003 Annual Meeting, Tucson, AZ, WE2, Vol. 2, p.517, (2003).

6) I. Kiyat, C. Kocabas and A. Aydinli, “Pressure Sensing Using Micromachined Asymmetric Integrated Vertical Coupler”, 12th European workshop on Heterostructure Technology , 12-15 October, 2003, Segovia, Spain, Book of Abstracts, MonB4, (2003).

7) I. Kiyat, C. Kocabas and A. Aydinli, “Integrated Optical Asymmetric Coupler Pressure Sensor”, AIP Conference Proceedings Vol. 709(1) pp. 431-432. May 10, 2004, The conference: International School of Quantum Electronics, 39th Course, Microresonator as Building Blocks for VLSI Photonics, 18-26 October, 2003, Erice, Sicily, Italy, (2003).